

# Modeling the rational synthesis of magnesium difluoride via the low-temperature atom beam deposition method



Sridhar Neelamraju

Max-Planck-Institut für Festkörperforschung

Dissertation an der Universität Stuttgart  
Stuttgart  
February 2013

---

# Modeling the rational synthesis of magnesium difluoride via the low-temperature atom beam deposition method

Von der Fakultät Chemie der Universität Stuttgart  
zur Erlangung der Würde eines  
Doktors der Naturwissenschaften (Dr. rer. nat.)  
genehmigte Abhandlung

Vorgelegt von  
**Sridhar Neelamraju**  
aus Neu Delhi, Indien

Hauptberichter:	Prof. Dr. Martin Jansen
Mitberichter:	Prof. Dr. Thomas Schleid
Vorsitzender:	Prof. Dr. Eric Mittemeijer
weiterer Prüfer:	PD Dr. K. Doll

Tag der mündlichen Prüfung: 18.02.2013

Max-Planck-Institut für Festkörperforschung, Stuttgart, 2013

## Acknowledgements

This thesis would not have been possible without the help and guidance of many people. I would like to thank:

- **Prof. Dr. Dr. h.c. Martin Jansen**, for giving me the opportunity to work in his research group and providing me with the necessary financial support and his keen interest in my research.
- **Prof. Dr. Christian Schön, FRSC** for his mentoring and guidance at every step of my research.
- **Priv.-Doz. Dr. Klaus Doll**, for very interesting scientific discussions and guidance.
- Other members of my thesis committee **Prof. Dr. Thomas Schleid** and **Prof. Dr. Ir. Eric J. Mittemeijer**.
- All members of the Jansen group at Max Planck Institute for Solid State Research, Stuttgart for making my time here very memorable. Special thanks to the theory sub-group including Ulrich Wedig, Nicola Toto, Aniket Kulkarni, Dejan Zagorac, Ramli Ismail and Manish Sultania for their help and support.
- The groups I have collaborated with over the past year including Dr. Dieter Fischer and Dr. Andreas Bach at Max Planck Institute for Solid State Research, Stuttgart and Xiaoke Mu, Dr. Wilfried Sigle and Prof. P. A. Van Aken at the Stuttgart center for electron microscopy, Max Planck Institute for Intelligent Systems, Stuttgart for lots of stimulating and fruitful discussions.
- Finally, I would like to thank my family and especially my father **Dr. N. H. Rao**, mother **Dr.(Mrs.) N. Sarla** and sister N. Bharati for their unwavering support and belief in my abilities.

# Contents

List of Figures	vii
<b>I Introduction</b>	<b>1</b>
<b>1 Introduction</b>	<b>3</b>
1.1 Introduction . . . . .	3
<b>II Background</b>	<b>7</b>
<b>2 Background</b>	<b>9</b>
2.1 Brief literature review . . . . .	9
2.1.1 Experiments on MgF <sub>2</sub> . . . . .	9
2.1.2 Theoretical studies on MgF <sub>2</sub> . . . . .	10
2.1.3 Deposition of atoms and clusters on a substrate . . . . .	10
2.2 Constructing an energy landscape . . . . .	11
2.2.1 Global optimization . . . . .	12
2.2.1.1 Simulated annealing . . . . .	12
2.2.1.2 Genetic algorithms . . . . .	12
2.2.1.3 Basin hopping . . . . .	13
2.2.2 Exploring the barrier structure . . . . .	13
2.2.2.1 Threshold algorithm . . . . .	13
2.2.3 Free energy . . . . .	15
2.3 Molecular Dynamics simulations . . . . .	15
2.3.1 Force calculations . . . . .	15
2.3.2 Velocity-Verlet algorithm . . . . .	15
2.4 Electronic structure calculations . . . . .	16
2.4.1 Hartree-Fock method . . . . .	16
2.4.2 Density Functional Theory . . . . .	17
2.4.3 Basis sets . . . . .	19
2.5 Low-temperature atom beam deposition of MgF <sub>2</sub> . . . . .	20

## CONTENTS

---

<b>III</b>	<b>Methods</b>	<b>23</b>
<b>3</b>	<b>Methods</b>	<b>25</b>
3.1	Introduction . . . . .	25
3.2	Exploration of energy landscapes . . . . .	25
3.2.1	Global optimization parameters . . . . .	25
3.3	Energy calculations . . . . .	26
3.3.1	Potentials . . . . .	26
3.3.2	Ab initio energy calculations . . . . .	27
3.4	Calculation of Raman and IR spectra . . . . .	29
3.4.1	Clusters . . . . .	29
3.4.2	Periodic systems . . . . .	29
3.5	Molecular Dynamics simulations . . . . .	30
<b>IV</b>	<b>Energy landscape investigations on MgF<sub>2</sub></b>	<b>33</b>
<b>4</b>	<b>Exploration of the energy landscape on MgF<sub>2</sub></b>	<b>35</b>
4.1	Bulk MgF <sub>2</sub> . . . . .	35
4.2	Detailed energy landscapes of neutral (MgF <sub>2</sub> ) <sub>n</sub> (n=3, 4) clusters . . . . .	36
4.2.1	Local minima and energies . . . . .	36
4.2.2	Energetic barriers - (MgF <sub>2</sub> ) <sub>3</sub> . . . . .	40
4.2.3	Energetic barriers - (MgF <sub>2</sub> ) <sub>4</sub> . . . . .	41
4.2.4	Probability flows - (MgF <sub>2</sub> ) <sub>3</sub> . . . . .	41
4.2.5	Probability flows - (MgF <sub>2</sub> ) <sub>4</sub> . . . . .	44
4.2.6	Holding point analysis - (MgF <sub>2</sub> ) <sub>3</sub> . . . . .	44
4.2.7	Holding point analysis - (MgF <sub>2</sub> ) <sub>4</sub> . . . . .	48
4.2.8	Local density of states - (MgF <sub>2</sub> ) <sub>3</sub> . . . . .	50
4.2.9	Comparison of ab initio and empirical landscapes . . . . .	50
4.2.10	Thermodynamics . . . . .	51
4.3	Global optimizations of neutral (MgF <sub>2</sub> ) <sub>n</sub> clusters . . . . .	54
4.4	Global optimizations of charged clusters . . . . .	54
4.4.1	Conclusion . . . . .	56
<b>V</b>	<b>Ab initio Raman and IR spectroscopy</b>	<b>59</b>
<b>5</b>	<b>Ab initio Raman and IR spectroscopy</b>	<b>61</b>
5.1	Methodology . . . . .	61
5.1.1	Theory . . . . .	61
5.1.1.1	Local optimization and determination of IR/Raman frequencies . . . . .	61
5.1.2	Experiment . . . . .	63
5.2	Raman and IR calculations for neutral (MgF <sub>2</sub> ) <sub>1-10</sub> clusters . . . . .	65
5.3	Charged Clusters . . . . .	65
5.4	Assignment of predicted vapor phase structures to experimental observations . . . . .	65

5.5	Specific structural features . . . . .	68
5.5.1	Fingerprint frequencies . . . . .	68
5.5.2	Order parameter for amorphous-crystalline transition . . . . .	70
5.6	Limitations . . . . .	70
5.6.1	Computational limitations . . . . .	70
5.6.2	Experimental limitations . . . . .	71
5.7	Conclusion . . . . .	71
<b>VI Molecular Dynamics simulations</b>		<b>73</b>
<b>6 Atomistic modeling of the LT-ABD method</b>		<b>75</b>
6.1	Introduction . . . . .	75
6.2	Setting up the substrates for deposition . . . . .	75
6.2.1	$\alpha$ -Al <sub>2</sub> O <sub>3</sub> substrate . . . . .	75
6.2.2	MgF <sub>2</sub> -anatase substrate . . . . .	76
6.2.3	MgF <sub>2</sub> -rutile substrate . . . . .	78
6.3	Setting up the vapor phase . . . . .	78
6.4	Deposition . . . . .	79
6.4.1	Deposition on $\alpha$ - Al <sub>2</sub> O <sub>3</sub> . . . . .	79
6.4.2	Analysis of the deposition . . . . .	79
6.5	Tempering . . . . .	81
6.5.1	Structural features of the deposit . . . . .	83
6.5.2	Mechanism . . . . .	85
6.5.3	Diffusion profiles . . . . .	87
6.6	Epitaxial growth and tempering on MgF <sub>2</sub> -anatase . . . . .	89
6.7	Radial distribution functions . . . . .	90
6.8	Conclusion . . . . .	94
<b>References</b>		<b>97</b>
<b>VII Appendix</b>		<b>107</b>
<b>A Vibrational frequencies of neutral clusters</b>		<b>109</b>
<b>B Vibrational frequencies of global minima upto 10 units</b>		<b>115</b>
<b>C Vibrational frequencies of ionic clusters</b>		<b>125</b>
<b>D Vibrational modes for all the periodic structures studied</b>		<b>133</b>
<b>E Raman intensities for global minima of (MgF<sub>2</sub>)<sub>n</sub> clusters</b>		<b>137</b>
<b>F Raman active modes observed in rutile structures</b>		<b>141</b>

## CONTENTS

---

G	CaF <sub>2</sub> -Energy-Volume curves	143
H	List of publications	145
VIII	Formalia	147



# List of Figures

1.1	Low-temperature atom beam deposition setup . . . . .	5
2.1	Threshold algorithm . . . . .	14
2.2	Hartree-Fock algorithm . . . . .	18
2.3	Parameter field for synthesis . . . . .	21
3.1	Effect of reducing basis sets on landscape . . . . .	29
3.2	MD code schematic . . . . .	31
4.1	E(V) curves for MgF <sub>2</sub> polymorphs . . . . .	36
4.2	Relative energies on empirical potential and ab initio level (HF, DFT-LDA, DFT-B3LYP) for cluster configurations with respect to the global minimum for the trimer (a) and tetramer (b), respectively. For the ab initio calculations, the Large basis set was used. . . . .	39
4.3	Isomers of (MgF <sub>2</sub> ) <sub>3</sub> . . . . .	40
4.4	Energetic barriers . . . . .	41
4.5	Tree-graph representations of ab initio and empirical energy landscapes . . . . .	42
4.6	Tree-graph representation of (MgF <sub>2</sub> ) <sub>4</sub> . . . . .	43
4.7	Probability flow chart: Trimer . . . . .	45
4.8	Probability flow chart: Tetramer . . . . .	46
4.9	Holding point analysis: trimer . . . . .	47
4.10	Holding point analysis: tetramer . . . . .	49
4.11	LDOS for neutral clusters studied . . . . .	51
4.12	Boltzmann distribution curves . . . . .	53
4.13	Global minima for neutral clusters up to 10 units of MgF <sub>2</sub> . . . . .	54
4.14	Isomers of ionic clusters . . . . .	56
5.1	Raman frequencies and intensities for neutral clusters . . . . .	62
5.2	Experimental Raman spectrum of vapor phase of MgF <sub>2</sub> . . . . .	63
5.3	Experimental Raman spectrum for bulk MgF <sub>2</sub> . . . . .	64
5.4	Raman frequencies and intensities for charged clusters of MgF <sub>2</sub> . . . . .	66
5.5	Raman active frequencies for (meta)stable modifications of bulk MgF <sub>2</sub> . . . . .	67
5.6	IR active frequencies and intensities for neutral clusters of MgF <sub>2</sub> . . . . .	68
5.7	IR active frequencies for possible (meta)stable modifications of bulk MgF <sub>2</sub> (Intensities for each structure are shown in the appendix). . . . .	69
5.8	Fingerprint frequencies for linear isomers . . . . .	69

## LIST OF FIGURES

---

5.9	Examples of the Raman active frequencies possibly characteristic of the amorphous $\text{MgF}_2$ deposit containing dangling bonds. . . . .	70
6.1	Substrates for deposition . . . . .	77
6.2	Snapshots during growth of amorphous deposit . . . . .	80
6.3	Analysis of growth of amorphous deposit . . . . .	82
6.4	Snapshots during annealing at 1500K . . . . .	83
6.5	Analysis of annealing at 1500K . . . . .	84
6.6	ABAB stacking of fluorine atoms . . . . .	85
6.7	Competing $\text{CdI}_2$ -type and $\text{CaCl}_2$ -type nuclei . . . . .	86
6.8	Distribution of competing nuclei . . . . .	86
6.9	Fluorine diffusion profiles . . . . .	87
6.10	Magnesium diffusion profiles . . . . .	88
6.11	Deposition on $\text{MgF}_2$ seeds . . . . .	89
6.12	Annealing on $\text{MgF}_2$ anatase . . . . .	90
6.13	Annealing on $\text{MgF}_2$ anatase . . . . .	91
6.14	Comparison of RDFs . . . . .	92
6.15	Comparison of RDFs . . . . .	93
E.1	Raman frequencies and intensities for global minimum of $(\text{MgF}_2)_4$ at the B3LYP/6311++G** level . . . . .	137
E.2	Raman frequencies and intensities for global minimum of $(\text{MgF}_2)_5$ at the B3LYP/6311++G** level . . . . .	138
E.3	Raman frequencies and intensities for global minimum of $(\text{MgF}_2)_6$ at the B3LYP/6311++G** level . . . . .	138
E.4	Raman frequencies and intensities for global minimum of $(\text{MgF}_2)_7$ at the B3LYP/6311++G** level . . . . .	139
E.5	Raman frequencies and intensities for global minimum of $(\text{MgF}_2)_8$ at the B3LYP/6311++G** level . . . . .	139
E.6	Raman frequencies and intensities for global minimum of $(\text{MgF}_2)_9$ at the B3LYP/6311++G** level . . . . .	140
E.7	Raman frequencies and intensities for global minimum of $(\text{MgF}_2)_{10}$ at the B3LYP/6311++G** level . . . . .	140
F.1	Modes of the rutile structure that are Raman active along with their frequencies in $\text{cm}^{-1}$ . . . . .	141
G.1	Energy-Volume curves derived for important structures of bulk $\text{CaF}_2$ found from Monte-Carlo simulated annealing. . . . .	143

## Abstract

A given chemical system, in general, will realize many (meta)stable structures, some of which might be observable on an experimentally viable timescale. Some of these polymorphs could have novel properties waiting to be exploited. However, addressing the problem of directing solid state synthesis towards such unknown polymorphs remains a major challenge. The prediction of new compounds using various theoretical methods is not usually followed up by an actual synthesis and planning the synthesis of novel inorganic solids often requires recourse to theoretical methods that can not only predict the thermodynamic stability of possible structure candidates but also model the kinetic behavior of atoms during the experimental synthesis. Here, we strive to fill this gap between knowledge derived from structure prediction methods and performing the actual synthesis of new structures experimentally by using tools available to the theoretical chemist that include energy landscape search algorithms, ab initio spectroscopy calculations and molecular dynamics simulations with the synthesis of  $\text{MgF}_2$  via the low-temperature atom beam deposition (LT-ABD) method as the model system.

Hence, in a first step, in order to understand the possible cluster modifications of  $\text{MgF}_2$  that can exist in the vapor phase, we perform global optimizations on neutral and charged clusters using Monte-Carlo simulated annealing and find many possible structures. We also explore the energy landscape of  $(\text{MgF}_2)_3$  and  $(\text{MgF}_2)_4$  using the threshold algorithm in order to be able to estimate the stability and dynamics of these clusters. This method allows us to determine not only the stable and metastable isomers but also the barriers separating these isomers and the probability flows among them, yielding estimates of the stability of all the isomers found. We find that there is reasonable qualitative agreement between the ab initio and empirical potential energy landscapes, and important features such as sub-basins and energetic barriers follow similar trends. However, we observe that the energies are systematically different for the less compact clusters, when comparing empirical and ab initio energies. Furthermore, we employ the same procedure to additionally investigate the energy landscape of the tetramer. For this case, however, we use only the empirical potential due to computational limitations.

This is followed by the calculation of Raman and IR spectra including the phonon modes and their intensities, for all the clusters found from the above study. We also calculate IR intensities and phonon modes for all bulk polymorphs of  $\text{MgF}_2$ . This way, we provide the synthetic chemist with a means

to observe possible (meta)stable phases of this system in both the vapor phase and the deposit while performing a deposition experiment on  $\text{MgF}_2$ . The calculated data are compared with in-situ measurements in the LT-ABD apparatus. The  $\text{MgF}_2$  vapor and film are characterized via Raman spectroscopy of the  $\text{MgF}_2$  gas phase species embedded in an Ar-matrix and of the  $\text{MgF}_2$ -films deposited onto a cooled substrate, respectively. We find that, in the vapor phase, there are mostly monomers and dimers of the neutral and charged species present in our experimental setup. Furthermore, the results suggest that in the amorphous bulk  $\text{MgF}_2$ , rutile-like domains are present and  $\text{MgF}_2$  clusters similar to those in the matrix. Finally, peaks at about  $800\text{ cm}^{-1}$ , which are in the same range as the  $A_g$  modes of clusters with dangling fluorine atoms connected to three-coordinated Mg atoms, indicate that such dangling bonds are also present in amorphous  $\text{MgF}_2$  and can be used to track the amorphous to crystalline transition in this system.

Finally, we model the growth of solid  $\text{MgF}_2$  from the gas-phase on an  $\text{Al}_2\text{O}_3$  substrate as it occurs in a real LT-ABD experiment, a hypothetical  $\text{MgF}_2$ -anatase substrate and a  $\text{MgF}_2$ -rutile substrate. The process is studied in all its stages, from the dynamics of  $\text{MgF}_2$  clusters in the gas phase, over their impact on the surface of the cold and hot substrates, and their diffusion on the substrate, to the formation of crystallites. The growth process was analyzed as a function of synthesis parameters including the substrate temperature, deposition rate and types of clusters deposited.

Both high and low rates resulted in the formation of amorphous  $\text{MgF}_2$  deposits. On annealing, we discovered a possible mechanism for the stabilization of the  $\text{CaCl}_2$ -type structure. We find two competing structures in the first few nanoseconds of the deposition related to the  $\text{CaCl}_2$  and  $\text{CdI}_2$  structure types and argue that this competition stabilizes the  $\text{CaCl}_2$ -type structure long enough for experimental observations to take place. Furthermore, the atom arrangements found in our simulations are in good agreement with existing experimental observations based on TEM and XRD measurements, for both the amorphous and the partly ordered metastable phase.

## Zusammenfassung

In einem gegebenen chemischen System können im allgemeinen viele (meta-)stabile Strukturen existieren, von denen einige auf einer experimentell zugänglichen Zeitskala beobachtet werden können. Einige diese Polymorphe könnten neuartige Eigenschaften haben, die der zukünftigen Nutzung harren. Die Lösung des Problems, wie die Festkörpersynthese gezielt auf eine solche Verbindung hingelenkt werden kann, bleibt jedoch eine grosse Herausforderung. Denn auf die Vorhersage neuer Verbindungen durch theoretische Methoden erfolgt normalerweise keine wirkliche Synthese, und die Planung der Synthese von anorganischen Festkörpern benötigt oft den Einsatz von theoretischen Verfahren, die nicht nur die thermodynamische Stabilität von möglichen Strukturkandidaten vorhersagen sondern auch das kinetische Verhalten der Atome während der experimentellen Synthese modellieren. In dieser Arbeit wollen wir den Graben zwischen den Kenntnissen aus der Strukturvorhersage und der tatsächlichen Synthese neuer Strukturen durch den Einsatz von Verfahren überbrücken, die dem theoretischen Chemiker zur Verfügung stehen wie Algorithmen zur Erkundung von Energielandschaften, zur Berechnung von Spektren und für Molekulardynamiksimulationen, wobei die Synthese von  $\text{MgF}_2$  durch die Tieftemperaturabscheidungsmethode (LT-ABD) als Modellsystem dient.

Vom Standpunkt des Modellierers kann man die LT-ABD-Synthese in drei Teile aufspalten: die Erzeugung der Gasphase, die Abscheidung des Gases auf dem Substrat, und das Tempern des abgeschiedenen Films. Um die möglichen Clustermodifikationen von  $\text{MgF}_2$ , die in der Gasphase existieren können, zu verstehen, führen wir als ersten Schritt globale Optimierungen an neutralen und ionischen Clustern unter Verwendung von Simulated Annealing durch und finden viele mögliche Strukturen. Darüber hinaus erkunden wir die Energielandschaft von  $(\text{MgF}_2)_3$  und  $(\text{MgF}_2)_4$  mit dem Thresholdalgorithmus, um die Stabilität und Dynamik dieser Cluster abzuschätzen. Diese Methode erlaubt uns nicht nur die Bestimmung der stabilen und metastabilen Isomere sondern auch der Barrieren, die die Isomere trennen, sowie der Wahrscheinlichkeitsströme zwischen ihnen, welche Abschätzungen der Stabilität aller Isomere liefern. Wir finden eine qualitative Übereinstimmung zwischen der auf ab initio Energien und der auf empirischem Potential basierenden Landschaft, und wichtige Aspekte wie die Unterbassins und die Energiebarrieren folgen ähnlichen Trends. Wir finden allerdings, dass diese Energien sich bei den weniger kompakten Clustern systematisch unterscheiden. Daneben haben wir dasselbe Verfahren angewandt, um zusätzlich die Energielandschaft des Tetramers zu untersuchen.

In diesem Fall haben wir uns wegen des Rechenaufwandes auf das empirische Potential beschränkt.

Der nächste Schritt bestand in der Berechnung der Raman- und Infrarotspektren, einschliesslich der Phononmoden und Intensitäten, für alle Cluster, die in der obigen Untersuchung gefunden worden waren. Zusätzlich berechneten wir die IR-Intensitäten und Phononmoden für alle Bulkpolymorphe von  $\text{MgF}_2$ . Hierdurch stellen wir dem Synthesechemiker eine Methode zur Verfügung, mögliche (meta)stabile Phasen des Systems sowohl in der Gasphase als auch in dem abgeschiedenen Film während eines Abscheidungsexperiments zu beobachten. Die berechneten Daten werden mit den in-situ Messungen in der LT-ABD-Apparatur verglichen. Das  $\text{MgF}_2$ -Gas und der  $\text{MgF}_2$ -Film werden mit Hilfe von Ramanspektroskopie an der in einer Argonmatrix ausgefrorenen Gasphase bzw. an dem auf einem gekühlten Substrat abgeschiedenen Film untersucht. In der Gasphase finden wir vor allem Monomere und Dimere der neutralen und geladenen Spezies. Die Messungen deuten weiter darauf hin, dass in der amorphen Bulkphase bereits rutilartige Domänen vorhanden sind. Schliesslich zeigen Peaks bei etwa  $800\text{ cm}^{-1}$ , die in demselben Bereich wie die  $A_g$ -Moden der Cluster mit isolierten F-Mg-Bindungen an dreifach koordinierte Magnesiumatome liegen, dass solche einfach gebundenen isolierten Fluoratome auch in amorphen  $\text{MgF}_2$  vorliegen und genutzt werden können, um den Übergang von der amorphen zur kristallinen Phase in diesem System zu verfolgen.

Im letzten Schritt modellieren wir das Wachstum des festen  $\text{MgF}_2$  von der Gasphase auf einem  $\text{Al}_2\text{O}_3$ -Substrat, wie es im tatsächlichen Experiment verwendet wird, sowie auf einem  $\text{MgF}_2$ -Anatasssubstrat und einem  $\text{MgF}_2$ -Rutilssubstrat. Der Prozess wird in all seinen Teilschritten untersucht, von der Dynamik der  $\text{MgF}_2$ -Cluster in der Gasphase, über ihr Auftreffen auf der Oberfläche der kalten und heissen Substrate, und ihre Diffusion auf dem Substrat, bis zu der Bildung von Kristalliten. Der Wachstumsprozess wurde als Funktion der Syntheseparameter einschliesslich der Substrattemperatur, der Abscheiderate, und der Art der abgeschiedenen Cluster analysiert.

Sowohl hohe als auch niedrige Abscheideraten führten zur Bildung von amorphen  $\text{MgF}_2$ -Filmen. Beim Tempern entdeckten wir einen möglichen Mechanismus für die Stabilisierung der  $\text{CaCl}_2$ -Struktur. Wir finden zwei im Wettbewerb stehende Strukturen in den ersten Nanosekunden der Abscheidung, die mit der  $\text{CaCl}_2$ - und der  $\text{CdI}_2$ -Struktur verwandt sind, und schliessen, dass dieser Wettbewerb die  $\text{CaCl}_2$ -artige Struktur lange genug stabilisiert, um experimentelle Beobachtungen vornehmen zu können. Darüber hinaus sind die in unseren Simulationen beobachteten Atomanordnungen in guter Übereinstimmung mit den vorliegenden auf TEM und XRD-basierenden Messdaten, und zwar sowohl für die amorphe also auch für die teilweise geordnete metastabile Phase.

# Part I

## Introduction





# 1

## Introduction

### 1.1 Introduction

A given chemical system, in general, will realize many (meta)stable structures that might be observable on an experimentally viable timescale. Some of these polymorphs could have novel properties waiting to be exploited. However, systematically addressing the problem of directing solid state synthesis towards such unknown polymorphs remains a major challenge. While a number of inorganic materials of technological interest have been discovered serendipitously(1), there has been a concentrated effort in the last two decades to rationally synthesize new inorganic materials. At the same time, it has been recognized that the exploration of the space of possible stable and metastable compounds experimentally is not sufficient and must be supplemented by a theoretical effort aimed at predicting new compounds (2, 3, 4, 5, 6, 7, 8, 9, 10). This symbiotic effort has led to the successful prediction(11, 12, 13, 14) and subsequent synthesis of a number of new and exciting compounds(15, 16, 17, 18, 19). However, the prediction of new compounds using various theoretical methods is not usually followed up by an actual synthesis. The failure may be due to a lack of subtle experimental synthesis methods where a number of parameters can and must be tweaked to achieve directed synthesis. While we can often propose a synthesis by analogy to the routes of related compounds, planning the synthesis of novel inorganic solids often requires recourse to theoretical methods that can not only predict the thermodynamic stability of possible structure candidates but also model the kinetic behavior of atoms during the experimental synthesis. In principle, theory can allow us to model existing synthesis routes in atomic detail (20), analyze the various steps involved, and finally aid the experimentalist in his work. Still, in practice, very few experimental methods can be simulated with reasonable accuracy from start to finish.

In this context, the low-temperature atom beam deposition method (LT-ABD) has been found to be particularly successful for the synthesis of previously unknown compounds. This approach has been employed to successfully synthesize new metastable compounds of binary and ternary salts and intermetallics(14, 15, 16). As opposed to conventional deposition methods used for solid-state synthesis, such as molecular beam epitaxy, where the substrate is heated in order to obtain ordered structures,

## 1. INTRODUCTION

---

in LT-ABD, an atomically disperse amorphous deposit is formed on a cold substrate. Crucially, this technique reduces the thermal activation barrier for solid state reactions by shortening the diffusion paths between the reactant molecules. These unique characteristics bring this particular synthesis method within the realm of simulation using advanced Monte-Carlo and molecular dynamics methods.(16)

In this thesis, we strive to model the whole LT-ABD synthesis route for the specific example of alkaline earth halides as realistically as possible. In a previous study on the energy landscape of magnesium difluoride solids, Wevers et al. (21) had suggested the not-yet-synthesized  $\text{MgF}_2$ -anatase structure as a likely structure candidate. On the energy landscape, this modification appears as an isolated basin with a high energetic barrier separating it from the rest of the structures. This indicates that, once synthesized, it might be possible to stabilize this structure on experimentally measurable timescales. This possibility, in particular, makes it interesting to study  $\text{MgF}_2$  as a model system for LT-ABD deposition.

In an earlier investigation, the LT-ABD deposition of Xenon on alpha-alumina was studied using molecular dynamics simulations(22). In this case, a random distribution of Xe atoms was deposited on a cooled  $\text{Al}_2\text{O}_3$  substrate, after verifying that even at rather low temperatures, Xe was still a monoatomic gas. In contrast, in the case of alkaline earth halides, the composition of the vapor phase is expected to play a major role.

So far, in the field of inorganic crystal structure prediction, there has been an overwhelming emphasis on predicting the thermodynamic stability of unknown modifications of various systems(2, 3). This might be sufficient if one explores high-temperature synthesis methods that are expected to yield the thermodynamically stable compound. But, for the LT-ABD synthesis, it is important to understand the kinetic behavior during deposition and subsequent tempering and in this way try to understand different routes that could lead to the same global minimum. As a consequence, in this thesis, we have divided the synthesis route into essentially three steps (See Figure 1.1):

- 1. The formation of small clusters in the vapor phase after evaporation :** This is modeled by a thorough investigation of the energy landscape of neutral  $(\text{MgF}_2)_n$  ( $n=1,3$ ) clusters on the ab initio level (estimation of barriers, stability and probability flows among various isomers)) and an investigation of the empirical energy landscape of ionic species and global minima of bigger cluster configurations. Eventually, we arrive at likely cluster candidates for the gas phase and calculate the Raman and infra-Red spectra on the ab initio level and compare with in-situ Raman measurements for experimental verification.
- 2. Deposition of clusters on  $\alpha\text{-Al}_2\text{O}_3$ ,  $\text{MgF}_2$ -rutile and hypothetical  $\text{MgF}_2$ -anatase :** Neutral dimers and monomers of  $\text{MgF}_2$  are deposited on three different substrates. Parameters that are varied include the substrate temperature, rate of deposition of clusters and the face of the substrate exposed to the deposit.
- 3. Tempering of the deposit :** After a long deposition, we temper this deposit at a constant temperature for a long time to see what kind of ordering is produced. Again, the variable parameters include temperature and face of the substrate exposed to the deposit.

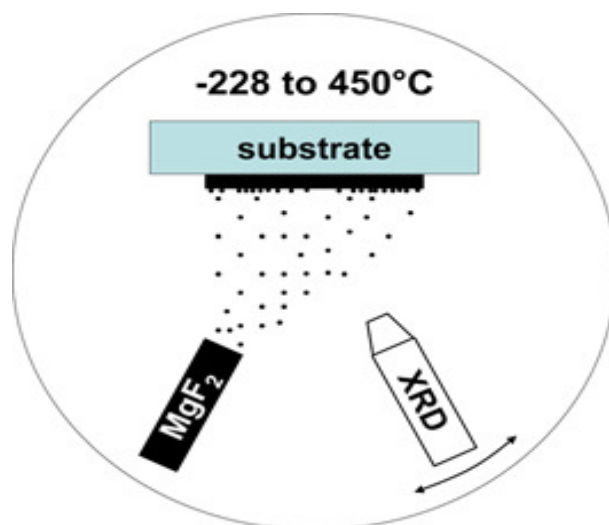


**Figure 1.1: LT-ABD setup**-A schematic representation of the LT-ABD method.

In this manner, we have strived to achieve an optimal combination of various modeling tools that are available to the theoretical chemist. These include a powerful package of stochastic Monte-Carlo energy landscape exploration algorithms (G42), molecular dynamics simulations code for thousands of atoms and Density functional theory based approaches for calculation of energies and vibrational spectra on an ab initio level. We hope that by using such a combination of tools to study the aforementioned three steps of the synthesis route, we will be able to gain further insight into the process of rational synthesis of inorganic solids via the LT-ABD method.

Understanding deposition and crystal growth mechanisms is key to both fundamental and applied sciences. It has been observed that different experimental techniques for synthesis of periodic structures take different paths to the global minimum structure (23). The low-temperature atom beam deposition method(15), has been employed in order to produce both known and novel stable and metastable phases of oxides(24), nitrides(25, 26) and halides(16, 18) that had not been accessible using any alternative synthesis route. The reason for this could be the low thermal activation barrier associated with this technique that slows down kinetics to experimentally observable scales. During low-temperature atom beam deposition, the metal constituents of the desired compound are initially evaporated using thermal effusion cells. Simultaneously, the oxygen molecules, for example, are broken up to form a low-density atomic gas. The oxygen-metal gas thus produced is then deposited on a cold substrate, which is maintained at liquid nitrogen or liquid helium temperature.

In the case of  $\text{MgF}_2$ , an order-disorder transition is observed on annealing the deposit from a low temperature of  $-228^\circ\text{C}$  to  $450^\circ\text{C}$ . A new  $\text{CaCl}_2$  polymorph of  $\text{MgF}_2$  was found using the low-temperature atom-beam deposition technique (18). In this experiment, the  $\text{MgF}_2$  bulk was initially evaporated and using thermal effusion cells at temperatures of 50K to 800K. The molecules are broken up at very low partial pressures of  $10^{-6}$  mbar. The gas produced is then deposited on a cold substrate, which is maintained at very low temperatures using liquid helium or liquid nitrogen. Eventually, an

## 1. INTRODUCTION

---

X-ray amorphous deposit is obtained on the substrate at a low-temperatures. Then, after slowly heating the substrate from the bottom, various (meta)stable modifications are observed during the transition to the global minimum structure.

X-ray amorphous deposits are obtained as a result of this procedure. Finally, upon slow heating, crystals of various stable and metastable modifications are generated. Understanding this procedure is of high scientific and technological interest, due to its unusually high degree of control over the synthesis parameters as compared to most other solid state synthesis methods. The goal of this study is thus to model such a synthesis throughout all its stages with  $\text{MgF}_2$  as a model system.

Molecular dynamics predicts atomic trajectories by direct integration of the equations of motion Newtons second law for classical particles with appropriate specification of an inter-atomic potential and suitable boundary conditions. In this section, I briefly explain a few important aspects of a classical Molecular Dynamics simulation. A comprehensive introduction to MD techniques can be found in Ref.(27).

# Part II

## Background



## 2

# Background

In this section we describe (a) experimental work regarding the system under investigation and (b) pioneering work in the fields of structure prediction of clusters and solids, ab initio spectroscopy and molecular dynamics modeling of vapor deposition techniques that are of relevance to the investigations performed in this thesis. A basic introduction to various methods used in the thesis is also given in some detail.

## 2.1 Brief literature review

### 2.1.1 Experiments on $\text{MgF}_2$

Different physical vapor deposition techniques have been used to synthesize thin films of  $\text{MgF}_2$ . For example, Kennedy et al.(28) studied the optical properties of  $\text{MgF}_2$  films deposited by Ion Beam Assisted Deposition. Atanassov et al.(29) studied the mechanical and structural properties of  $\text{MgF}_2$  films prepared by plasma ion-assisted deposition. Many such studies have since been performed in order to improve the refractive index of thin films of  $\text{MgF}_2$  for anti-reflection properties for solar cells (30, 31).

Experiments directed purely at synthesis of new structures of  $\text{MgF}_2$  are considerably more rare. The low-temperature atom beam deposition carried out by Bach et al. (18) found an unknown  $\text{CaCl}_2$ -type polymorph as a meta-stable state.

Polymorphs other than the rutile-type and the  $\text{CaCl}_2$ -type have been observed experimentally through high-pressure studies of Haines et al.(32).In the latter work, the transition from rutile-type to  $\alpha$ - $\text{CaCl}_2$ -type phase was shown to be second order and probably ferroelastic. They also found the  $\alpha$ - $\text{PbO}_2$  (3GPa),  $\text{PdF}_2$  (3 GPa) and the nine-fold coordinated contunnite phase (35GPa) for the  $\text{MgF}_2$  system. Furthermore, the authors presented a general pathway for high-pressure phases. This was as follows:

## 2. BACKGROUND

---

rutile  $\rightarrow$   $\text{CaCl}_2 \rightarrow \alpha\text{-PbO}_2 \rightarrow \text{PdF}_2$ (modified fluorite)  $\rightarrow \alpha\text{-PbCl}_2$ , with an overall increase in the coordination number of Mg from 6 to 9. The cubic fluorite-type structure was also found to be stable at 30GPa. (33)

Experimental Raman studies on bulk  $\text{MgF}_2$  have been carried out frequently (33, 34, 35, 36). The first Raman spectrum of magnesium fluoride in the rutile type was calculated by Krishnan and Katiyar (34, 35). Subsequently, the vibrational modes were assigned from more accurate data by Porto et al. (36). As far as the vapor phase is concerned, some experimental studies including Raman(37), infra-red(38), and mass spectroscopic measurements(39, 40) have been performed in the past.  $\text{MgF}_2$  and  $(\text{MgF}_2)_2$  clusters have been previously observed and characterized using Raman spectroscopy by Lesiecki et al.(37). However, the assignment of the specific isomer was not conclusively made by any experimental study.

### 2.1.2 Theoretical studies on $\text{MgF}_2$

The energy landscape of bulk  $\text{MgF}_2$  has been studied in detail using simulated annealing and the threshold algorithm by Wevers et al. (21, 41) and various possible metastable modifications at zero pressure were suggested(41, 42, 43). Based on this work, it appears that the anatase-type modification is locally ergodic and should be kinetically stable at the standard conditions. This implies that given the right experimental parameters, it might be possible to generate the yet-unknown anatase polymorph using e.g the LT-ABD method. However, the physical properties of the hypothetical metastable bulk  $\text{MgF}_2$  phases, which could be used for their identification have not yet been studied. In addition, the high pressure phase transition from rutile to  $\text{CaCl}_2$  was studied using molecular dynamics by Zhang et al. (44) and Nga et al.(45) where a shock-induced phase transition from rutile to the cubic fluorite structure was found to take place.

Furthermore, the frequencies of the monomer, two dimers and nine proposed trimers of  $\text{MgF}_2$  have been studied at different levels of theory by Gigli, Axten, Simandiras, Ystenes and Francisco et al. (46, 47, 48, 48, 49, 50). None of the theoretical calculations have included any data on intensities, which would be particularly useful when assigning structures of isomers to experimental data. Furthermore, the possible charged species of  $\text{MgF}_2$  that could appear under experimental conditions in the gas phase have not been studied up to now to our knowledge.

### 2.1.3 Deposition of atoms and clusters on a substrate

Growth processes of solid materials are of great interest from both the fundamental and the technological point of view. Understanding how different growth procedures lead to different polymorphs of the same substance, for instance, is a key issue in natural sciences with many applications in fields as diverse as the electronic, chemical and pharmaceutical industry. Since different modifications of the same material display in



## 2.2 Constructing an energy landscape

---

general different properties(23), it is vital to study the relationship between the synthesis route followed and the resulting morphology of the grown compound.

Although recent progress has made available tools for the microscopy and spectroscopy of solid compounds during the whole growth process (51, 52, 53), atomistic simulations prove invaluable in casting light on the mechanisms which determine the growth mode (54, 55). In particular, molecular dynamics (MD) has been extensively used to study growth processes of materials from both the liquid and the gas phase (56, 57, 58, 59, 60, 61, 62, 63), especially in an attempt to model the experimental conditions occurring during a molecular beam epitaxy experiment(64).

A brief background of the methods used in this thesis are provided in the following subsections.

## 2.2 Constructing an energy landscape

An energy landscape is defined as the hypersurface of (potential) energy over the 3N-dimensional space of configurations of a N-atom chemical system. Thus, the landscape contains all the possible (meta)stable modifications as locally ergodic regions; in particular the local minima of a given chemical system, together with transition paths and energetic barriers between these regions. In practice, the chemical system is defined by a potential that describes all important interactions in this system accurately. The (meta)stable states are essentially local minima on this potential, and the barriers and possible transition paths depend on the form of this potential. Thus, it is crucial to have an accurate potential to describe the given system.

A three-pronged approach is used for the effective exploration of the energy landscape of clusters and bulk systems studied here.

1. Global optimization using e.g. simulated annealing in order to find local minima.
2. A detailed global exploration of the barrier structure using the threshold algorithm.
3. Local optimization of structure candidates on ab initio level.

We note that plenty of methods such as simulated annealing, genetic algorithms, taboo search, lid-based algorithms, basin-hopping, meta-dynamics, swarm-particle optimization, etc. have been developed for the identification of local and global minima and the study of the global barrier structure for chemical systems. These are briefly described in the following subsections. The underlying theme for the global optimization methods is to arrive at the lowest-energy structures in the shortest possible time.

## 2. BACKGROUND

---

### 2.2.1 Global optimization

#### 2.2.1.1 Simulated annealing

Monte-Carlo (MC) methods are essentially stochastic in nature<sup>1</sup>. Here, a walker at configuration  $i$  at time step  $t$  is moved in a particular direction in configurational space (by making e.g an atom exchange move). If this new configuration  $j$  satisfies a pre-defined acceptance criterion, the move is accepted. Else, the move is rejected and the walker stays at the original configuration  $i$ . In classical MC, we use the Metropolis acceptance criterion (65) i.e if the energy of state  $j$  is equal to or below the one for state  $i$ , the move is accepted. If  $E(j) > E(i)$ , then the move is accepted with an exponential probability  $\exp(-(E(j) - E(i))/C)$  where  $E(j)$  and  $E(i)$  are the energies of the final and initial configuration respectively and  $C$  is a control parameter usually corresponding to the temperature  $kT$ . In this way, barriers of height  $C$  can be crossed with a certain probability ( $1/C$ ) while sampling the energy landscape. If the control parameter  $C$  is set to zero, only moves that take the system lower in energy will be accepted. This corresponds to the stochastic quench.

Kirkpatrick et al. developed the simulated annealing algorithm (66) for global optimization. Cerny (67) used this approach to solve the traveling salesman problem(68, 69). Simulated annealing requires a single initial individual configuration as a starting point and a unary search operation. The implementation of this algorithm is quite simple: it corresponds to a lowering of the control parameter  $C$  during a Metropolis walk(65).

Typically, simulated annealing is performed in order to globally explore the energy landscape of the system. The aim is to be able to visit as many interesting configurations of the system as possible in the “shortest” time. Various modifications of this method are available today depending on the problems at hand (4, 68, 69, 70, 71, 72, 73). In the following subsections, we describe other methods used for globally optimizing a system and finding the global minimum on the energy landscape. While not following trajectories as precisely as a molecular dynamics simulation, Monte-Carlo based methods are often preferable for optimization purposes because of their ability to employ large steps on the landscape and thus explore complex landscapes more efficiently. We note that the choice of an efficient combination of moves (the “moveclass”) is of great importance for the success of the optimization.

#### 2.2.1.2 Genetic algorithms

Genetic algorithms are a class of evolutionary algorithms that are inspired by the natural selection rules of Darwinian evolution and use moves derived from evolutionary biology such as inheritance, mutation, natural selection, and recombination (or crossover) to generate new structures (74, 75). The technique was pioneered by J. Holland in 1975 (76). As a first step, many random solutions are generated to form an

---

<sup>1</sup>This method derives its name from the city of Monte-Carlo as it involves the use of random numbers and probabilistic statistics.

initial population.

The population size depends on the nature of the problem, but typically contains several hundreds or thousands of possible solutions. Traditionally, the population is generated randomly, allowing the entire range of possible solutions or atom configurations for chemical systems. Occasionally, the solutions may be “seeded” in areas where optimal solutions are likely to be found. These random seeds are represented in a binary format as a set of 0s and 1s; however for chemical systems, representation in other formats is possible, especially if the configurations are always locally minimized. Many of these solutions are stochastically selected from the whole population and crossed (mutated) with each other to form a new population. The fitness of these populations is evaluated using appropriate fitness tests and this process is repeated iteratively. Eventually, the system of random configurations “evolves” to a population that is the fittest.

When used in the context of constructing energy landscapes, the fitness is usually set equal to the energy of the system where maximum fitness corresponds to minimum energy. Thus, an ensemble of configurations with the lowest energy survives preferentially from one generation to the next. In the process, we find interesting low-energy structures and the global minimum structure is the one with the lowest energy. More details can be found in Ref.(75) and Ref.(77, 78).

### 2.2.1.3 Basin hopping

The basin-hopping method was suggested by David Wales in 1997(79). In this technique, the potential energy surface is transformed into a collection of inter-penetrating staircases. The model exploits the fact that a typical potential energy surface should have a large potential energy gradient and the lowest possible transition state energies or rearrangement barriers. The transformation associates any point in configuration space with the local minimum obtained by a geometry optimization started from that point, effectively removing many transition state regions from the problem. However, unlike other methods based upon hypersurface deformation, this transformation does not change the global minimum. The method is described in Ref.(79) in detail.

A description of other interesting methods used for global optimizations on the energy landscapes of chemical systems can be found in Ref. (4, 70, 80, 81, 82, 83).

## 2.2.2 Exploring the barrier structure

### 2.2.2.1 Threshold algorithm

The threshold algorithm (70) is a stochastic approach for exploring the barrier structure of a chemical system. Starting points of the threshold exploration are the minima obtained from e.g. simulated annealing. For each local minimum, a series of lids slightly above it are chosen. Then, one performs a random walk in configuration space restricting the total energy of the system below the specified lid value. Periodically, multiple quenches are performed from holding points along the walker’s trajectory in

## 2. BACKGROUND

---

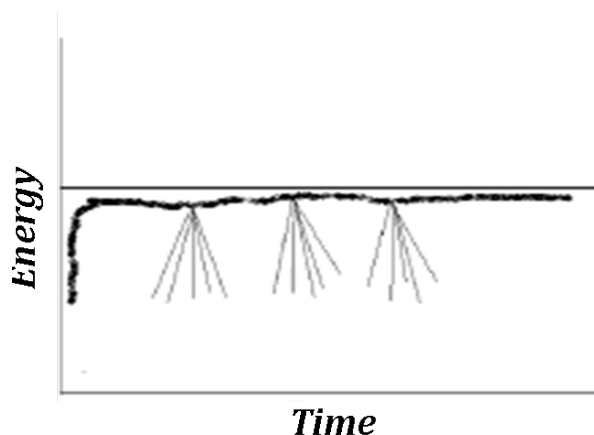


**Figure 2.1: Threshold algorithm** - A schematic representation of the threshold algorithm.

configuration space (c.f. Figure 2.1). For lids slightly above the minimum, the walker typically remains in the vicinity of the starting minimum. On raising the lid beyond a certain threshold, different minima are obtained after the quench. This implies that the energetic barrier for transformation has been breached, and the lid at which this occurs gives an upper limit for the height of the energetic barriers separating the minima. We can also analyze the distribution of local minima found from the holding points as a function of energy lid. This allows an estimate of the size of the transition regions compared to the minimum basins(21). Furthermore, the likelihood to reach a neighboring minimum as a function of lid energy yields a measure of the probability flow in the system (42). Note that if new minima are found during a threshold run, these serve as additional starting points for further explorations.

The move-class for the threshold runs is different from the one used for simulated annealing insofar as atom exchange moves are concerned. Atom exchange moves are unrealistic and correspond to a tunneling through the energetic barrier and hence cause major jumps on the landscape. Thus they are usually excluded from threshold runs.

In addition to the estimates of the energy barriers, the analysis of the frequency with which various minima are reached allows us to construct transition maps at every threshold. These maps show us both the size of basins and transition regions as a function of the threshold value, and provide a measure of the probability flow on the energy landscape which involves energetic and entropic barriers. These also allow us to construct tree-graphs to visualize the interactions among different isomers. The whole procedure is semi-automated and can be applied to systems comprising hundreds of local minima.

### 2.2.3 Free energy

Usually, the structures obtained during experiment are the ones with the lowest free energy (Equation 2.1)

$$F(R) = -k_B T \log(Z)(R) \quad (2.1)$$

Thus, in order to understand which possible (meta)stable states could be observed experimentally, we compute the local free energy for all locally ergodic regions which correspond to these metastable modifications, and identify the ones with the lowest free energy. For low temperatures, it is usually sufficient to consider only the contributions of vibration to the free energy. We note that, mathematically, local free energy is not a continuous function of  $R$ .

## 2.3 Molecular Dynamics simulations

Molecular dynamics predicts atomic trajectories by direct integration of the equations of motion derived from Newton's law for classical particles with appropriate specification of an inter-atomic potential and suitable boundary conditions. In this section, I briefly explain a few important aspects of a classical Molecular Dynamics simulation. A comprehensive introduction to MD techniques can be found in Ref.(27).

### 2.3.1 Force calculations

Force calculations are the most time-consuming part for an MD run. Consider a system with  $N$  particles interacting in a pair-wise fashion. Assuming interactions between a particle and the nearest (periodic) image of another particle, we must evaluate  $N(N-1)/2$  pair distances. Thus, the time required to evaluate forces scales as  $N^2$ . In our particular case, where we model deposition from the vapor phase, we have anything between 6000-15000 atoms in the system. Thus, a fast-pair list construction algorithm (84) is implemented to obtain considerable speed-up and "quasi-linear" scaling with system size under periodic boundary conditions. More details about this algorithm can be found in Ref. (84, 85). A version of this method is also implemented in the popular GROMOS package used for MD simulations of biomolecules.

### 2.3.2 Velocity-Verlet algorithm

The Velocity-Verlet algorithm is used for integrating the equations of motion. Once the forces on all particles have been computed, Newton's equations are solved to construct a trajectory. If  $r(t)$  defines the positions,  $a(t)$  the accelerations and  $r(t - \delta(t))$  are the positions from the previous step, then the equation for advancing the positions is given by 2.2 <sup>1</sup>:

---

<sup>1</sup>See Ref.(27) for details. Notations are taken from this reference.

## 2. BACKGROUND

---

$$r(t + \delta t) = 2r(t) - r(t - \delta t) + \delta t^2 a(t) \quad (2.2)$$

This is derived by adding the Taylor expansions about  $r(t + \delta t)$  and  $r(t - \delta t)$ . By subtracting these expansions, we derive velocities at time step  $t$ . This is shown in equation 2.3. These are very useful for estimating the kinetic energy and hence the system temperature.

$$v(t) = \frac{r(t + \delta t) - r(t - \delta t)}{2\delta t} \quad (2.3)$$

While the positions are subject to errors of the order  $\delta t^4$ , the velocities are subject to errors of the order  $\delta t^2$ .

### 2.4 Electronic structure calculations

In this section, we discuss briefly the first-principles methods used in this thesis. The starting point is the time-independent Schrödinger equation:

$$H\psi = E\psi \quad (2.4)$$

Here  $H$  is the Hamiltonian operator of the system,  $\psi$  is the wave function describing the entire system and  $E$  is the eigen value of the Hamiltonian that corresponds to the total energy of the system. The Hamiltonian for a typical chemical system can be described by

$$\begin{aligned} H_{total} &= \sum_I \frac{p_I^2}{2M_I} + \sum_i \frac{p_i^2}{2m_i} + \frac{1}{2} \sum_{I \neq I'} \frac{ZZ'e^2}{|\vec{X}_I - \vec{X}_{I'}|} \\ &+ \frac{1}{2} \sum_{i \neq i'} \frac{e^2}{|\vec{x}_i - \vec{x}_{i'}|} + \sum_{I,i} \frac{Ze^2}{|\vec{X}_I - \vec{x}_i|} + \text{relativistic corrections} \\ &= T_I + T_e + V_{II} + V_{ee} + V_{Ie} \end{aligned} \quad (2.5)$$

where  $Z$  and  $Z'$  are the charges of the ions labeled by  $I$  and  $I'$ , respectively.  $\vec{X}_I$  and  $\vec{x}_i$  are position vectors of the ions  $I$  and electrons  $i$  respectively,  $M_I$  and  $m_i$  are the masses of ions and electrons, respectively.

#### 2.4.1 Hartree-Fock method

The Hartree-Fock (HF) self-consistent field calculation scheme is a self-consistent iterative variational procedure to calculate the Slater determinant for which the expectation value of the electronic Hamiltonian is a minimum. The method works within the Born-Oppenheimer approximation, i.e. the positions of the nuclei are assumed to be fixed. This means that the nuclear and electronic terms in the Schrödinger equation can be

## 2.4 Electronic structure calculations

---

separated, enabling it to be solved for fixed positions of the nuclei, and the electronic energies are calculated at various internuclear distances. The method was developed for calculations on atoms and later further developed by Pople(86) and others for molecules and solids(87, 88, 89). However, there are a few disadvantages associated with the method. Relativistic effects like spin-orbit coupling are completely ignored. The variational solution is assumed to be a linear combination of a finite number of basis functions, which are usually chosen to be orthogonal and the finite basis set is assumed to be approximately complete.

The starting point for the HF method is a set of approximate one-electron orbitals. For a molecular or crystalline calculation, the initial approximate one-electron wave functions are linear combinations of atomic orbitals (LCAO). This results in a collection of one-electron orbitals that are anti-symmetric. The variational theorem states that for any given time-independent Hamiltonian, any trial wave function will have an energy expectation value that is greater than or equal to the true ground state energy corresponding to the given Hamiltonian. Because of this, the Hartree-Fock energy is an upper bound to the true ground state energy of a given molecule. In the context of the HF method, the best possible solution is at the HF limit; i.e., the limit of the HartreeFock energy as the basis set approaches completeness.

Finding the ground state is actually an optimization problem, where we minimize  $\int \psi^* H \psi dx$  with the condition that only anti-symmetric wave functions are admissible as a result of the Pauli principle (i.e each orbital is occupied by only one electron.) and that the wavefunction is normalized. The algorithm is summarized in Figure 2.2 (90).

A complete discussion of the algorithm and the method can be found in Ref.(91)

### 2.4.2 Density Functional Theory

The main idea of density functional theory is that any property of a system of many interacting particles can be viewed as a functional of the ground state density  $n_o(\mathbf{r})$ . Thus, one scalar function of position  $\mathbf{r}(\mathbf{x}, \mathbf{y}, \mathbf{z})$  determines all information in the many-body wave functions for the ground state and all excited states (91). This offers an elegant formulation of N-particle quantum mechanics, promising conceptual simplicity and computational efficiency. There are, of course, limitations on accuracy from the approximation of unknown terms in the energy functional.

The approach of Hohenberg and Kohn (92) is to formulate density functional theory as an exact theory of many body systems. The formulation applies to any system of interacting particles in an external potential  $V_{ext}(\mathbf{r})$ , including any problem of electrons and fixed nuclei, where the Hamiltonian can be written as :

$$H = \frac{\hbar}{2m_e} \sum_i \nabla_i^2 + \sum_i V_{ext}(r_i) + \frac{1}{2} \sum_{i \neq j} \frac{e^2}{|\mathbf{r}_i - \mathbf{r}_j|}$$

(2.6)

## 2. BACKGROUND

---

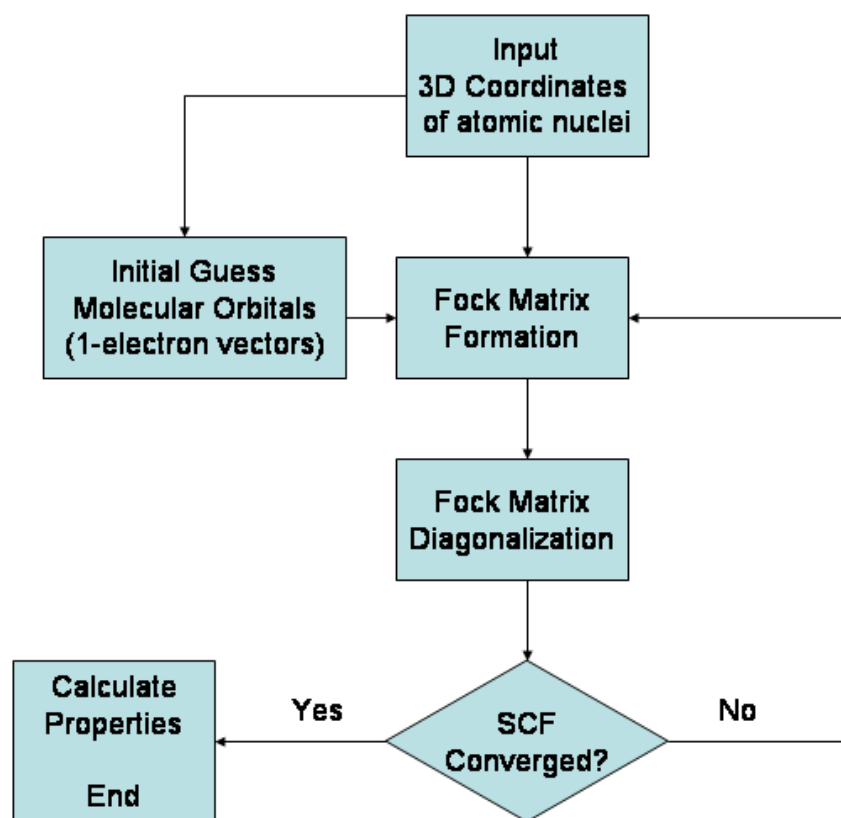


**Figure 2.2: Schematic Hartree-Fock algorithm** - A schematic representation of the Hartree-Fock algorithm.(90)



Next, they proposed the following theorems:

- **Theorem I:** For any system of interacting particles in an external potential  $V_{ext}(\mathbf{r})$ , the potential  $V_{ext}(\mathbf{r})$  is determined uniquely, except for a constant, by the ground state particle density  $n_o(\mathbf{r})$ .
- **Corollary I:** Since the Hamiltonian is thus fully determined, except for a constant shift of the energy, it follows that the many-body wavefunctions for all states (ground and excited) are determined. Thus, all properties of the system are completely determined given only the ground state density  $n_o(\mathbf{r})$ .
- **Theorem II:** A universal functional for the energy  $E[n]$  in terms of the density  $n(\mathbf{r})$  can be defined, valid for any external potential  $V_{ext}(\mathbf{r})$ . For any particular  $V_{ext}(\mathbf{r})$ , the exact ground state energy of the system is the global minimum value of this functional, and the density  $n(\mathbf{r})$  that minimizes the functional is the exact ground state density  $n_o(\mathbf{r})$ .
- **Corollary II:** The functional  $E[n]$  alone is sufficient to determine the exact ground state energy and density. In general, excited states of electrons must be determined by other means.

A detailed discussion can be found in Ref (91).

### 2.4.3 Basis sets

Quantum mechanical calculations are typically performed using a finite set of basis functions. For Hartree-Fock calculations and also some DFT calculations, we use a basis composed of a finite number of atomic orbitals, centered at each atomic nucleus within the solid and interacting through linear combinations (see Ref. (93)). These atomic orbitals were typically Slater orbitals which corresponded to a set of functions which decayed exponentially with distance from the nuclei. In the CRYSTAL'09 framework, these Slater-type orbitals are approximated as linear combinations of Gaussian orbitals instead. This leads to a massive increase in computational efficiency as it is easier to calculate overlap and other integrals using Gaussian basis functions (94).

There are many types of basis sets composed of Gaussian-type orbitals (GTOs). The basis sets containing only occupied orbitals are called minimal basis sets. They are typically composed of the minimum number of basis functions required to represent all of the electrons on each atom. Some basis sets can literally contain dozens of basis functions on each atom. We add or remove diffuse functions on the atomic orbitals corresponding to the sp or d shell in order to describe anions and other soft molecular systems (95, 96, 97, 98, 99). A detailed description of the types of basis sets used and the calculation of energies can be found in the CRYSTAL'09 manual (100).

It must be noted that the interaction energies are susceptible to a basis set superposition error (BSSE). As the atoms of interacting molecules, the basis functions overlap. If the total energy is minimized as a function of system geometry, the short range energies must be compared with the long-range energies from the unmixed sets, and this mismatch introduces error. Thus, there is a need to parameterize the basis

## 2. BACKGROUND

---

sets depending on the system being studied keeping this error in mind.

The most common alternative choice of basis is a set of (very many) plane waves. Parameters that influence the accuracy of the subsequent calculations are the energy cut-off of the plane waves and the k-point mesh over the diffusion zone. In order to reduce the number of waves, one often introduces pseudopotentials that incorporate the effects of the inner electrons. Further details can be found in Ref.(100, 101).

### 2.5 Low-temperature atom beam deposition of $\text{MgF}_2$

Conventional methods for synthesis in the solid state are based on reacting solids which, even after intense milling, are dispersed on a macroscopic scale compared to atomic distances. As a consequence, solid state reactions require a high thermal activation, favoring the formation of thermodynamically stable products. One way to overcome these complications is to reduce the transport distances to atomic dimensions. This idea is realized with the Low-Temperature - Atomic Beam Deposition' (LT-ABD), which allows to disperse the components of the desired product at an atomic level and in an appropriate ratio. Such randomly 'frozen mixtures of atoms could serve as an ideal starting point for solid state syntheses from atoms. The reduction of transport distances also brings this method closer to theoretical methods like molecular dynamics where it is particularly hard to realistically model diffusion processes over long time-scales. For synthesis, several UHV-preparation chambers are used with a special cart-system, which allows sample transfer maintaining vacuum and cooling. This method has been applied successfully to synthesize predicted modifications of halides(16, 18), nitrides(15) and alloys(102).

A summary of the experimental parameter field investigated including substrate temperature, vapor pressure, and sample temperature during X-ray diffraction, is depicted in Figure 2.3. Amorphous  $\text{MgF}_2$  (black dots) is only obtainable at substrate temperatures below  $-100^\circ\text{C}$ . The  $\text{CaCl}_2$  polymorph (red dots) can be formed at  $-80^\circ\text{C}$  already during deposition and is generated at  $70^\circ$  annealing temperature from an amorphous deposit. At deposition temperatures around  $-50^\circ\text{C}$ , distorted rutile type (green) is obtained. The formation of rutile type (blue dots) by annealing clearly depends on the deposition temperature. The lower the substrate temperature during deposition, the higher is the temperature which is needed to form the rutile type. This trend is also true for the other phase transitions from amorphous state via  $\text{CaCl}_2$  to rutile type, which all correspond to displacive and orderdisorder transitions with no clear frontiers noticeable, particularly not between  $\text{CaCl}_2$  and distorted rutile type. (18)

## 2.5 Low-temperature atom beam deposition of $\text{MgF}_2$

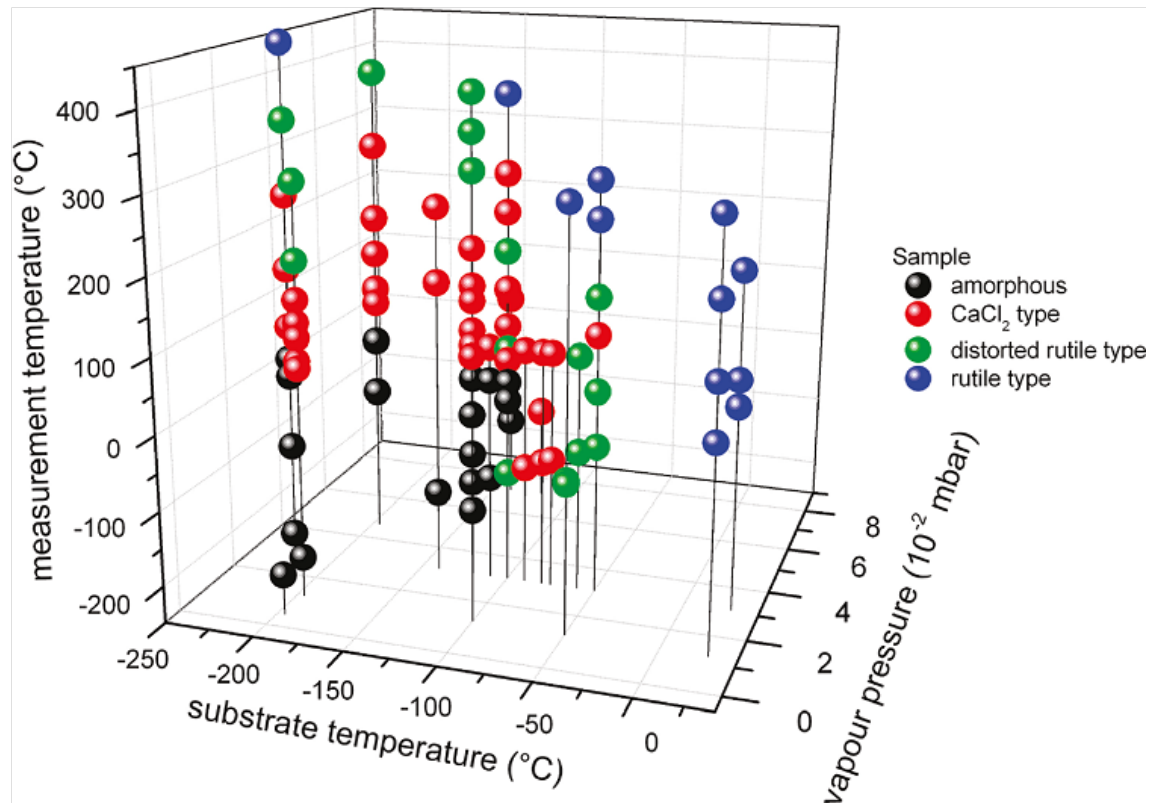


**Figure 2.3: Parameter field for synthesis** - Obtained phases of  $\text{MgF}_2$  as a function of substrate temperature, vapor pressure, and measurement temperature, XRPD results; color code: amorphous  $\text{MgF}_2$  (black),  $\text{CaCl}_2$  polymorph (red), distorted rutile type (green), rutile type (blue); each black line corresponds to one experiment..

## 2. BACKGROUND

---

**Part III**  
**Methods**



# 3

## Methods

### 3.1 Introduction

In this section we describe the various simulation parameters used for the Monte-Carlo, molecular dynamics and quantum mechanical calculations used in this thesis. Also, the parameterization for force-fields that need to be used for performing reasonably accurate empirical potential calculations are described here.

### 3.2 Exploration of energy landscapes

A three-pronged approach is used for the effective exploration of the energy landscape of clusters and bulk systems studied here.

1. Global optimization using simulated annealing in order to find local minima.
2. Detailed global exploration of the barrier structure using the threshold algorithm.
3. Local optimizations on ab initio level.

#### 3.2.1 Global optimization parameters

Global optimization is performed using the simulated annealing procedure (66, 103). During each of the simulated annealing runs, multiple stochastic quenches followed by local optimizations based on analytical gradients are performed to identify possible low-lying minima. The search for minima is followed by a more detailed exploration of the energy landscape, and especially the barrier structure, by the threshold algorithm(70, 104). No symmetry constraints are used during the global optimization. Various parameters associated with the simulated annealing of  $\text{MgF}_2$  clusters and all bulk systems studied are described in Table 3.2.

### 3. METHODS

---

Typically this procedure leads us to thousands of minima. In order to automatically distinguish between various cluster and bulk configurations, we use various symmetry identification routines implemented in the KPLOT code(105). For the clusters, the compare cluster (CCL) algorithm (106) and for periodic structures, the compare cell algorithm (CMPZ)(107) is used, respectively to eliminate duplicates. In the literature (108), very often energies are used to distinguish one structure from another but this fails e.g. in the case of enantiomeric pairs of isomers. However, we find that, in the case of clusters, it is particularly useful to make distinctions based on geometry. As this allows for the possibility of counting the exact number of isomers found as a function of a tolerance parameter. Point group identification of clusters is performed using the SYMMOL code(109) and the space group identification for bulk structures is done via the RGS algorithm (110). These algorithms allow us to eliminate duplicates and assign space groups/point groups after the global optimization runs are complete.

## 3.3 Energy calculations

### 3.3.1 Potentials

During the Monte-Carlo simulated annealing and threshold runs for  $\text{MgF}_2$  clusters using empirical potentials, all single-point energy calculations were performed using the GULP code(111). The Coulomb-plus-Buckingham-type potential derived by Catti et al.(112) was used for the magnesium fluoride clusters and during MD simulations of  $\text{MgF}_2$ . This is described in Equation 3.1. The Coulomb-plus-LJ type potential described in Eq.3.2 was used for the simulated annealing on periodic structures and in MD runs as well. The interactions between atoms of the  $\text{MgF}_2$  deposit and the  $\text{Al}_2\text{O}_3$  substrate were also modeled using this potential.

$$E_{ij} = \frac{Z_i Z_j}{r_{ij}} + b_{ij} \exp\left(\frac{-r_{ij}}{\rho}\right) - \frac{d_{ij}}{r_{ij}^6}. \quad (3.1)$$

$$V_{ij} = \frac{Z_i Z_j}{r_{ij}} + \epsilon \left( (\sigma/r_{ij})^{12} - (\sigma/r_{ij})^6 \right) \quad (3.2)$$

The  $\sigma$  term was chosen as the sum of the ionic radii of the interacting ions, and the epsilon term was set to 0.05. Interactions within the substrate were modeled using the pairwise Coulomb-plus-Buckingham potential suggested by Bacorisen et al. (113) for  $\text{Al}_2\text{O}_3$  and Catti et al. for  $\text{MgF}_2$ (112). Parameters for individual interactions are shown in Table 3.1. The interactions between the substrate ( $\text{Al}_2\text{O}_3$ ) and the vapor phase (clusters of  $\text{MgF}_2$ ) was described by a Coulomb-plus-Lennard-Jones type potential. The potential for  $\text{MgF}_2$  was derived to reproduce the lattice constants and elastic constants of the bulk  $\text{MgF}_2$  rutile structure. Given that our system is periodic in two-dimensions, a treatment of the Coulomb term in the Coulomb-plus-Buckingham type potential within the Ewald scheme was computationally expensive. Therefore, we opted for the damping procedure proposed by Wolf et al. (85) which has the advantage



**Table 3.1:** Potential parameters used for Molecular Dynamics and Monte-Carlo simulations for  $\text{MgF}_2$  and  $\text{Al}_2\text{O}_3$ .

i,j	A(eV)	Rho(Angstroms)	C(AeV)
Mg-F	905.517	0.215	0.5557
F-F	17039.097	0.215	15.168
Mg-Mg	4166.274	0.215	0.5557
Al-O	1374.79	0.301	0.0
O-O	9547.96	0.219	32.0

of being applicable to systems with arbitrary geometry, without introducing a significant error into the potential calculation. The parameters for both the systems are described in Table 3.1. Also, given the scale of this simulation on a single processor, we implemented the fast pair-list construction algorithm as described by Heinz and Huhenberger(84). The epsilon-term was fixed at 0.05 eV and the  $\sigma$ -terms were derived from the sum of ionic distances as described in the literature (27). The 12-6 term of the LJ-type potential is not expected to play a significant role as far as the total energies are concerned as the Coulomb term is typically 8-10 times greater than the L-J term (114).

#### 3.3.2 Ab initio energy calculations

The CRYSTAL'09 package (100, 115) was used for performing ab initio calculations of energies at different levels of accuracy. Here, the fundamental approximation is the expansion of the single particle wave functions as a linear combination of Bloch functions defined in terms of local functions. These local functions are defined as linear combinations of Gaussian type functions. The exponents and coefficients of these Gaussian type functions are defined in the input in the form of a basis set.

In the final local optimizations of the minima, for magnesium and fluorine the basis sets using Valenzano et al. (116) and Nada et al. (117) were chosen, respectively. After local optimization with tight parameters, the lattice constants of the rutile-type  $\text{MgF}_2$  structure were found to be reproduced accurately. Similarly, for calcium, the basis set from Kaupp et al. (118, 119) was used as starting point for energy calculations.

Using the CRYSTAL program, we can solve both Hartree-Fock (restricted and unrestricted) and Kohn-Sham equations with local and hybrid functionals. Various exchange functionals used in DFT such as LDA, Becke, PWGGA, PBE, etc. and correlation functionals such as PZ, LYP, VWN, etc. can also be calculated. Also, hybrid HF-DFT functionals such as B3Pw, B3LYP and other user-defined hybrid functionals can be calculated. (100)

### 3. METHODS

**Table 3.2:** Typical simulation parameters for simulated annealing and threshold runs, using ab initio and empirical energy functions; in case of threshold runs, the number of runs, minima etc. refers to the number per starting point per threshold

Parameter	Simulated annealing		Threshold	
	Empirical	Ab initio	Empirical	Ab initio
Init. vol. factor	100	3	n.a.	n.a.
Minim. dist. allowed	0.55Å	0.7(r <sup>+</sup> + r <sup>-</sup> )	0.55Å	0.7(r <sup>+</sup> + r <sup>-</sup> )
Steps/run	10 <sup>6</sup>	5000	125x10,000	5x7,000
No. of runs	1	50	1 125	15
Holding points/run	400	1	125	5
Quenches / holding point	3	1	5	5
Length of quench run	10,000	10,000	10,000	7,000
$T_{init}$ (eV/atom)	1.0	1.0	n.a.	n.a.
$T_{final}$ (eV/atom)	0.006	0.78	n.a.	n.a.
Moveclass (translation, atom exchange, cell vectors %)	80,10,10	80,10,10	90,0,10	90,0,10
Symmetry constraints	none	none	none	none
No. of minima / run	1200	1	625	25

CRYSTAL'09 can be used for both 3-D periodic systems and 1-D periodic systems. Also, it is especially useful for studying 2-D periodic slabs and surfaces. Local optimizations that include full optimization of cell parameters and atomic coordinates, calculation of vibrational modes and infra-red intensities are other useful qualities that we have exploited.

During the simulated annealing and threshold runs, there is a need for a speed-up and it is needed that energies of largely low-symmetry random configurations are calculated quickly. This is done by loosening the parameters for accuracy. Specifically, in the case of the MgF<sub>2</sub> trimer, several approximations needed to be made in order to allow faster calculation of the energies. In the Mg basis, the diffuse Mg sp shell (exponent 0.28) and the Mg d-shell (exponent 0.5) were not considered. Also, the thresholds from the integral selection were reduced from the default values (10<sup>-6</sup>, 10<sup>-6</sup>, 10<sup>-6</sup>, 10<sup>-6</sup>, 10<sup>-12</sup>) to 10<sup>-4</sup>, 10<sup>-4</sup>, 10<sup>-4</sup>, 10<sup>-4</sup>, 10<sup>-8</sup>. The convergence threshold on the self-consistent field cycles was reduced from the default (10<sup>-7</sup>  $E_h$ ) to 10<sup>-3</sup>  $E_h$ . It is shown in Figure 3.1 that these approximations have a negligible effect on the energies of the MgF<sub>2</sub> trimer. This is important to note because the barrier energy estimates are also made in the smaller basis.

## 3.4 Calculation of Raman and IR spectra

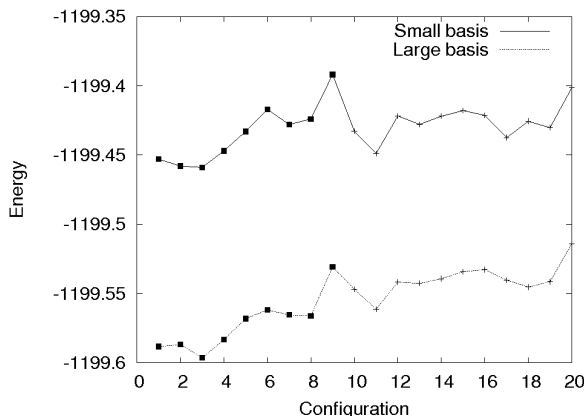


**Figure 3.1:** Effect of basis- Effect of reducing the basis set and applying loose parameters for speed-up.

## 3.4 Calculation of Raman and IR spectra

### 3.4.1 Clusters

For clusters, we calculate both Raman and IR intensities using the Gaussian'03 suite. Calculations were performed using the three-parameter hybrid functionals of Becke and the correlation functional of Lee, Yang, and Parr B3LYP(120). Geometries were optimized using the Berny algorithm(121) with very tight optimization parameters, and vibrational frequencies were then computed by determining the second derivatives of the energy with respect to the Cartesian nuclear coordinates. Vibrational frequencies are computed by determining the second derivatives of the energy with respect to the Cartesian nuclear coordinates and then transforming to mass-weighted coordinates. Finally Raman and IR intensities were produced by numerical differentiation of dipole derivatives with respect to the electric field (122). No scaling factors of any kind were used as the trends in frequencies remain constant and the experimentally known frequencies were well reproduced for the  $\text{MgF}_2$  monomer.

### 3.4.2 Periodic systems

For the periodic crystals, Raman active and IR active phonon modes were identified and the IR intensities were calculated using the CRYSTAL'09 program(100, 115). For magnesium, the basis sets from Valenzano et al. (116) and for fluorine the basis sets from Nada et al. (117) were chosen. The lattice constants of the rutile-type modification of bulk  $\text{MgF}_2$  were well reproduced and the Raman active frequencies predicted for the rutile polymorph were also within error limits. We also compared the energies, bond lengths and frequencies with experimental measurements from Porto et al (36). In these calculations, the IR intensity and Raman activity of the vibrational modes are determined from the changes in the electric dipole moment and the polarizability

### 3. METHODS

---

tensor with the oscillations of the atoms (123).

The reasons for using Gaussian'03 and CRYSTAL'09 for evaluating the Raman spectra of clusters (up to 10 units of  $\text{MgF}_2$ ) and solid  $\text{MgF}_2$ , respectively, were the following: For non-periodic structures, Raman intensities can be calculated using Gaussian03, but this is not possible with CRYSTAL'09. Also, Gaussian'03 is faster for non-periodic systems as it has analytical second derivatives. On the other hand for periodic systems, we found CRYSTAL'09 to be preferable to Gaussian'03 as the latter cannot handle all the symmetries, e.g. only the ones like mirror planes, but not a threefold rotation axis. Therefore it is beneficial to use CRYSTAL'09 as it can handle any space group or point group symmetry in the solid state.

### 3.5 Molecular Dynamics simulations

After establishing the contents of the vapor phase using the methods above, we proceeded to perform molecular dynamics simulations. The details of the potentials used for MD simulations have been discussed in Section 3.3.1. Depositions were carried out at temperatures of 10K, 50K, 300K, 500K and 1000K and the MD time step varied between 2fs to 6fs.

The procedure for modeling the LT-ABD setup was the following. We first constructed substrates and these were equilibrated at temperatures ranging from 50K to 1000K. The time-step of each MD step was varied from 2fs to 6fs. We also tested the effect of annealing at high-temperatures after generating a 12000 atom amorphous deposit of larger clusters of up to 30 atoms on the  $\text{Al}_2\text{O}_3$  substrate.

A schematic of all the interacting functions in the MD code can be seen in Figure 3.2.

### 3.5 Molecular Dynamics simulations

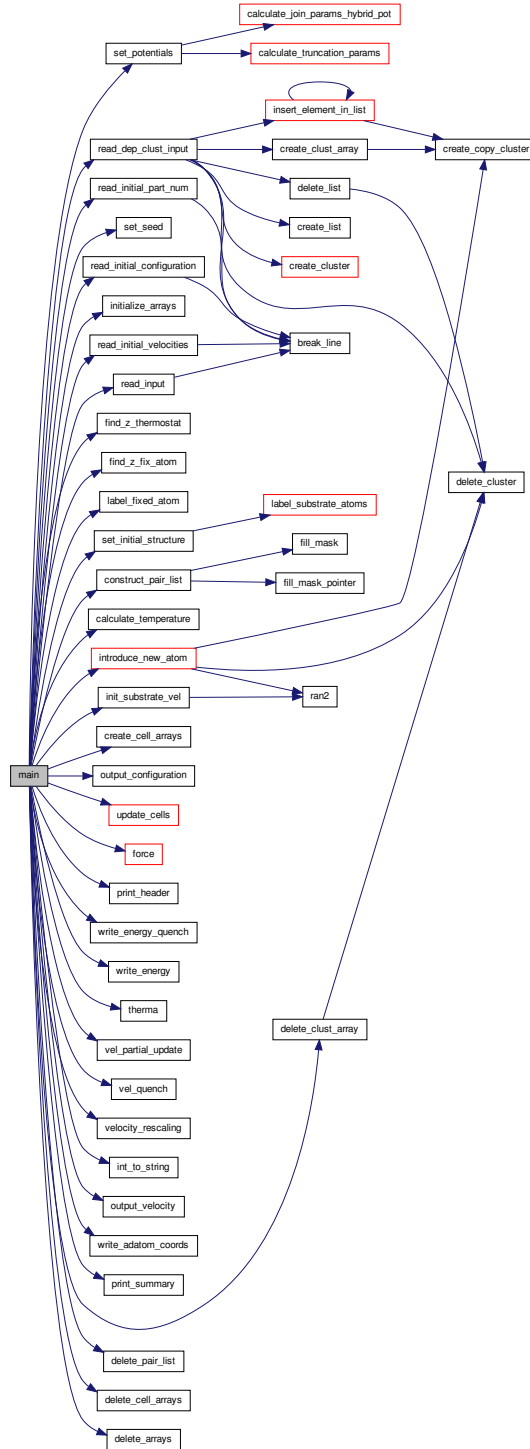


**Figure 3.2: MD code-** The figure shows how various functions in the MD code interact with each other.

### 3. METHODS

---

## Part IV

# Energy landscape investigations on $\text{MgF}_2$





# 4

## Exploration of the energy landscape on $\text{MgF}_2$

### 4.1 Bulk $\text{MgF}_2$

The whole synthesis LT-ABD route has been modeled with the  $\text{MgF}_2$  system as a model. We start with reproducing the earlier result of the investigations by Wevers et al. (21, 41, 42) on the  $\text{MgF}_2$  landscape by performing long simulated annealing runs with a simple Coulomb-plus-Lennard-Jones potential. We have used 2, 3 and 4 formula units of  $\text{MgF}_2$ ,  $10^6$  annealing steps followed by 50000 quench steps. The minima found agreed with those identified earlier. The  $E(V)$  curves of all the important structures found from these runs are plotted in Figure 4.1. The system was annealed from a temperature of 1eV ( $\approx 11,600\text{K}$ ). During the simulated annealing, 42 different structure types were found. The crystal structures were distinguished using the cmpz algorithm (107) as implemented in the KPLOT program (105) using default tolerance parameters.

The structures were further locally optimized at the B3LYP level. The fractional coordinates and lattice parameters of the fully optimized structures are shown in Table 4.1. With longer runtime and ab initio local optimizations, this is an improvement on the previous work and more accurate lattice parameters and fractional coordinates are derived that are shown in Table 4.1 for the various structures that were suggested.

Very often, a structure that appears to be metastable with the Coulomb-plus-Lennard-Jones potential, relaxes to a different structure after optimizing with tight parameters on the ab initio level. Specifically, the  $\text{CaCl}_2$ -type polymorph transformed into the rutile-type structure on local optimization with tight parameters. Thus, at 0 Pa, this structure is not thermodynamically stable and must relax to the rutile-type.

Next, the energy as a function of volume curves were fitted to the Birch-Murnaghan equation (See Figure 4.1). These  $E(V)$  curves calculated for the kinetically stable modifications show that the anatase-type structure should be synthetically accessible for

## 4. EXPLORATION OF THE ENERGY LANDSCAPE ON $\text{MgF}_2$

---

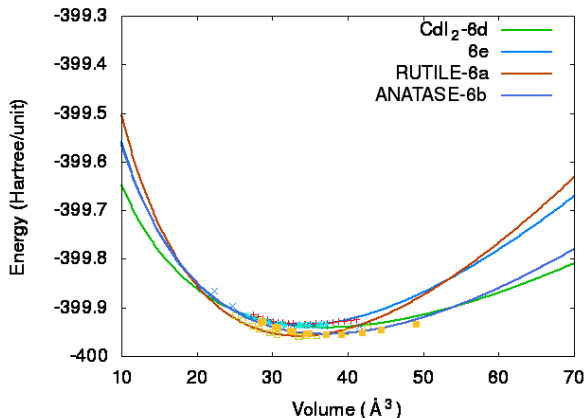


**Figure 4.1: E(V) curves-** E(V) curves fitted to the Birch-Murnaghan equation. Energies from a fully ab initio local optimization of structures found from simulated annealing.

the  $\text{MgF}_2$  system.

## 4.2 Detailed energy landscapes of neutral $(\text{MgF}_2)_n$ ( $n=3, 4$ ) clusters

### 4.2.1 Local minima and energies

As a first step in modeling the LT-ABD synthesis of  $\text{MgF}_2$ , we study the energy landscape of neutral  $\text{MgF}_2$  clusters. Using the threshold algorithm, we performed extensive searches for local minima on the energy landscapes of the dimer, trimer and the tetramer on an empirical potential level and of the dimer and trimer on the ab initio level, respectively.

Figure 4.3 gives an overview over the minimum structures found using simulated annealing and the threshold algorithm in the  $(\text{MgF}_2)_3$  system. The structures are labeled in increasing order of energies as predicted by the empirical potential.

For both the empirical and ab initio simulated annealing, the biggest basin belonged to structure 3 ( $D_{2d}$ ). Structures 5 and 6 look nearly identical; however, in structure 6, the six-member ring is planar ( $C_{2v}$ ), whereas in structure 5 ( $C_s$ ) it is not. The energies of these two minima are considerably different. Note that structure 9 has one imaginary frequency ( $-3 \text{ cm}^{-1}$ ) in the vibrational spectrum. It is possible that with a higher level of theory, a negative frequency does not occur at all. All these structures have previously been reported (48), where short range interatomic potentials had been derived from the electron gas model

## 4.2 Detailed energy landscapes of neutral $(\text{MgF}_2)_n$ ( $n=3, 4$ ) clusters

**Table 4.1:** Lattice parameters and atomic coordinates for optimized bulk structures as obtained from CRYSTAL09.

Minimum	Space Group	Cell Constants(a,b,c, $\alpha,\beta,\gamma$ )	Atom	x	y	z
Rutile(6a)	P42/MNM (136) tetragonal	a=4.646, b=4.646, c= 3.107 $\alpha = 90, \beta = 90, \gamma = 90$	Mg	0.000	0.000	0.000
			F	0.303	0.303	0.000
Anatase(6b)	I41/AMD (141) tetragonal	a=3.877, b=3.877, c=9.930 $\alpha = 90, \beta = 90, \gamma = 90$	Mg	0.000	0.000	0.000
			F	0.000	0.000	0.208
$\text{CaCl}_2$ <sup>1</sup>	PNNM (58) orthorhombic	a=4.592, b=4.938, c=2.959 $\alpha = 90, \beta = 90, \gamma = 90$	Mg	0.000	0.000	0.000
			F	0.275	0.325	0.000
$\text{CdI}_2$ (6d)	P-3M1 (164) hexagonal	a=3.156, b=3.156, c=4.804 $\alpha = 90, \beta = 90, \gamma = 120$	Mg	0.000	0.000	0.500
			F	1/3	-1/3	-0.318
5-fold (5a)	P21/M (11) monoclinic	a=9.087 b=3.857 c=6.332 $\alpha = 90, \beta = 90, \gamma = 90$	Mg	0.139	0.250	0.499
			Mg	0.360	0.250	0.000
			F	0.250	0.250	0.250
			F	-0.085	0.250	-0.499
			F	0.250	0.250	-0.250
6e	CMC21(36) orthorhombic	a=3.0255, b=6.585, c= 6.732 $\alpha = 90, \beta = 90, \gamma = 90.00$	Mg	0.000	0.293	-0.251
			F	0.000	0.008	0.296
			F	0.0	-0.278	-0.445
6c	P4/mmm(123) tetragonal	a=3.029 b= 3.029 ,c=3.742 $\alpha = 90, \beta = 90, \gamma = 90$	Mg	0.000	0.000	0.000
			F	0.500	0.500	0.000
			F	0.000	0.000	0.500

<sup>1</sup>These lattice parameters are not for the locally optimized structure. Ref.(124).

(EGM) of Gordon and Kim (125) and followed by a Monte-Carlo growing strategy and optimization by Powell's quadratically convergent method was employed. Our simulated annealing approach coupled with the threshold algorithm also found the same structures.

For a comparison, the energies of the minima were computed using several energy functions (empirical potential, B3LYP, HF and LDA). These have been summarized in Table 4.2 and Figure 4.2. In general, the pair potential favored the more compact structure 1 ( $C_s$ ) with relatively high coordination numbers, whereas all quantum mechanical methods predicted planar structure 3 ( $D_{2d}$ ) as the global minimum. This is reasonable, since the pair potential had been calibrated for bulk  $\text{MgF}_2$  modifications. Figure 4.2(b) shows the relative energy of the tetramer cluster configurations with respect to the global minimum. While the ab initio trimer energy differences are relatively well reproduced by the pair potential, this does not apply to the same degree to the tetramer molecule in the high-energy range. These are the structures with a low coordination number.

Since the volume of the cell is approximately 100 times the volume of the atoms, we also observe the formation of fragments ( $(\text{MgF}_2)_2 + \text{MgF}_2$ ) during the simulated annealing runs. Typically, these minima lie very high on the energy landscape. We have not considered such structures when performing the threshold analysis as large energetic barriers need to be overcome to achieve any transitions from the  $(\text{MgF}_2)_3$  minimum configurations to fragmented structures. However, these fragments do occur frequently in the simulated annealing runs on both the ab initio and the empirical energy landscape. The fragmentation energies of such molecules have been thoroughly studied using both theory and experiment in the past. (47, 126, 127).

#### 4. EXPLORATION OF THE ENERGY LANDSCAPE ON $\text{MgF}_2$

---

**Table 4.2:** Energies(eV/atom) of structures and frequency of occurrence in simulated annealing runs for  $(\text{MgF}_2)_3$ ; percentages refer to occurrence in empirical potential (ab initio energy) runs

Structure	Empirical	DFT-B3LYP
1 ( $C_s$ )	-6.4377	-9.1254 (2)
2 ( $D_{3h}$ )	-6.4279	-9.1206 (3)
3 ( $D_{2h}$ )	-6.4268	-9.1499 (1)
4 ( $C_s$ )	-6.4247	-9.1100 (4)
5 ( $C_s$ )	-6.4029	-9.0643 (5)
6 ( $C_{2v}$ )	-6.3607	-9.0456 (8)
7 ( $C_s$ )	-6.3933	-9.0561 (7)
8 ( $C_{2v}$ )	-6.3997	-9.0583 (6)
9 ( $C_s$ )	-6.2980	-8.9516 (9)
fragments	n.a.	n.a.

---

\*The remaining 1.5% we see the occurrence of fragment  $(\text{MgF}_2)_2 + \text{MgF}_2$

## 4.2 Detailed energy landscapes of neutral $(\text{MgF}_2)_n$ ( $n=3, 4$ ) clusters

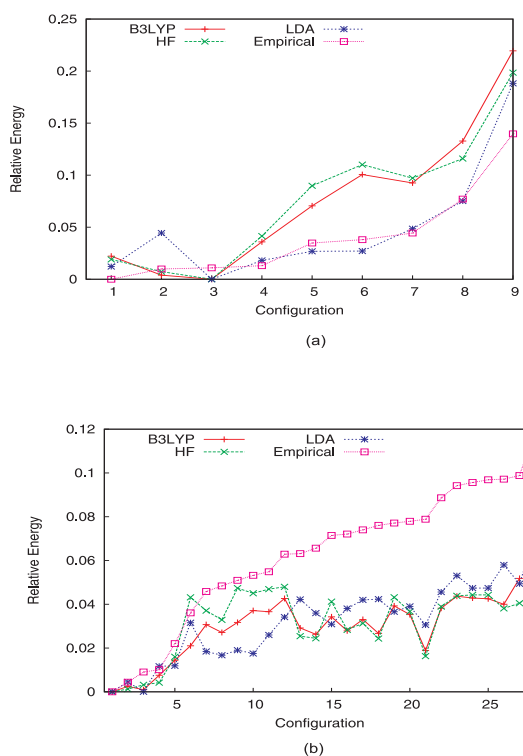


**Figure 4.2:** Relative energies on empirical potential and ab initio level (HF, DFT-LDA, DFT-B3LYP) for cluster configurations with respect to the global minimum for the trimer (a) and tetramer (b), respectively. For the ab initio calculations, the Large basis set was used.

## 4. EXPLORATION OF THE ENERGY LANDSCAPE ON $\text{MgF}_2$

---

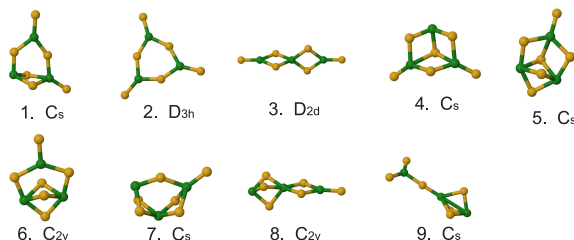


**Figure 4.3:** Isomers of  $(\text{MgF}_2)_3$ - Labeled in increasing order of energy derived from the pair potential.

The global optimization on ab initio level was quite efficient: In the 50 relatively short simulated annealing runs using ab initio energies, we found 5 of the 9 structures (1, 2, 3, 4 and 9), whereas the search of the empirical landscape during the five long simulated annealing runs with empirical potential produced only 4 of the 9 structures. All the structures shown in Figure 4.3 were found during the threshold runs. This result underlines the fact that it is not sufficient to perform just a few long simulated annealing runs with many quenches along the way, since these few runs do not efficiently explore the landscape globally although they tend to do a very good job finding the deepest minimum in the sub-regions visited. Minimum no. 3 was found to be the most common one (88.75% for empirical and 30% for ab initio calculations, respectively) in the simulated annealing runs.

The results from the simulated annealing runs are presented in Table 4.2.

### 4.2.2 Energetic barriers - $(\text{MgF}_2)_3$

The barrier structure of the landscape was analyzed using the threshold algorithm. We compared the barriers both for empirical and ab initio methods (B3LYP functional with the smaller basis set). During the threshold run, energies were computed using less accurate ab initio parameters, and hence the energies of local minima were computed at this level. These energies were used to calculate the barriers in figure 4.4, which separate the individual minima from the global minimum.

Tree-graph models as simplified representations of the empirical (Figure 4.5a) and ab initio (Figure 4.5b) landscapes were constructed. Despite some differences in the energy rankings of the minima, the tree-graphs look qualitatively similar, in particular exhibiting the same sub-basins ((4,1), (6,5) and (8,3)).

The essentially linear  $D_{2d}$  structure 3 shows the highest energetic barrier towards the rest of the landscape both at the empirical and the DFT level. Also, the energetic barriers for transition to the global minimum predicted by ab initio methods are generally greater than the barriers predicted by empirical methods (see Figure 4.4). In particular, the barriers for the 4-1 and 2-3 transitions are much higher for ab initio calculations (0.097 and 0.08, vs. 0.221 and 0.232 eV per atom, respectively). It is not clear, why such a big gap appears for these two particular transitions. For the (8, 3) and (6, 5) sub-basins, the ab initio barriers calculated are 0.102 eV per atom and 0.024

## 4.2 Detailed energy landscapes of neutral $(\text{MgF}_2)_n$ ( $n=3, 4$ ) clusters

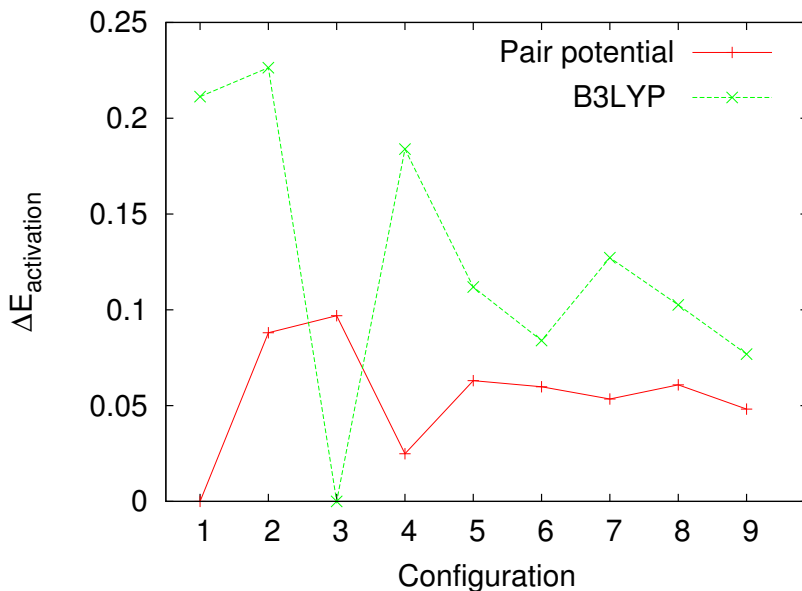


**Figure 4.4: Energetic barriers** - Energy barriers for transition from local minima to the global minimum for the trimer. Overall, the barriers determined on ab initio level (B3LYP, green) are higher than those on empirical potential level (red).

eV per atom respectively. Analogous calculations with the empirical pair-potential indicate a barrier of 0.061 eV per atom and 0.050 eV per atom. As an exception from the general trend, for the 65 transition, we find that the empirical barrier is greater than the one predicted by ab initio methods.

### 4.2.3 Energetic barriers - $(\text{MgF}_2)_4$

The tree-graph representation for the tetramer is shown in Fig 4.6. This particular tree-graph can be characterized as being of the willow-tree kind(128). The deepest super-basin contains structures 1, 2, 3, 4 and 14 that are stabilized by a bridged eight-membered ring consisting of 4 Mg and 4 F atoms, and the transformations among them involve only deformations of the octagonal ring. Analogous to the case of the trimer, the energetic barriers surrounding the linear isomer 21 ( $D_{2h}$  symmetry) are very high. This particular structure does not interact with any other local minimum on the landscape up to the highest lid investigated (0.32 eV per atom). Furthermore, isomers 22, 23 and 28 also exhibit high barriers for transitions to neighboring minima.

### 4.2.4 Probability flows - $(\text{MgF}_2)_3$

Along with estimates of the energetic barriers, the threshold algorithm also provides important information about the stability of the minima and basins by determining the

#### 4. EXPLORATION OF THE ENERGY LANDSCAPE ON $\text{MGF}_2$

---

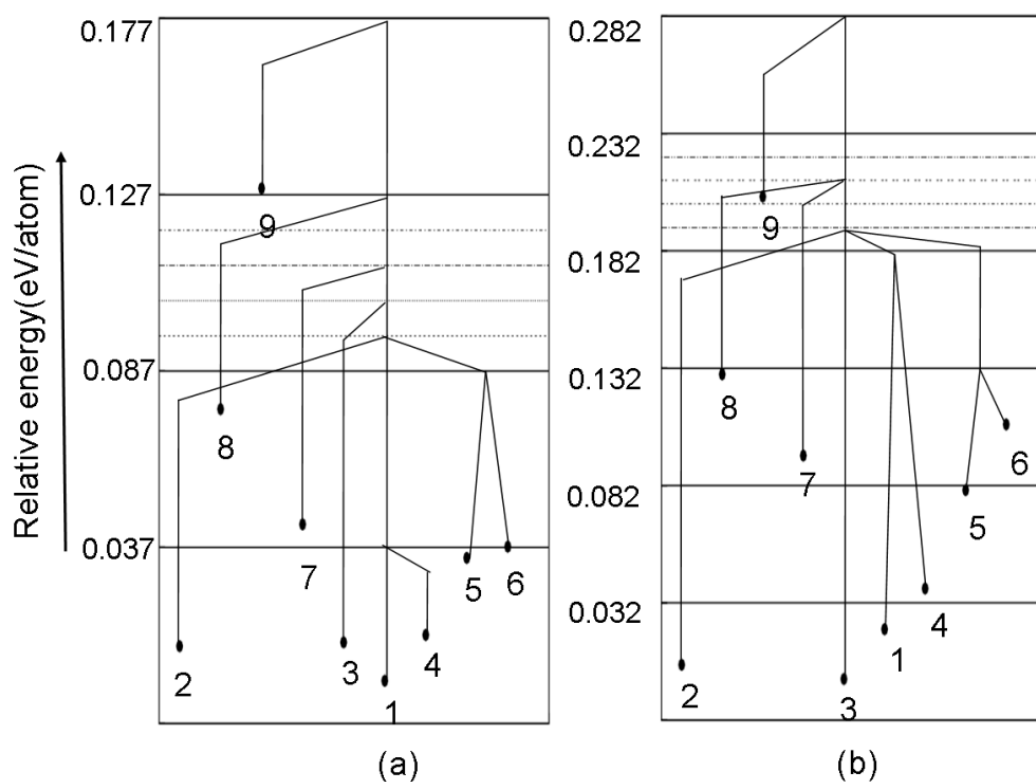


**Figure 4.5: Tree-graph representations** - Tree-graph representations of landscapes derived from (a) empirical and (b) ab initio energies.



## 4.2 Detailed energy landscapes of neutral $(\text{MgF}_2)_n$ ( $n=3, 4$ ) clusters

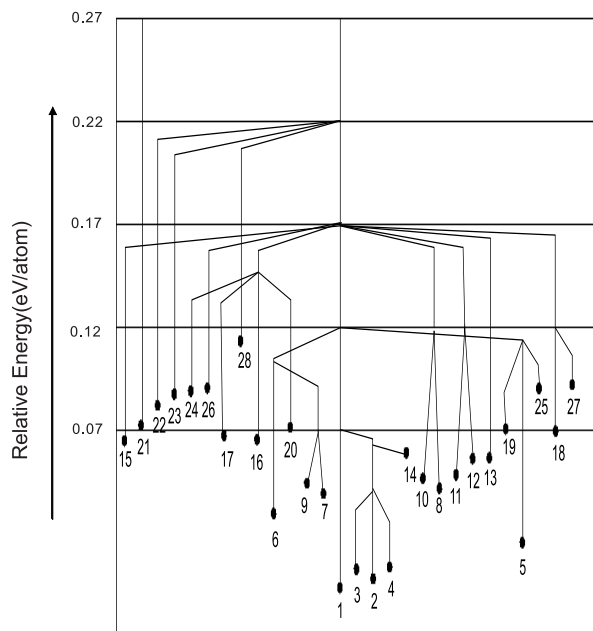


**Figure 4.6: Tree-graph representation of tetramer** - Tree-graph representations of landscapes derived from the empirical potential for the tetramer.

likelihood of a given minimum configuration to transform to a new minimum configuration after a certain energy barrier is crossed. A summary of these probability flows for the trimer can be found in Figure 4.7. Reliable data is available for the empirical methods (a total of 18,750 minima generated). For the sake of completeness, we also present the probability flow charts for ab initio threshold runs (850 minima generated).

From Figure 4.7 (a) we see that as the threshold is raised, new minima begin to occur. For the empirical threshold runs, the first transition we see is at a threshold of 0.037 eV above the global minimum (threshold, empirical, 1<sup>st</sup> transition: TE1). This occurs from isomer 4 ( $C_s$ ) to isomer 1 ( $C_s$ ) with a very small probability (0.5%). On raising the threshold by 0.05 eV/atom (TE2 = 0.087 eV/atom), we observe a transformation of isomer 5 ( $C_s$ ) to isomer 6 ( $C_{2v}$ ). The figure also shows that while the transformation from 5 to 6 is unlikely (0.96%), one from 6 to 5 occurs more readily (50%). On increasing the threshold by a further 0.05 eV/atom (TE3 = 0.137 eV/atom), many minima begin to interact. Structures 2, 5, 6, 7 and 8 now transform to the global minimum with various probabilities. Isomers 8 ( $C_{2v}$ ) and 3 ( $D_{2d}$ ) especially interact at this threshold: about 40% of the time, we observe a transformation of structure 8 ( $C_{2v}$ ) to structure 3 ( $D_{2d}$ ). However, on starting from isomer 3, we never see the formation of isomer 8. In fact the  $D_{2d}$  configuration of structure 3 has a 100% return rate up to 0.17 eV/atom above the global minimum, clearly indicating the existence of a high entropic or kinetic barrier shielding structure 3 from the rest of the landscape. We note that in general (42), such entropic barriers are usually not symmetrical at a

## 4. EXPLORATION OF THE ENERGY LANDSCAPE ON $\text{MGF}_2$

---

given energy level  $TE$ , i.e.  $B_S^{(A \rightarrow B)}(TE) \neq B_S^{(B \rightarrow A)}(TE)$ .

From the analogous ab initio charts, we see that the first transition appears at a threshold of 0.132 eV/atom (threshold, ab initio, 1<sup>st</sup> transition: TA1) above the global minimum, where the basins 5 and 6 interact. On raising the threshold by 0.05 eV/atom (TA2 = 0.182 eV/atom), isomer 4 returns to isomer 1 with a probability of 92%. On raising the threshold by a further 0.05 eV/atom (TA3 = 0.232 eV/atom), we see that all runs originating from structure 8 lead to structure 3. Similarly, all runs starting from isomer 9 lead to isomer 3. We note that these three isomers all exhibit essentially linear structures. This distinct close association of isomers with linear structures is not observed so clearly for the empirical landscape.

It is clear that although the sub-basins remain the same, preferences for certain basins change when going from the empirical to the ab initio potential. For example, there was a greater probability flow from structure 6 to structure 5 in the empirical potential threshold runs when compared to the ab initio energy threshold runs. Also, minima corresponding to structures 1 and 2 are very closely associated on the ab initio landscape but not with isomer 4, while in threshold runs on the empirical landscape, structure 2 never appears without the concurrent appearance of both structures, 1 and 4.

### 4.2.5 Probability flows - $(\text{MgF}_2)_4$

A probability flow chart derived from the threshold runs for the tetramer can be seen in Figure 4.11. At the lowest threshold, only the low-energy structures (1, 2, 3 and 4) interact with each other significantly. We next see the emergence of the (14-2) and (9-7) sub-basins which do not even require a bond to be broken during the transition. As we increase the threshold by a further 0.05 eV/atom, greater energetic barriers are overcome. As in the trimer, the basin corresponding to the essentially linear configuration 21 ( $D_{2h}$ ) remains completely isolated up to the highest threshold value considered (0.27 eV/atom above the global minimum), indicating a combination of large energetic and entropic barriers that separate this isomer from the rest of the landscape.

### 4.2.6 Holding point analysis - $(\text{MgF}_2)_3$

The analysis of holding points and the minima one can reach from these configurations gives us further insight into the size of transition regions connecting the basins(21). For instance, one can visualize the various routes taken by the walkers moving between different interacting local minima at different threshold values. A holding point is qualitatively classified as either a basin point or a transition point based on the following criteria: 1) A holding point is a basin point if at least 80% of the quenches (4 out of 5) end up in the same minimum. Otherwise, the holding point is a transition point . 2) A holding point is a basin point if 100% of the quenches (5 out of 5) end up in the same minimum. Otherwise it is a transition point.

## 4.2 Detailed energy landscapes of neutral $(\text{MgF}_2)_n$ ( $n=3, 4$ ) clusters

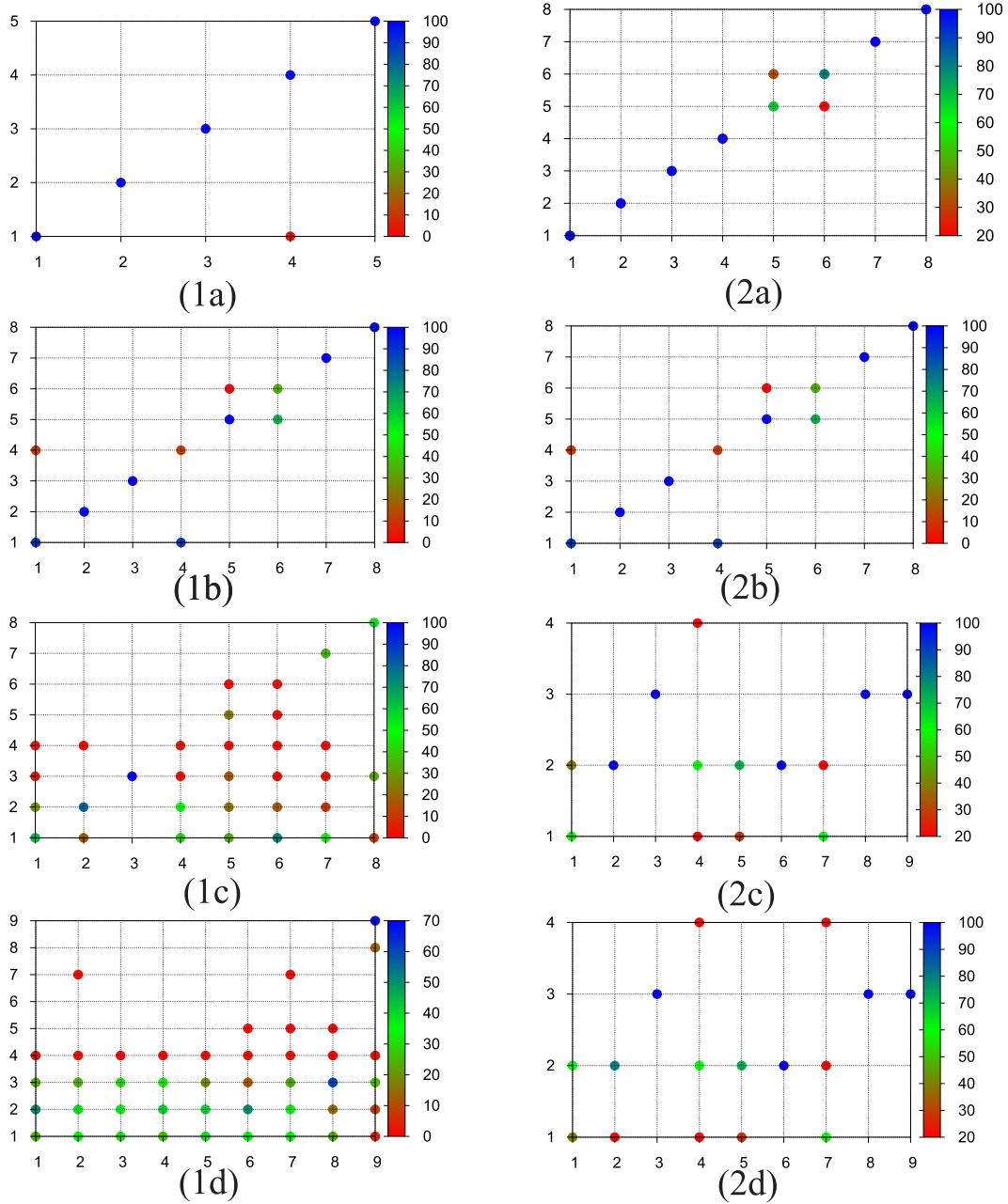
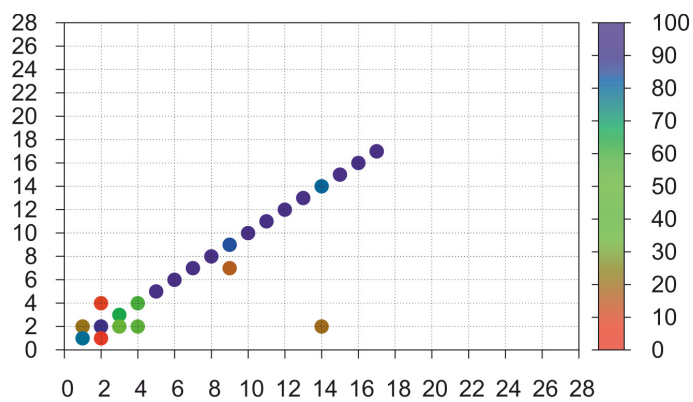
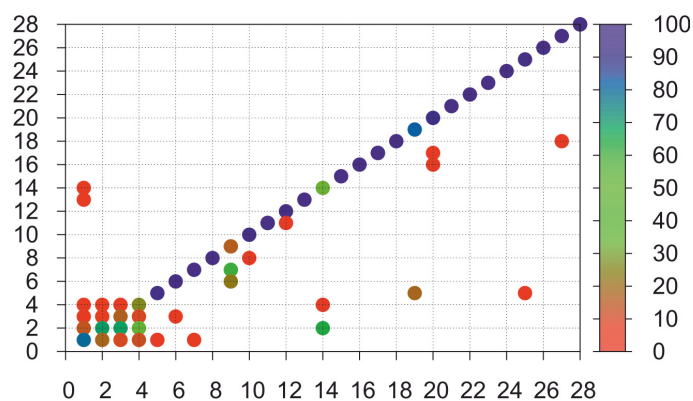


**Figure 4.7: Probability flow-chart : Trimer** - Probability flow charts derived for the trimer from threshold runs. x-axis: starting configuration (1-9); y-axis: final configuration (1-9) (1) empirical landscape at (a) 0.037 eV per atom, (b) 0.087 eV per atom, (c) 0.127 eV per atom and (d) 0.177 eV per atom above the global minimum. (2) Ab initio landscape at (a) 0.132 eV per atom, (b) 0.182 eV per atom, (c) 0.232 eV per atom and 0.282 eV per atom above the global minimum.

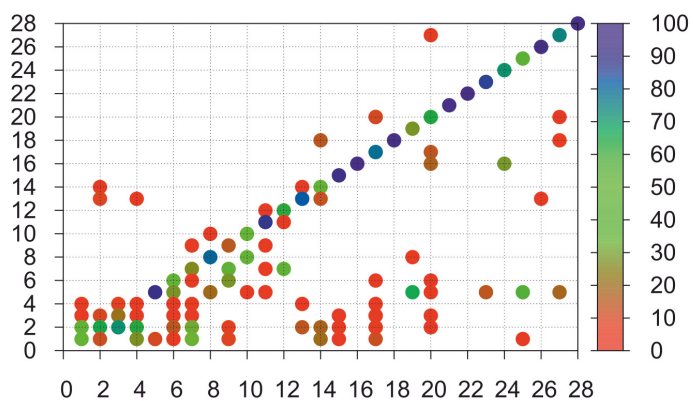
#### 4. EXPLORATION OF THE ENERGY LANDSCAPE ON $\text{MGF}_2$



(1a)



(1b)



(1c)

**Figure 4.8: Probability flow-chart : Tetramer** - Probability flow charts derived for tetramer from threshold runs. x-axis: Starting configuration (1-28); y-axis: Final Configuration (1-28). Empirical landscape at a) 0.07 eV/atom, b) 0.12 eV/atom and c) 0.15 eV/atom. above the global minimum.

## 4.2 Detailed energy landscapes of neutral $(\text{MgF}_2)_n$ ( $n=3, 4$ ) clusters

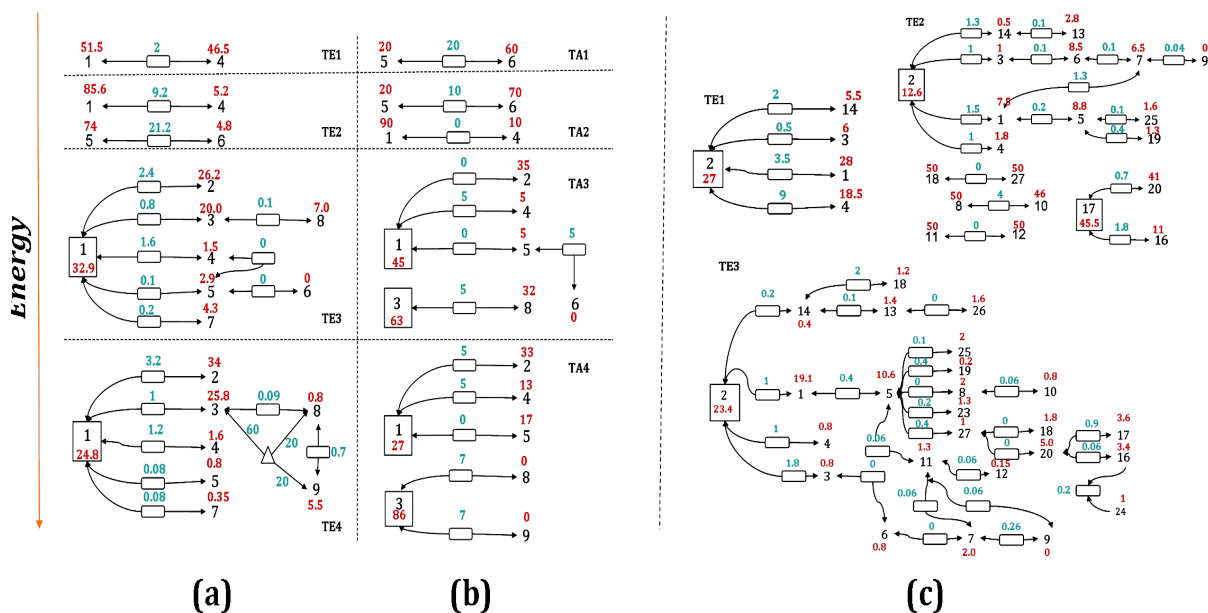


**Figure 4.9: Holding point analysis: trimer** - The figure shows all the transitions as a function of the threshold values for 1) Empirical landscape at a) 0.037 eV/atom b) 0.087 eV/atom c) 0.127 eV/atom and d) 0.177 eV/atom above the global minimum and 2) Ab initio landscape at a) 0.132 eV/atom b) 0.182 eV/atom c) 0.232 eV/atom and 0.282 eV/atom above the global minimum. Numbers in red show the percentage of holding points belonging to the basins corresponding to the local minima. Numbers in green show the percentage of holding points corresponding to the transition regions. Every isolated region is allotted a 100% probability.

In Figure 4.9(1a-1d) we have plotted the percentages of all the holding points associated with the transition regions as well as the holding points belonging to basins that correspond to individual local minima for the empirical potential landscape. We note that at low energy lids, the landscape is usually split into several disjoint regions. For every such isolated region on the energy landscape, the probabilities to belong to holding and transition points add up to 100%. For example, in Figure 4.9(2d), we see there are two distinct isolated regions on the energy landscape. One corresponds to the four minimum (1-2-4-5) basin which contains more compact structures. The other corresponds to the three minimum (3-8-9) basin which contains the linear  $D_{2d}$  structure 3 and its modifications. Only minima that interact with other minima at a given threshold are shown here. It is clear that both the aforementioned classification schemes give similar numbers in Figures 4.9(1a-1d). However, the difference is much greater in Figures 4.9(2a-2d) because only 5 holding points per structure were generated for a given threshold.

For the trimer, 2% of the holding points at the lid TE1 = 0.037 eV/atom belong

## 4. EXPLORATION OF THE ENERGY LANDSCAPE ON $\text{MgF}_2$

---

to transition regions. This changes to 30.4%, 5.2% and 4.7% on raising the threshold to  $\text{TE2} = 0.087$  eV/atom,  $\text{TE3} = 0.122$  eV/atom and  $\text{TE4} = 0.177$  eV/atom, respectively. It is interesting that in contrast to the study(21) of the landscape of solid  $\text{MgF}_2$ , the size of the transition regions does not monotonically increase with lid-energy. If this observation also applies to other cluster systems, it might have important consequences both for the synthesis of various cluster isomers and their isomerization, and the success of the many global optimization algorithms that are based on combinations of large jumps on the landscape with local optimizations.

Since we do not sample the configurational space long enough using ab initio methods, we do not have enough statistics to make a statistically significant comparison with the empirical potential threshold runs. However, for the sake of completeness, a diagram is provided in Figure 4.9(2a-2d). The most obvious difference to the empirical landscape is that the landscape remains split into disjoint regions up to much higher energies, in agreement with the energy barriers found for the two landscapes. Furthermore, the size of transition regions appears to be larger on the ab initio energy landscape than on the empirical energy landscape.

Both for the ab initio and empirical energy landscape, we see that isomer 6 is visible, i.e. it possesses basin points among the holding points, only until threshold T2 and then disappears for higher energies. This indicates that it is a small sub-basin bordering only structure 5, while the latter can draw probability from the main part of the landscape, mainly via isomer 1.

### 4.2.7 Holding point analysis - $(\text{MgF}_2)_4$

A similar analysis of holding points was performed for the tetramer as well (Figure 4.10), where the same convention was applied to the holding point assignments as for the trimer. The first minima that interact are 1, 2, 3, 4 and 14, and 15% of all holding points are transition points at the first threshold value ( $\text{T1} = 0.07$  eV/atom). On raising the threshold by 0.05 eV/atom to 0.12 eV/atom above the global minimum, 5.2% of all holding points belong to transition regions. We see five distinct isolated regions on the energy landscape with interacting local minima. The basin that originally contained only the isomers with octagonal rings (1, 2, 3, 4 and 14) now also includes clusters with high coordination and more compact structures (5, 6, 7, 9, 13, 19 and 25). The possible routes for this isomerization can be visualized using Figure 4.10. Transformations to each of these configurations can be achieved by 'breaking' only one bond in the ring-like structures followed by some atom rearrangement. The second isolated region consists of structures 16, 17 and 20. Transformations among these structures again require only one bond to be broken followed by a rearrangement. In fact, isomers 16, 17 and 20 lie so close to each other on the landscape that from four different holding points one could reach all three of these minima when performing the set of five multiple quenches. The other three isolated basins contain the interacting pairs of isomers 18-27, 8-10 and 11-12, respectively.

At the next threshold of 0.17 eV/atom above the global minimum, we see that the smaller isolated basins mentioned above merge into the biggest basin and all of the local minima (except 15, 21, 22 and 28) can interact with each other. The possible

## 4.2 Detailed energy landscapes of neutral $(\text{MgF}_2)_n$ ( $n=3, 4$ ) clusters

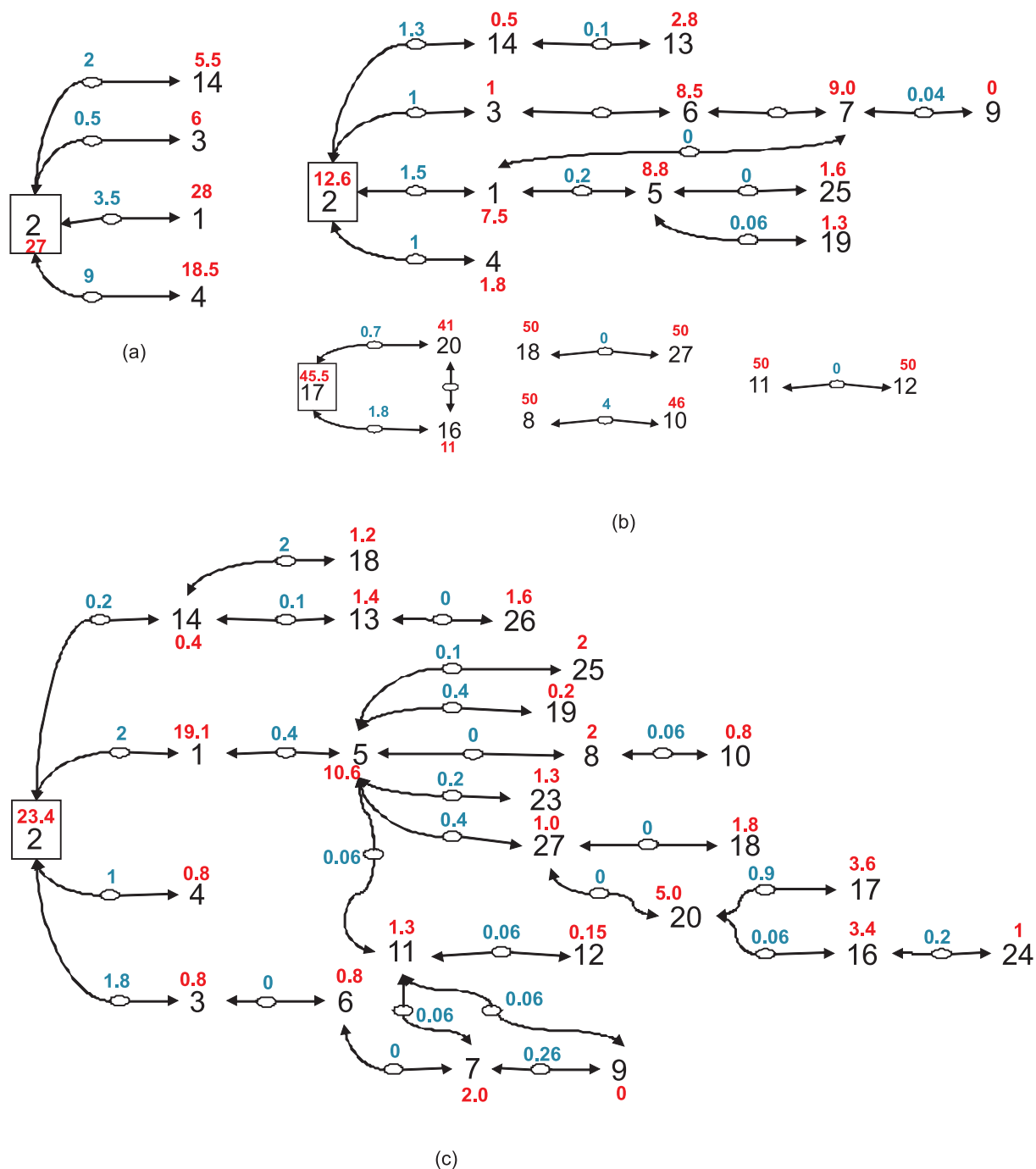


**Figure 4.10: Holding point analysis: tetramer** - All transitions as a function of the threshold values for runs with a pair potential on the tetramer at threshold values of a) 0.07 eV/atom, b) 0.12 eV/atom and c) 0.15 eV/atom. Holding point belongs to a basin if 4 out of 5 quenches lead to the same minimum.

## 4. EXPLORATION OF THE ENERGY LANDSCAPE ON $\text{MgF}_2$

---

paths are shown in Figure 4.10. From the tree-graph in Figure 4.6, structures 15, 22 and 28 start interacting with other local minima at the next threshold of 0.22 eV/atom. However, the energetic barrier for a transformation of the linear  $D_{2h}$  structure is not crossed up to the highest lid considered, 0.27 eV/atom above the global minimum.

### 4.2.8 Local density of states - $(\text{MgF}_2)_3$

Using the overlap of the densities of states (DOS) observed when starting from a given minimum  $i$  allows us to approximately construct the local density of states  $g_i(E)$ (104). These local DOS merge once the energy barrier for a transition has been reached and in addition the growth laws of the different  $g_i(E)$  have become essentially identical. Thus, it is possible that the full merger occurs at energies higher than the energy of the lowest saddle connecting the two basins. The reason for this is the fact that due to finite sampling time one actually measures the *accessible* local density of states, i.e. the sampling can be influenced by the entropic barriers that separate two basins even at energies above the saddle points. From Figure 4.11 we see that for the trimer,  $g_i(E)$  for every local minimum  $i$  fully merges with the global minimum at some energy which typically lies a little higher than the energetic transition barriers. Only at lid values above the energetic barriers (0.22 eV/atom),  $g_i(E)$  is practically independent of the starting points. On the other hand, we note that minima corresponding to isomers 6 and 8, and similarly isomers 3 and 2, follow a very similar growth law even before reaching the separation barrier energy. This indicates that the phase space volumes of these basins are rather similar already in the regions close to the respective local minima. However, these similarities were not reflected in the probability flows, indicating that the multidimensional shapes of the two basins are different nevertheless.

### 4.2.9 Comparison of ab initio and empirical landscapes

When comparing the ab initio and empirical landscapes, two clear differences emerge. Firstly, the global minima predicted are different. Secondly, the barriers predicted with the ab initio calculations are, in general, significantly higher than the ones for the empirical potential. However, both configurations suggested to be global minima belong to the structures with the lowest energies for both the empirical and the ab initio landscape. Furthermore, the barrier trends for transition to the respective global minima remain the same. Still, it is clear from the different global minima and the barriers for the 6-5 transition that the empirical energy function does not properly work for structures with low coordination. It could therefore be beneficial if the pair-potential parameters were (re-)fitted with these energetic barriers in mind. Regarding the dynamics on the energy landscape, features such as sub-basins, transition regions, and overall probability flows are quite similar for the two landscapes. Quite generally, such a comparison of the dynamics can serve as an indicator of how much of a system's "real" landscape is reproduced by a given force-field, in contrast to just selected (minimum) configurations. Thus, comparing both the minima and the dynamics of



## 4.2 Detailed energy landscapes of neutral $(\text{MgF}_2)_n$ ( $n=3, 4$ ) clusters

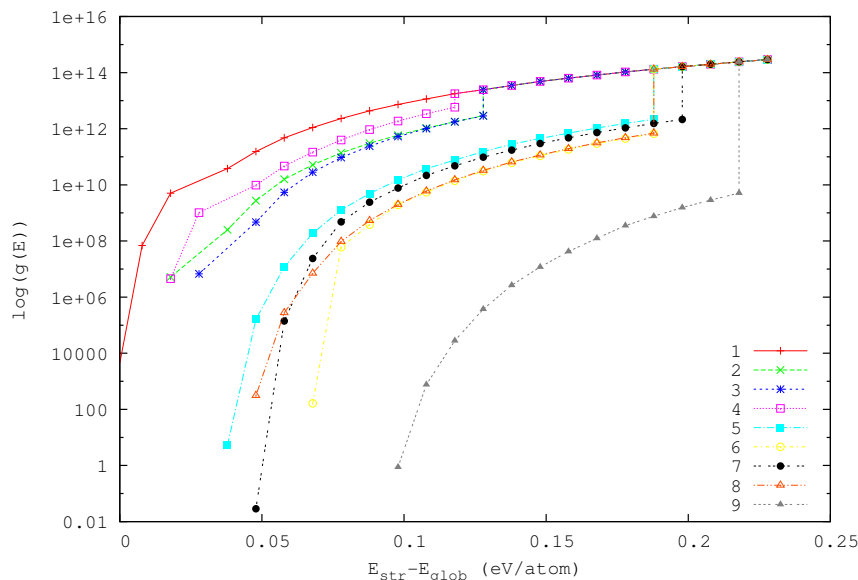


**Figure 4.11:** Local densities of states  $\log(g(E))$  for all neutral trimer structures, based on sampling the empirical potential landscape. The red line corresponds to the global minimum.

landscapes based on ab initio calculations and empirical potentials is expected to become a valuable tool for validating empirical potentials in the future.

Of possibly general importance could be the observations, if confirmed, that a) the ratio of the size of transition and basin regions does not remain constant with energy, and b) the relative size of the transition regions is larger for the ab initio landscape than for the empirical potential one. Experimentally, the small size of the transition regions suggests that a) the various isomers can exhibit some degree of stability even at relatively high temperatures compared to the lowest saddle barrier energies, and b) the transformations between isomers occur only via a few distinct channels on the landscape. Concerning the global search for minima, the existence of many basin points at high energies might explain the success of algorithms that combine large jumps on the landscape with local minimizations, such as basin-hopping(79), thermal cycling(129, 130) or evolutionary algorithms(131), at least for small clusters. However, it is clearly necessary that many more (cluster) landscapes need to be explored regarding the size of their characteristic regions, before firm conclusions can be drawn.

### 4.2.10 Thermodynamics

Returning to the original motivation for the exploration of the landscape of  $\text{MgF}_2$  clusters, an important aspect for the proper modeling of the gas phase of  $\text{MgF}_2$  during

## 4. EXPLORATION OF THE ENERGY LANDSCAPE ON $\text{MgF}_2$

---

the LT-ABD synthesis is, to what extent the clusters in the gas phase are equilibrated among each other (via collisions), and with respect to the isomerization processes of an isolated cluster. Thus, as a first step, we have computed the Boltzmann-equilibrium probabilities of an isolated trimer and tetramer cluster as a function of temperature based on the energies of the individual minima (c.f. Figure 4.12(a) and 4.12(b), respectively).

Francisco et al. have previously computed the Boltzmann distributions of three specific trimers (structures 1, 2 and 3) using total energies (derived via Møller-Plesset perturbation methods that are expected to yield somewhat more accurate energies than the ones we have computed here) and including harmonic vibrational frequencies(48). They observe a transition from isomer 3 ( $D_{2d}$ ) to isomer 2 ( $D_{3h}$ ) at 3600 K which is due to the different vibrational contributions of these structures. We do not observe any such transitions, of course, since we compute the Boltzmann distribution based only on the energies of the minima. However, this is not critical, since we are only interested in the low-temperature regime expected to exist in the experiment, where the vibrational contributions are not very influential.

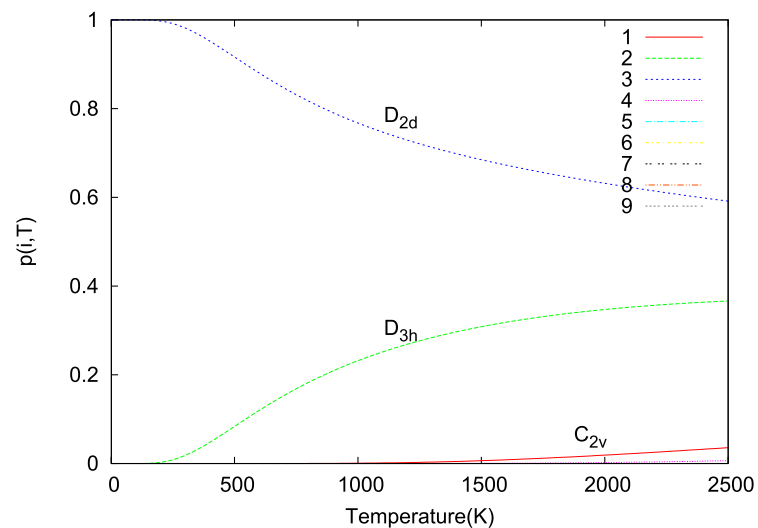
The next step is the computation of the likelihood of collisions among the clusters during their travel between the source and target. Using the kinetic theory of gases (132), we find that for an ideal trimer gas, the root mean square velocity ( $\sqrt{\frac{3RT}{M}}$ ) is 200.09 m/s for the trimer and 173.28 m/s for the tetramer respectively, and thus, the mean free path in the framework of the LT-ABD synthesis (18) of bulk  $\text{MgF}_2$ , where typically low pressures ( $10^{-4}$  mbar) and temperatures (280K) are involved<sup>1</sup>, for the trimer (approximately 5 Å in diameter) is 71.2 cm and for the tetramer (approximately 10 Å in diameter) is 17.8 cm. Thus, the molecules should not collide with each other once they have left the surface of the source material. Since the distance from source to target is approximately 15 cm in the experimental apparatus, internal degrees of freedom must be used for isomerization transitions between the different minima.

The ab initio barriers, and the analysis of the holding points, probability flows and local DOS indicate that once a certain cluster configuration is achieved, it takes a relatively high temperature (of the order  $10^3\text{K}$ ) for any fast isomerization reaction. Combining this with our observation during the simulated annealing runs that isomer 3 ( $D_{2d}$ ) is by far the most likely one to form in the vapor phase (for short synthesis times) when starting from single atoms or molecules that merge to form trimers, suggests that there is a good chance that isomer 3 would be observed, besides the other minima with the lowest energies (1 and 2). Clearly, analogous arguments apply to the

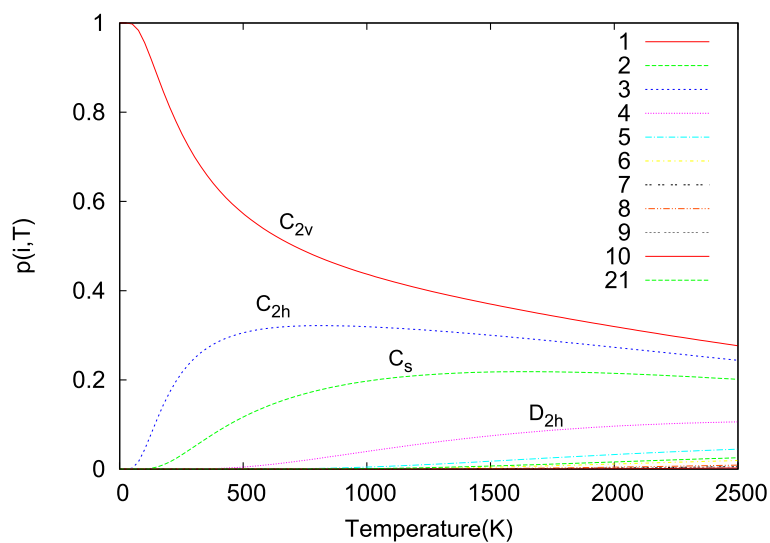
---

<sup>1</sup>Based on the ratio of vaporization temperature  $T_V \approx 2500$  K to the temperature to which the source material is heated  $\approx 1500$  K,  $T_V/T_S \approx 5/3$ , one finds that the evaporated gas of clusters (consisting of the high-velocity tail range in the Maxwell-Boltzmann distribution of the atoms at the surface of the source material) should have a temperature of  $T_c \approx 280$  K after escaping from the solid surface. This estimate assumes that the evaporated clusters do not reach equilibrium with the heated surface of the source material, but travel essentially ballistically towards the target (and the cooled walls of the synthesis chamber).

## 4.2 Detailed energy landscapes of neutral $(\text{MgF}_2)_n$ ( $n=3, 4$ ) clusters



( a )



( b )

**Figure 4.12:** Boltzmann distribution curves based on the fully optimized ab initio energies of local minima for the trimer (a) and tetramer (b). For the tetramer, only the ten lowest minima and structure 21 are depicted.

## 4. EXPLORATION OF THE ENERGY LANDSCAPE ON $\text{MgF}_2$

---

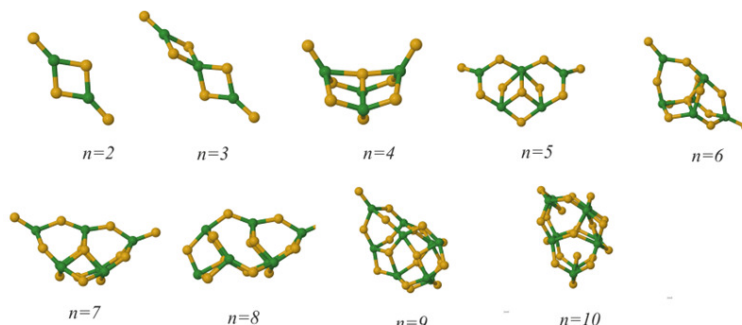


**Figure 4.13: Global minima** - Global minimum for  $(\text{MgF}_2)_{1-10}$  clusters from Monte-Carlo simulated annealing.

tetramer, where also the  $D_{2h}$ -isomer 21 is expected to be present besides the low-energy structures 1, 2, 3 and 4 (c.f. Figure 4.12(b))

Furthermore, the common occurrence of fragments in the optimization runs suggests, that many individual  $\text{MgF}_2$  molecules and  $(\text{MgF}_2)_2$  clusters will also be present in the gas phase, besides the trimers and tetramers, and should be included in the gas mix impinging on the substrate.

### 4.3 Global optimizations of neutral $(\text{MgF}_2)_n$ clusters

The global minima of neutral clusters containing up to 10 units of  $\text{MgF}_2$  are depicted in Figure 4.13 and the simulated annealing runs are summarized in Table 4.3. Our global minima for  $(\text{MgF}_2)_{2-10}$  are in good agreement with those found in a previous study on the same system which employed a basin-hopping scheme for finding global minima (133). The bond energies and second energy differences indicate that in thermodynamic equilibrium, clusters of sizes 2, 7 and 8 would be favored.

### 4.4 Global optimizations of charged clusters

To our knowledge, the structures of charged species of Mg/F clusters have not been studied. Since we cannot exclude the possibility of their survival under experimental conditions, we have also investigated the energy landscapes of such charged structures and determined the deepest local minima via the stochastic simulated annealing algorithm. Only structures with a single overall charge were considered. This is reasonable as it would take an unrealistic amount of energy to form small divalent charged clusters in the vapor phase. The systems studied were  $\text{MgF}^+$  (monomer cation),  $\text{MgF}_3^-$

## 4.4 Global optimizations of charged clusters

**Table 4.3:** Global optimizations for  $(\text{MgF}_2)_{2-10}$ .

Number of units	Number of minima after MC/SA	Energy per $\text{MgF}_2$ unit(eV)	Point group
2	1	-399.84708	$D_{2h}$
3	6	-399.86548	$D_{2d}$
4	18	-399.87922	$C_{2v}$
5	34	-399.88607	$C_s$
6	71	-399.89275	$C_s$
7	117	-399.90171	$C_{2v}$
8	151	-399.90564	$C_s$
9	169	-399.90602	1
10	181	-399.91225	$C_s$

(monomer anion),  $\text{Mg}_2\text{F}_3^+$  (dimer cation),  $\text{Mg}_2\text{F}_5^-$  (dimer anion),  $\text{Mg}_3\text{F}_5^+$  (trimer cation) and  $\text{Mg}_3\text{F}_7^-$  (trimer anion). The local minima obtained for each of these systems are depicted in Figure 4.14. Again, the structures are labeled in the order of the energies obtained from the pair-potential. The parameters for simulated annealing used for these clusters are exactly the same as the ones used for the neutral clusters.

We used a Monte-Carlo simulated annealing based approach to find the global minima for all neutral and charged clusters up to decamers and trimers ( $(\text{Mg}_3\text{F}_7)^-$ ,  $(\text{Mg}_3\text{F}_5)^+$ ), respectively. The starting point was a random atom arrangement inside a very large cubic simulation cell. The initial volume of the container was 100 times the volume of the atoms/ions as estimated by their atomic radii. We used periodic boundary conditions as far as the movement of atoms was concerned, but atoms could only interact inside the simulation box. The atoms were not allowed to come closer than 0.55 Å. All calculations were performed at 0 GPa. The form of the two-body potential used and the parameters for the optimization(112) were exactly the same ones used for optimizing neutral clusters discussed above.

For each of the polymers of  $\text{MgF}_2$  considered, one very long simulated annealing run consisting of  $10^6$  Monte-Carlo steps was performed, in order to find the global minimum and as many low-lying side minima as possible. The temperature was reduced exponentially from 1 eV/atom to 0.006 eV/atom over the length of the annealing run. At 400 different points along the trajectory, we performed 5 quenches of 10,000 steps each followed by a gradient descent after each quench. Afterwards, the five structures with the lowest energies and/or largest basins were picked and optimized at the ab initio level. Finally, the vibrational spectra were calculated for the modification with the lowest ab initio energy.

As far as the periodic systems were concerned, no further global explorations were performed. The most promising candidates suggested by Wevers et al.(41) were analyzed on the ab initio level by minimizing their energies and computing their Raman

## 4. EXPLORATION OF THE ENERGY LANDSCAPE ON $\text{MgF}_2$

---

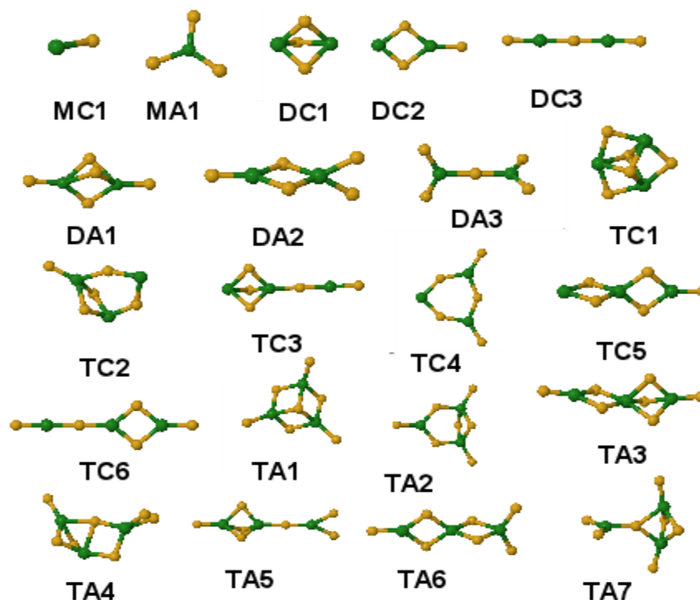


**Figure 4.14: Isomers of monovalent clusters** - Isomers of all the monovalent clusters studied. MA=Monomer Anion, DA=Dimer Anion, TA = Trimer Anion, MC = Monomer Cation, DC = Dimer Cation, TC = Trimer Cation

and infra-red spectra.

### 4.4.1 Conclusion

We have explored the energy landscape of  $\text{MgF}_2$ -trimers and  $\text{MgF}_2$ -tetramers both on ab initio and empirical potential level, and determined not only the stable isomers, but also the energetic and entropic barriers separating them and their local densities of state. Especially for the tetramer, we observe that the energies are systematically different for the less compact clusters, when comparing empirical and ab initio energies. To our knowledge, this is the first study comparing energetic barriers of empirical and ab initio potentials. The agreement is better for the more compact clusters, which is to be expected, as the potential was calibrated for bulk  $\text{MgF}_2$  and thus a compact structure. We find that the barrier structures of the empirical and ab initio energy landscapes are quite similar qualitatively although quantitative differences exist. We have investigated the probability flow on the landscape, in order to study the stability of the various isomers. We find that with the mean free path greatly exceeding the distance between source and substrate in the experiment, the stability of the individual local minima is high enough such that a mixture of different isomers is expected to impinge on the substrate during the LT-ABD synthesis of metastable  $\text{MgF}_2$ -modifications.

## 4.4 Global optimizations of charged clusters

---

Additionally, we have also found local minima from extensive simulated annealing runs for possible species of charged clusters and global minima for clusters upto  $(\text{MgF}_2)_{1-10}$ . We now proceed to calculate at ab initio level, the Raman and IR spectra of all the species found from these extensive studies in the next chapter.

#### 4. EXPLORATION OF THE ENERGY LANDSCAPE ON $MGF_2$

---



## Part V

# Ab initio Raman and IR spectroscopy



# 5

## Ab initio Raman and IR spectroscopy

Experimental studies including Raman (37), IR (38), and mass spectroscopy measurements (39, 40) have been performed in the past on  $\text{MgF}_2$  clusters. The frequencies of the monomer, two dimers and nine proposed trimers of  $\text{MgF}_2$  have been studied at different levels of theory (46, 47, 48, 48, 49, 50) already. For example,  $(\text{MgF}_2)_2$  clusters have been previously observed and characterized using Raman spectroscopy(37). But up to now, none of the theoretical calculations have included any data on intensities, which would be particularly useful when assigning structures from experimental data. Furthermore, the possible charged species of  $\text{MgF}_2$  that could appear when generating the gas phase in the experimental LT-ABD setup have not been studied yet. In this chapter, we present the results of computations of the Raman and IR frequencies and intensities of all species found in the previous chapter.

### 5.1 Methodology

#### 5.1.1 Theory

##### 5.1.1.1 Local optimization and determination of IR/Raman frequencies

The energy landscape including the barrier structures and probability flows among the local minima, has been described in detail in the previous chapter for the neutral trimer on the ab initio level (DFT with a B3LYP functional), and for the neutral tetramer on the empirical level using a standard Coulomb-plus-Buckingham type potential. Estimating the lifetimes of the various cluster modifications, we found that many isomers of  $\text{MgF}_2$  clusters may survive in non-negligible amounts in the vapor phase, even at high temperatures during a low-temperature atom beam deposition experiment. Thus, while the smaller  $(\text{MgF}_2)_{1-3}$  clusters are the ones most likely present in the gas phase

## 5. AB INITIO RAMAN AND IR SPECTROSCOPY

---

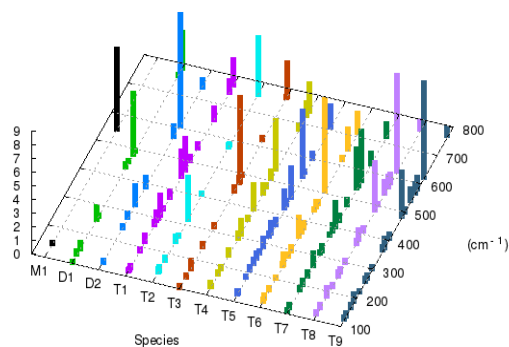


**Figure 5.1:** Raman frequencies and intensities for neutral clusters (up to three  $\text{MgF}_2$  units) calculated in the B3LYP/631++G\*\* basis. The nine isomers are labeled in increasing order of energies derived from the pair-potential as discussed in the previous chapter.

in an evaporation-based experiment, it is likely that higher oligomers and even charged Mg/F clusters may be present in the gas phase or on the surface as part of the deposit. Similarly, possible bulk polymorphs of  $\text{MgF}_2$  were calculated by Wevers et al. (21, 41) in an earlier study. In the previous section, these crystalline modifications were locally optimized. After careful optimization, we calculated the Raman and IR active frequencies, in detail for each polymorph using CRYSTAL'09. It must be noted that these frequencies are very sensitive to the positions of the atoms. Thus, extremely tight parameters were used during optimization and all structures were re-optimized until convergence was achieved after the first step itself.

We used the Gaussian03 (134) software for optimization and calculation of the Raman spectra and vibrational modes of charged and neutral  $\text{MgF}_2$  clusters. All calculations were performed with the B3LYP functional (120) in the 6-311++G\*\* basis. The energies, bond-lengths and frequencies for the trimer were then compared with known values from the literature.(37, 38, 47, 48, 49, 135).

Raman spectra for solid  $\text{MgF}_2$  were calculated using CRYSTAL09 (100, 115). For magnesium, the basis sets from Valenzano et al. (116) and for fluorine the basis sets from Nada et al. (117) were chosen, respectively. We verified that the lattice constants of the rutile-type modification of bulk  $\text{MgF}_2$  were well reproduced. Similarly, we compared the energies, bond lengths and frequencies with experimental measurements from Porto et al (36). In these calculations, the infra-red intensity and Raman activity of the vibrational modes are determined from the changes in the electric dipole moment and the polarizability tensor with the oscillations of the atoms.

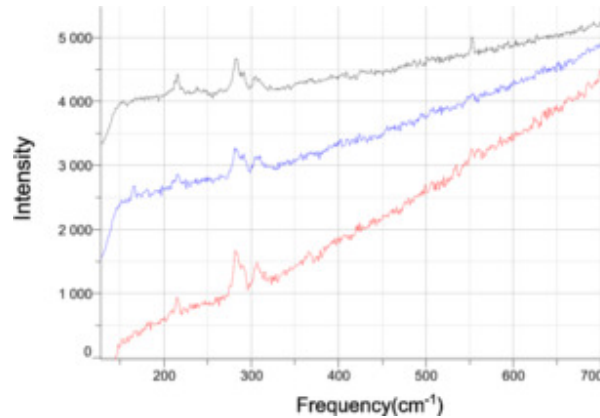


**Figure 5.2:** Experimental Raman spectra of three different samples of  $\text{MgF}_2$  in argon matrix (deposited at  $-250^\circ\text{C}$  (LHe), sapphire substrate,  $1 \times 10^{-4}$  mbar Ar-chamber pressure) measured at  $-250^\circ\text{C}$ . Experimental Raman measurements by A. Bach (18).

### 5.1.2 Experiment

In order to be able to identify the clusters actually present in the gas phase during the LT-ABD synthesis, magnesium difluoride films and samples of  $\text{MgF}_2$  in argon matrices were prepared by A. Bach and D. Fischer (136) to perform studies by Raman spectroscopy. Magnesium difluoride (99.99%, Aldrich, USA) was dried at  $200^\circ\text{C}$  in vacuum and directly evaporated from an effusion cell (Dr. Eberl MBE - Komponenten GmbH, Germany), which was held at a constant temperature between  $1020^\circ\text{C}$  and  $1050^\circ\text{C}$ , and deposited onto a cooled substrate ( $-100^\circ\text{C}$ ) inside an ultra high vacuum chamber ( $1 \times 10^{-8}$  to  $5 \times 10^{-9}$  mbar) for a period of several hours. The residual gas was analyzed and monitored by quadrupole mass spectrometer (Prisma Plus QMG 220, Pfeiffer Vacuum GmbH, Germany).  $\text{MgF}_2$  in argon matrices were prepared by simultaneous deposition of  $\text{MgF}_2$  and argon gas ( $1 \times 10^{-4}$  mbar) on the cooled substrate (at  $-250^\circ\text{C}$ ). The following materials were used as substrates: sapphire (0001) (CrysTec GmbH, Germany), polished copper (polycrystalline, Goodfellow GmbH, Germany). The substrates with the deposited samples were transferred from the deposition chamber to the Raman spectroscopy unit, while maintaining vacuum and cooling, by means of a car transfer system. This work was performed by Andreas Bach and Dieter Fischer in our group. The results are summarized in Table 5.1. The experimental Raman measurement on the thin-films of  $\text{MgF}_2$  are shown in Figure 5.3 and three independent measurements on the vapor phase are shown in Figure 5.2

To carry out the Raman spectroscopy, a microscope laser Raman spectrometer (iHR 550 spectrometer; BXFM microscope, manufactured by HORIBA, Bensheim) with confocal geometry was used. The incident laser beam (473 nm at 20 mW) passes through a window in the vacuum chamber and finally impinges on the sample.

## 5. AB INITIO RAMAN AND IR SPECTROSCOPY

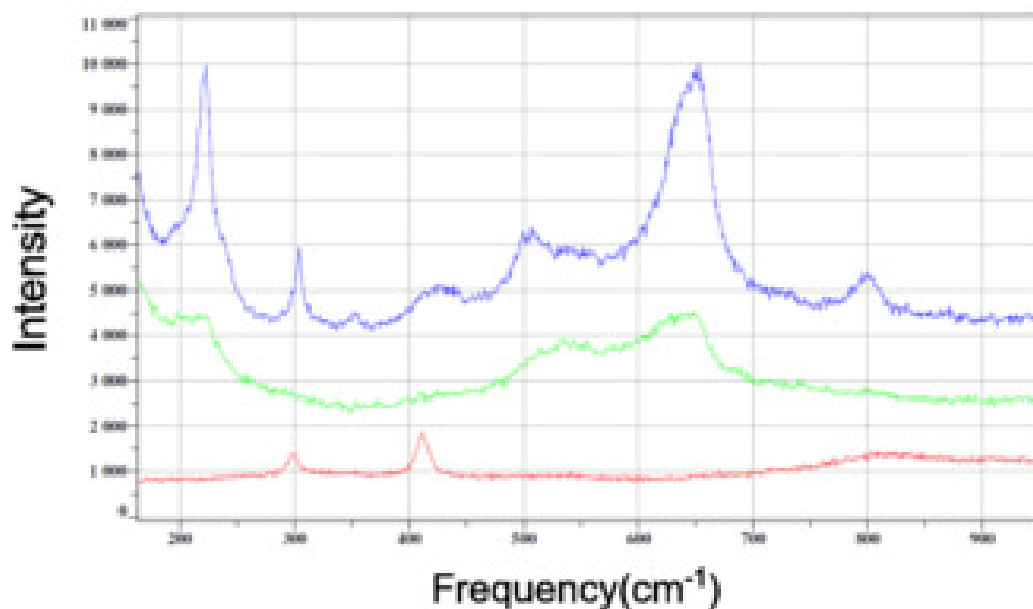


**Figure 5.3:** Experimental Raman spectra measured at 25 °C of Bottom: MgF<sub>2</sub> powder, Middle: clean Cu substrate and Top: MgF<sub>2</sub> layer on Cu substrate (deposited at -100°C). Experimental Raman measurements by A. Bach (18).

**Table 5.1:** Raman bands of MgF<sub>2</sub> clusters and bulk MgF<sub>2</sub> polymorphs.

Sample	Raman Shift(cm <sup>-1</sup> )								
MgF <sub>2</sub> in Ar-Matrix	165	216	283	291	307	365		553	
Disordered MgF <sub>2</sub> on Cu		222			303	352	419	507	800
MgF <sub>2</sub> rutile	92 <sup>1</sup>				295		410	515 <sup>1</sup>	
MgF <sub>2</sub> anatase (calculated)	160	280	322	377	451			532	
MgF <sub>2</sub> CaCl <sub>2</sub> (calculated)	153	268	277	347	384			488	

<sup>1</sup>See Ref.(36)

## 5.2 Raman and IR calculations for neutral $(\text{MgF}_2)_{1-10}$ clusters

Since our goal is to identify possible isomers in the gas-phase during an LT-ABD experiment, we have calculated Raman and IR active frequencies and intensities for all suggested modifications up to  $(\text{MgF}_2)_3$ . These include one monomer (M1), two isomers of the dimer (D1, D2) and 9 isomers of the trimer (T1-T9). The structures are labeled in increasing order of energy as computed with the pair potential. The structures of these isomers have been reported in previous works that employed Monte-Carlo investigations on the energy landscape (48, 137). In addition, we have calculated vibrational spectra for all the global minima up to  $(\text{MgF}_2)_{10}$ , since such clusters might also be present in the gas phase or form on the substrate and the vibrational spectra of these bigger clusters could help us to better understand the seeding and growth mechanisms involved in the LT-ABD met

For the monomer, the computed bond-length of 1.765 Å is in good agreement with the experimentally reported bond length of 1.77 Å (138). The F-Mg-F bending mode is found at  $145 \text{ cm}^{-1}$  in reasonable agreement with the experimentally reported value (139) of  $160 \pm 3 \text{ cm}^{-1}$ , and the Raman active symmetric stretch mode was found at  $549 \text{ cm}^{-1}$ , which is in excellent agreement with measured  $550 \text{ cm}^{-1}$  of  $\text{MgF}_2$  in an Ar matrix (37).

## 5.3 Charged Clusters

In the literature, no structures of charged species of Mg/F clusters are available. Since we cannot exclude the possibility of their survival under experimental conditions, we have also investigated the energy landscapes of such charged structures in the previous chapter. The Raman spectra computed at ab initio level for selected structures in each system are shown in Figure 5.4. All calculated Raman active modes are depicted in Figure 5.4. DA1, TC1, TC2, TC3, TC6 and TA3 show intense Raman modes. Specifically, DA1 and TC6 have intense modes at  $307 \text{ cm}^{-1}$  and  $210 \text{ cm}^{-1}$ , and TC1 a weaker one at  $150 \text{ cm}^{-1}$ . (See the appendix for more details and IR spectra)

## 5.4 Assignment of predicted vapor phase structures to experimental observations

In Table 5.2, we have summarized experimentally observed frequencies of vapor phase clusters from Lesiecki et al. (37) (L), Snelson et al (38). (S), Mann et al (135). (M) and Hauge et al (H) (140), the most recent assignments made by Francisco et al.(48) (F), along with possible assignments from this work. None of the earlier calculations on phonon modes of  $\text{MgF}_2$  clusters so far had included intensities derived for the Raman or infra-red peaks. With our new calculated data, it is possible to distinguish between

## 5. AB INITIO RAMAN AND IR SPECTROSCOPY

---

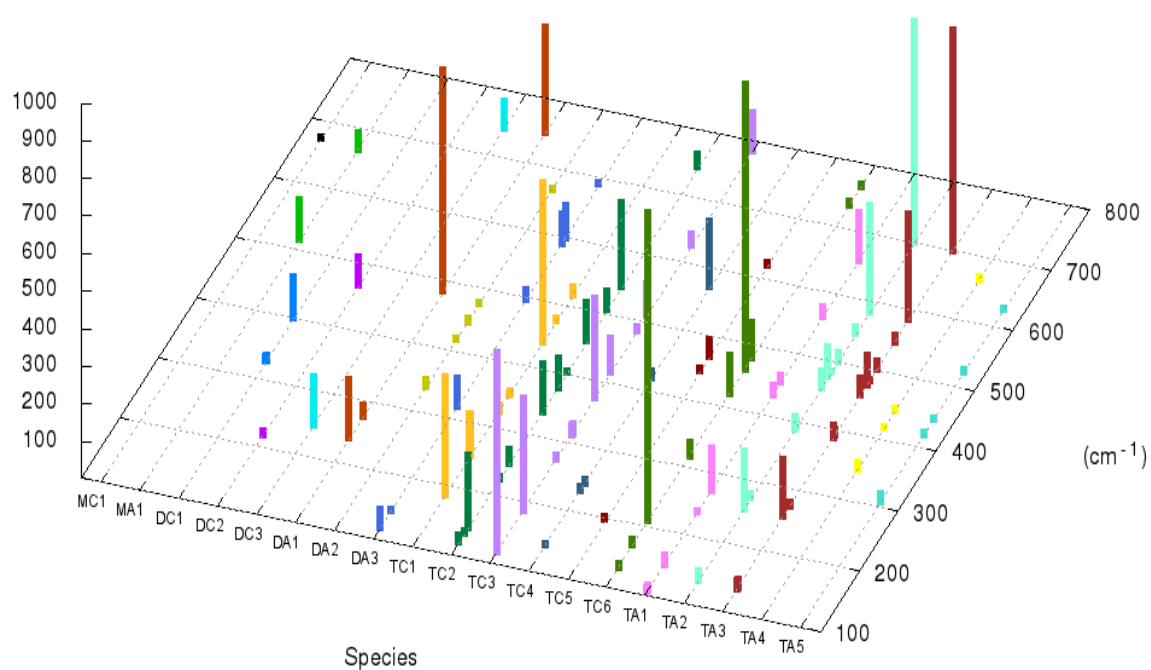


**Figure 5.4:** Raman frequencies and intensities for charged clusters upto 3 units calculated in the B3LYP/631++G\*\* basis. For notation, see previous chapter.



## 5.4 Assignment of predicted vapor phase structures to experimental observations

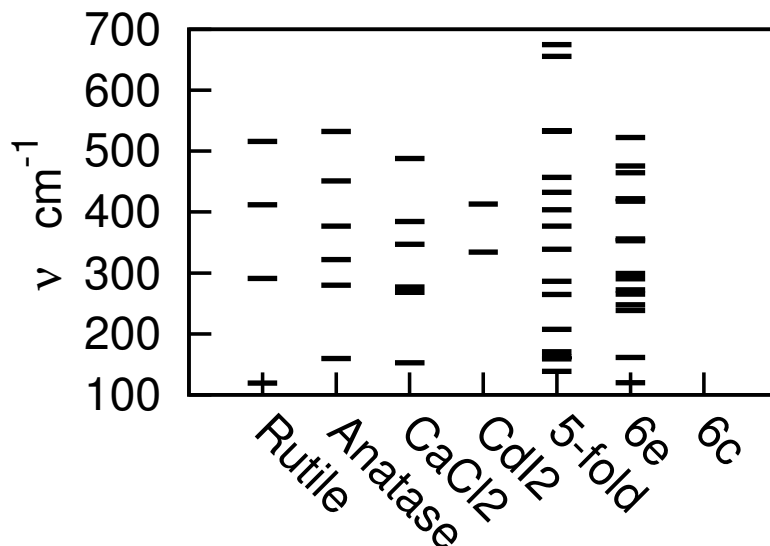


**Figure 5.5:** Raman active frequencies for possible (meta)stable modifications of bulk  $\text{MgF}_2$ .

isomers of dimers and trimers. For example, the IR active band at  $240\text{ cm}^{-1}$  had been assigned to either a dimeric or trimeric species by (M) and (F). We see that the most intense peak in this region arises from the dimer D1 ( $D_{2h}$  isomer). In the calculated IR spectrum for D1, this peak is accompanied by two other intense peaks at  $492\text{ cm}^{-1}$  and  $761\text{ cm}^{-1}$ . A peak around  $490\text{ cm}^{-1}$  was reported by S, M, H and L and assigned to a dimeric species. S and H also reported a peak at  $745\text{ cm}^{-1}$  and  $746.5\text{ cm}^{-1}$  respectively and assigned it to a dimeric species. We believe this corresponds to the intense peak found at  $761\text{ cm}^{-1}$  in our calculations for D1, which is within the error limits. Therefore, it would appear that the  $D_{2h}$  isomer of the dimer was present in the experiments reported, as the three most intense IR peaks have all been observed experimentally. The most intense Raman peak for this isomer is seen at  $480\text{ cm}^{-1}$  in our calculations. This has, however, not been reported so far, possibly due to the intensity not being measurable. L has reported Raman active modes at  $550\text{ cm}^{-1}$  and  $584\text{ cm}^{-1}$ . It is clear that the  $550\text{ cm}^{-1}$  peak comes from the most intense Raman frequency of the monomer found at  $549\text{ cm}^{-1}$  in our calculations. The mode at  $584\text{ cm}^{-1}$  was assigned to a dimeric species by L and F. The most intense Raman mode for the  $C_{3v}$  isomer of the dimer (D2) is found at  $605\text{ cm}^{-1}$  in our calculations suggesting that this is the isomer found by L. It is interesting that the most intense Raman active peak for D1 is not found in any experiment whereas all three intense IR peaks are observed.

We can say with some confidence that for our experimental results in the vapor phase the peak at  $550\text{ cm}^{-1}$  corresponds to the monomer (M1) and the one at  $365\text{ cm}^{-1}$  to the  $D_{2h}$  dimer. Among the neutral clusters considered, none of the systems had a high intensity Raman active mode up to the  $280\text{-}300\text{ cm}^{-1}$  region. Furthermore,

## 5. AB INITIO RAMAN AND IR SPECTROSCOPY

---

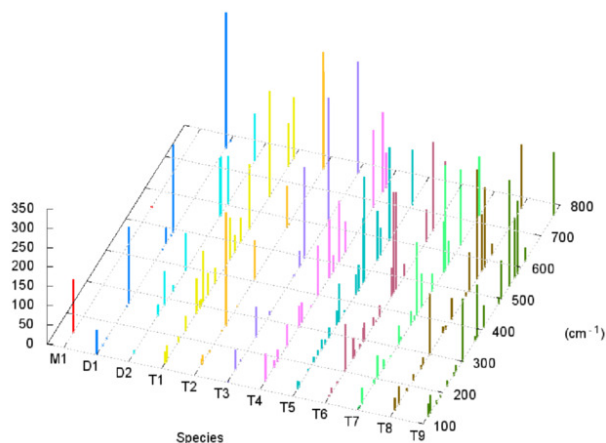


**Figure 5.6:** IR active frequencies and intensities for clusters  $(\text{MgF}_2)_n$  ( $n=1,2,3$ ).

according to the calculations, none of the other peaks were observed in previous experiments on the vapor phase of  $\text{MgF}_2$ . However, it is possible that at lower effusion cell temperatures ( $1050^\circ\text{C}$  compared to the  $1275^\circ\text{C}$  (37)), charged species are stabilized in the argon matrix. Although a number of peak assignments to various cationic and anionic clusters are possible, among the charged species considered in our calculations, DA1 appears to have a very strong Raman activity in this region of the spectrum. Thus, the dimeric anion DA1 is also likely to be present in the experiment, while the other anionic and cationic species are possible (especially DA3 and TC6) but less likely.

## 5.5 Specific structural features

### 5.5.1 Fingerprint frequencies

From the calculations performed so far, it appears that linear isomers  $((\text{MgF}_2)_{1-6})$  corresponding to  $(\text{BeCl}_2)_n$ -like chains can be identified using Raman spectroscopy. These  $\text{MgF}_2$  chains have characteristically intense frequencies at  $470\text{-}480\text{ cm}^{-1}$  and  $775\text{-}785\text{ cm}^{-1}$  with very few low-intensity Raman active modes in between (See Fig.5.8). These two modes are found as the most intense vibrations for only these types of isomers. The  $470\text{-}480\text{ cm}^{-1}$  peak is the result of in-plane stretching of the bonds involving bridging fluorine atoms that belong to the three-coordinated magnesium atoms at either end of the chain, while the  $775\text{-}785\text{ cm}^{-1}$  vibration is a result of the movement of the dangling fluorine atom at each end. These modes can be seen in Figure 5.8. In fact, this frequency appears to be characteristic for dangling F-atoms in the terminal  $\text{MgF}_3$  unit in all neutral clusters investigated.

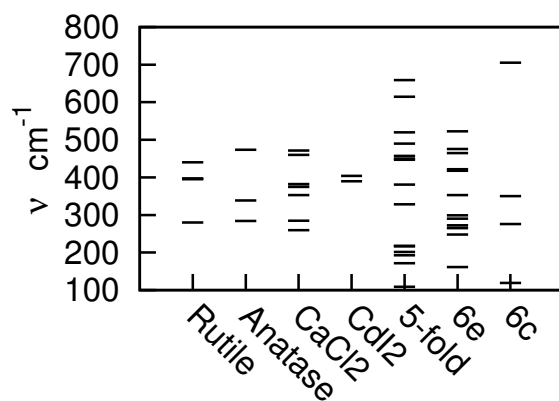


**Figure 5.7:** IR active frequencies for possible (meta)stable modifications of bulk  $\text{MgF}_2$  (Intensities for each structure are shown in the appendix).

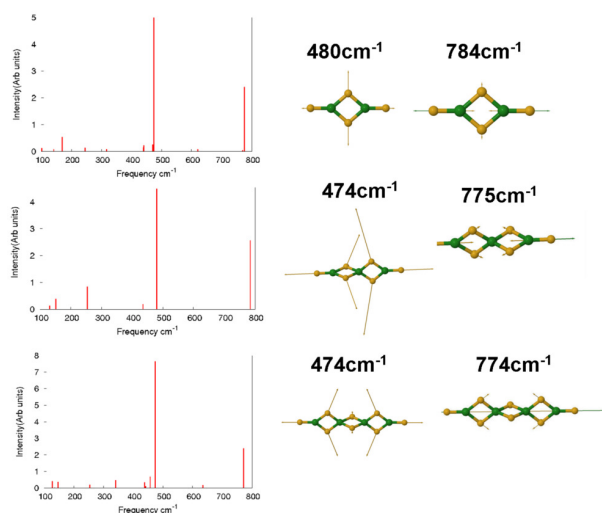


**Figure 5.8:** The two most intense modes for linear chains of the dimer(top), trimer(middle) and tetramer(bottom) of  $\text{MgF}_2$ .

## 5. AB INITIO RAMAN AND IR SPECTROSCOPY

---

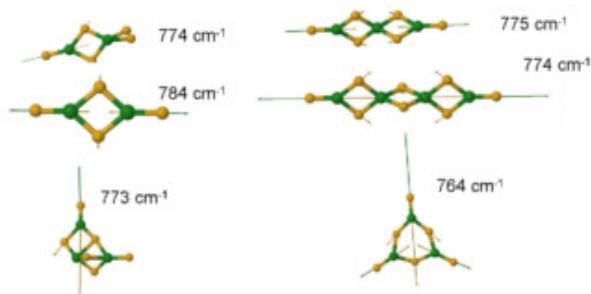


**Figure 5.9:** Examples of the Raman active frequencies possibly characteristic of the amorphous MgF<sub>2</sub> deposit containing dangling bonds.

### 5.5.2 Order parameter for amorphous-crystalline transition

In this context, we note that in the Raman measurements on amorphous MgF<sub>2</sub> deposited on Cu substrate, there occurs a broad peak at roughly 800 cm<sup>-1</sup>. However, this peak is not present in the crystalline phases. We believe this feature could be a result of dangling fluorine atoms that are only present in the amorphous material but not in the crystalline phases. In Figure 5.9, we show some examples of these modes. The arrows indicate the direction of movement of the atom. In all of the cases shown in the figure, the dangling fluorine atom on a three-coordinated Mg moves in the direction of this Mg atom and this mode always results in an intense Raman vibration between 750 and 800 cm<sup>-1</sup>. It might therefore be possible to follow the transition from amorphous to crystalline MgF<sub>2</sub> by observing this peak.

## 5.6 Limitations

### 5.6.1 Computational limitations

The most important limitation for the Raman and IR study of MgF<sub>2</sub> clusters was the non-availability of Raman intensities for bulk structures in CRYSTAL'09. While the frequencies show good agreement with the known experimental data for the rutile-type structure, it would be extremely useful to have data on intensities in order to make accurate assignments to bulk polymorphs. Also, we would have preferred to use more accurate quantum chemical methods (such as the coupled-cluster approximation and possibly multi-reference methods) for calculating the vibrational spectra. These methods are, however, much more expensive and thus too time consuming. Finally, we have used an empirical pair-potential that was fitted for reproducing the lattice parameters and elastic constants of the rutile-type structure of MgF<sub>2</sub> bulk for exploring the landscape of the clusters. This has not been much of a concern, as we have shown in the previous chapter that the potential reproduces the qualitative features (especially the local minima) of the true ab initio landscape quite satisfactorily.

### 5.6.2 Experimental limitations

Raman intensities of  $\text{MgF}_2$  powder are low compared to a  $\text{MgF}_2$  crystal and are further reduced by the limited thickness of the thin films. Thus, the detection of a Raman signal of an amorphous  $\text{MgF}_2$  film is difficult. The same holds for the matrix spectroscopy, where we have also a low concentration of  $\text{MgF}_2$  species. Because of this background we are not able to draw stronger conclusions from the spectra obtained. It is also possible that in the argon matrix the gas phase species combine together during the deposition and formed larger clusters. Furthermore, the magnesium fluoride clusters interact with the matrix atoms (matrix damping effect). Both processes can lead to band shifts, intensity anomalies, or to new visible bands.

## 5.7 Conclusion

In order to characterize the clusters present in the gas phase during the LT-ABD process, we have calculated the Raman and infra-red spectrum of these structures and of various predicted bulk  $\text{MgF}_2$ -polymorphs (including Raman and infra-red intensities for the clusters). We have compared these results with experiments performed in the context of the low-temperature atom beam deposition synthesis of  $\text{MgF}_2$  polymorphs. We find that the monomer M1 and the dimer D2 constitute only a minor part in the gas phase during the synthesis and find evidence that most likely, several charged species are also present. We have also discussed the possibility of following the amorphous to crystalline transition of  $\text{MgF}_2$  by following the intensity of the broad peak at about  $800\text{ cm}^{-1}$  which is most likely due to the dangling fluorine atoms in three-coordinated Mg atoms. Finally, in our calculations, we can identify two characteristic Raman active frequencies at around  $475\text{-}480\text{ cm}^{-1}$  and at about  $800\text{ cm}^{-1}$  for the short and long linear polymorphs of  $(\text{MgF}_2)_n$  which can also serve as a fingerprint for such chain-like structures both in clusters and bulk phases of  $\text{MgF}_2$ . Since the peaks discussed are present in all matrix samples investigated, it is unlikely that impurities are the reason for their existence.

## 5. AB INITIO RAMAN AND IR SPECTROSCOPY

---

**Table 5.2:** Assignment of observed frequencies in vapor phase.

Frequency( $\text{cm}^{-1}$ )	S (38)	M(135)	H(140)	L(37)	F(48)	This work
240(IR)		M1, Polymer				D1
248,249(IR)	M1			D2	D1	D1
283, 291, 307(IR)						T1, T2, TA5
354(Raman)				Dimer	D2	D2,T2
450(IR)		Polymeric				T1,T3,T6
477(IR)		M1		No MgF2	No MgF2	M1, T1, T3, T6
490S, 483M,486.6H, 486.5L (IR)	Polymeric	Polymeric	D1,D2	D1,D2	D1,D2	D1,T3
548(IR)				MgF2X	D2	D2
550(Raman)				M1	M1	M1
584(Raman)						D2
(738.2, 732.8, 726.5)(IR)		MC1				DA1,MA1
(745.9,741.1, 735.4)(IR)	Polymeric	MC1		D1,MgF	MgF	D1, T2, T3
850, 840,842.3, 841.8(IR)	M1	M1	M1	M1	M1	M1

## Part VI

# Molecular Dynamics simulations





# 6

## Atomistic modeling of the LT-ABD method

### 6.1 Introduction

In this section, we present the results of molecular dynamics simulations of the deposition of  $\text{MgF}_2$  clusters of various sizes on the  $\text{Al}_2\text{O}_3$  substrate and subsequent annealing of the deposit. We also discuss the kinetic stability of the yet-unknown anatase polymorph of  $\text{MgF}_2$ . The previous two chapters have described a detailed study on the vapor phase of  $\text{MgF}_2$ . The logical next step is to deposit precisely the species identified onto the  $\text{Al}_2\text{O}_3$  substrate used in experiment. There has been a significant experimental interest in synthesizing  $\text{MgF}_2$  thin-films for optimizing the optical properties. However, we have not come across any theoretical study that discusses the atomistic growth process of  $\text{MgF}_2$ .

### 6.2 Setting up the substrates for deposition

#### 6.2.1 $\alpha\text{-Al}_2\text{O}_3$ substrate

Before proceeding with the actual deposition, we need to have a stable equilibrated surface in order for the simulations to succeed. In the case of  $\text{Al}_2\text{O}_3$ , the slab was chosen in such a way as to expose the oxygen-terminated (0001) surface. Although the Al-terminated surface had been previously calculated to be more stable than the O-terminated (0001) surface (141), we still decided to use the latter in order to reproduce more closely the experimental conditions. It has been shown in ultra-high vacuum experiments that this substrate is oxygen terminated in the presence of major impurities such as argon, nitrogen and water (142, 143). Since the pressure in the experimental chamber before starting deposition was around  $10^{-8}$  bar and the substrate had not been specially treated with any cleaning process, we expected the exposed Al

## 6. ATOMISTIC MODELING OF THE LT-ABD METHOD

---

layer to be passivated with O and other species present in the chamber within a few seconds. Therefore, it is reasonable to assume an O-terminated surface as a starting configuration before deposition was initiated.

The slab chosen for deposition comprised 3600 atoms and was obtained by constructing an ABA stacking of close-packed planes of O atoms. Six close-packed planes made of 120 oxygen atoms and with lateral dimensions of  $50.4 \text{ \AA} \times 48.5 \text{ \AA}$  were used. The nearest-neighbor distance between O atoms was  $2.8 \text{ \AA}$ . Two thirds of the octahedral hollow sites between two adjacent close-packed O-planes were filled with Al atoms, in such a way to reproduce the known crystal structure of  $\alpha$ -alumina. During the simulation, the bottom two planes comprising of oxygen and aluminium atoms were fixed so as to reproduce the stabilizing effect of the bulk sample. Then, the initial slab was locally minimized by using an MD-assisted quenching procedure. At each MD step, after solving the classical equations of motion via the velocity-Verlet algorithm, the quenching was accomplished by canceling all those components of an atom's velocity whose scalar product with the force acting on the atom was negative. Periodic boundary conditions across the plane parallel to the xy-plane were applied. Upon quenching, the topmost plane of oxygen atoms was observed to relax inwards, in such a way to reduce the surface dipole moment. This effect has also been observed experimentally in an extremely clean environment under very low vapor pressures.

Before initiating the actual deposition, the minimized slab was equilibrated by performing MD for a time interval of around 1 ps and at the temperature of the deposition. A simple thermostat based on velocity rescaling was used and applied to all atoms lying within a distance less than one third of the slab height from the bottom of the slab. The equilibrated structure was then used as the substrate for the deposition and growth simulation.

The minimized and equilibrated slab at 1000K is shown in Figure 6.1. The inward relaxation of the top-most Oxygen plane can be seen.

### 6.2.2 MgF<sub>2</sub>-anatase substrate

The anatase structure can be stabilized for TiO<sub>2</sub> up to a thickness of 20 nm in vacuum (144). By depositing on a hypothetical substrate for anatase-MgF<sub>2</sub>, we can test the kinetic stability of this structure at different conditions and generally study whether epitaxial growth and subsequent tempering will yield the same anatase-type structure or transform into the rutile structure.

We chose to expose the (011) and (100) faces based on previous studies on the stability of the TiO<sub>2</sub>-anatase structure and electronic structure calculations of surface energies using the CRYSTAL'09 suite. For the purpose of studying epitaxial growth, we feel it would be sufficient to explore low-index surfaces only.

For the (011) slab, the starting structure was terminated by fluorine atoms and comprised 3360 atoms. The simulation cell dimensions were  $53.50 \text{ \AA} \times 52.22 \text{ \AA}$  in the x and y directions respectively. The MgF<sub>2</sub>-anatase unit cell used to produce this slab had dimensions of  $a=3.822 \text{ \AA}$ ,  $b=3.822 \text{ \AA}$  and  $c=9.719 \text{ \AA}$ . Next, after tempering for 2 ns, we saw a significant relaxation of the top most layer of F-atoms, quite similar to the

## 6.2 Setting up the substrates for deposition

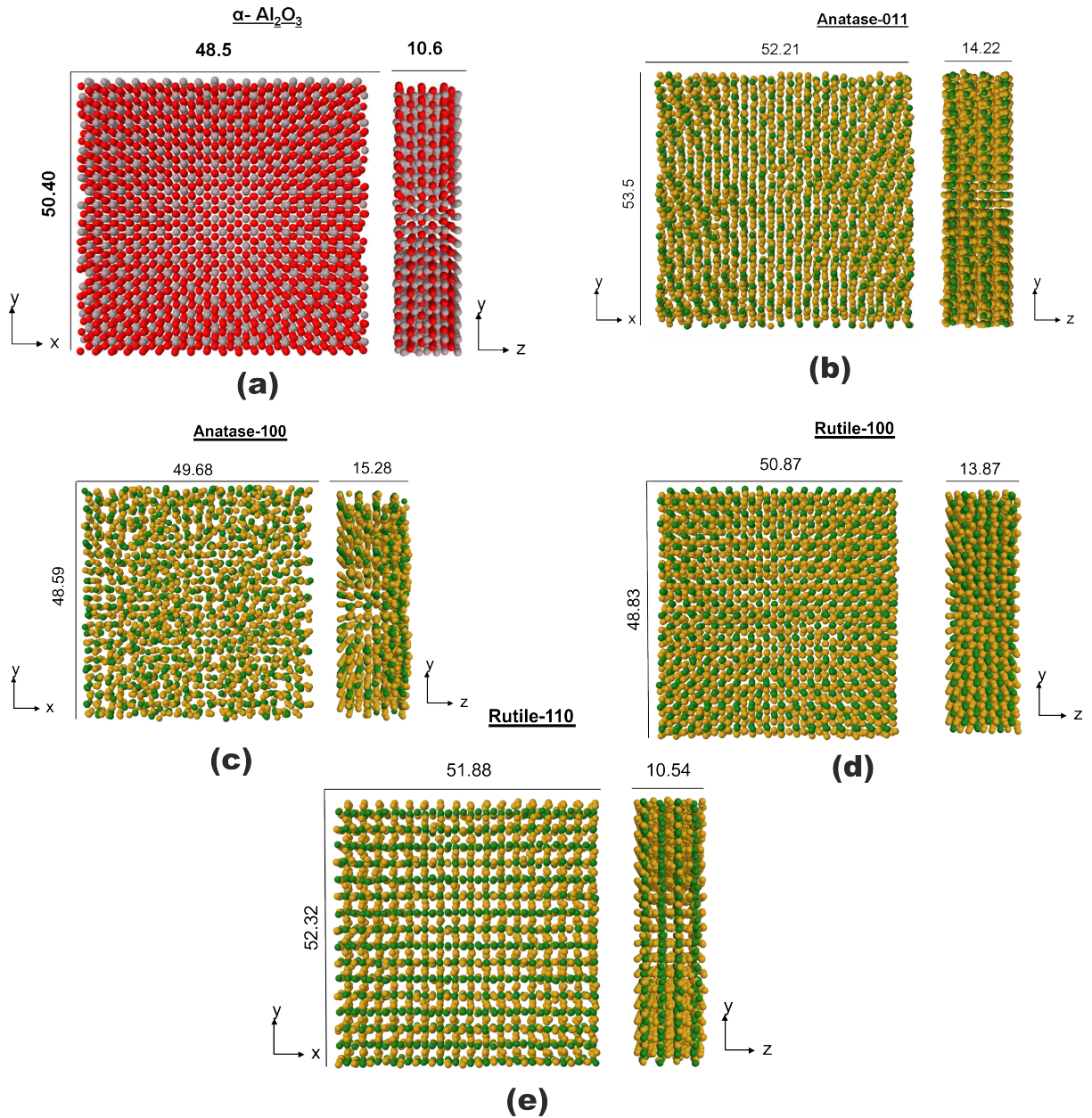


Figure 6.1: Substrates used for deposition- (a)  $\alpha\text{-Al}_2\text{O}_3$  (b)  $\text{MgF}_2\text{-anatase (011)}$  (c)  $\text{MgF}_2\text{-anatase (001)}$  (d)  $\text{MgF}_2\text{-rutile (100)}$  (e)  $\text{MgF}_2\text{-rutile (110)}$

## 6. ATOMISTIC MODELING OF THE LT-ABD METHOD

---

case of  $\text{Al}_2\text{O}_3$  described above. The starting and final structures at 1000K are shown in Figure 6.1. This is the highest temperature at which these slabs are equilibrated.

The (100) slab comprised 3120 atoms and the top-most layer had both Mg and F atoms. The simulation cell dimensions were  $48.59 \text{ \AA} \times 49.69 \text{ \AA}$  in the x and y directions respectively. Here too, we see a significant relaxation of the top-most layer that is most pronounced at 1000K as can be seen from Figure 6.1.

### 6.2.3 $\text{MgF}_2$ -rutile substrate

The rutile structure was stabilized with the (100) and the (110) surfaces exposed. The (100) slab comprised 3168 atoms and the dimensions were  $48.83 \text{ \AA} \times 50.87 \text{ \AA}$ . For the (110) slab, comprised of 3264 atoms, the slab's dimensions were  $51.88 \text{ \AA} \times 52.32 \text{ \AA}$  in the x and y directions. In a previous ab initio study on  $\text{MgF}_2$  surfaces (145), these faces were found to be the thermodynamically most stable ones. They are shown in Figure 6.1.

## 6.3 Setting up the vapor phase

In a previous study of Xenon deposition, it was found that up to experimental vapor pressures from  $10^{-7}$  to  $10^{-3}$  bar, no clusters of Xenon were formed. Subsequently, a deposition of single atoms at different rates was studied (22). However, in the context of an ionic system like  $\text{MgF}_2$ , it is clear that this will not be the case. The previous two chapters have described details of an energy landscape and Raman investigation on the vapor phase of the experiment being modeled. Especially from the results of the Raman investigation, it is clear that the linear monomer and the  $D_{2h}$  dimer are present in our experimental setup, among other possible structures. The exact distribution and percentages of these clusters remains unclear, however. Thus, we have deposited these two clusters with a probability of 0.5 each. The initial distance of the particle was set at  $10 \text{ \AA}$  above the the growing surface. The x and y coordinates of the impinging cluster were chosen randomly. In a separate study, we also deposited bigger clusters of up to 45 atoms in order to see the effects of changing the gas phase composition on the deposit.

The rate of cluster deposition was varied from 4.5 atoms every 1000 MD (high-rate) steps to 4.5 atoms every 10,000 MD steps (low-rate). This is in contrast with most MD studies on molecular beam epitaxy that tend to start with a monoatomic gas phase/plasma or deposit atoms in a particular stoichiometric ratio (22). We also deposited big clusters found from the simulated annealing study performed in the previous chapter. Two clusters of 45 atoms and 30 atoms were deposited in with a probability of 0.8 and 0.2 respectively. In the case, the average deposition rate was 42 atoms per 1000 MD steps and 10,000 MD steps at 50K and 1000K respectively.

## 6.4 Deposition

### 6.4.1 Deposition on $\alpha - Al_2O_3$

We first simulated the deposition at a rate of about  $10^{12}$  atoms/s and about  $10^{10}$  atoms/s. This translated to a new cluster being deposited on the substrate every 1000 and 10000 MD steps respectively (1 MD step = 2 fs). This deposition rate is much faster than the experimental deposition rate, of course.

Independent of the rate of deposition or temperature of the substrate, we always obtain an amorphous deposit after depositions on a cold substrate at these two rates with the temperature being greater towards the top of the deposit. Figure 6.2 shows an example of the structure obtained after deposition at 50K and 1000K (the lowest and highest temperatures for depositions studied) on the  $\alpha-Al_2O_3$  substrate. It is interesting to note that we see epitaxial growth at even the fastest rates on the hypothetical  $MgF_2$ -anatase and  $MgF_2$ -rutile substrates at substrate temperatures of 1000K.

At 1000 K, the 6681 atoms deposited on  $\alpha-Al_2O_3$  substrate produced a film of thickness of around 75 Å whereas for the amorphous deposit at 50 K, the thickness for the same number of atoms was 90 Å. A bin of 4 Å is chosen in order to make sure that layers containing only a small number of atoms are not underrepresented. (See 6.2b) when computing average temperature.

Snapshots at four different intervals of time during deposition are shown in Figure 6.2a. We can therefore conclude that  $MgF_2$  films would follow the island type growth process on  $Al_2O_3$  substrate at both high and low temperatures.

### 6.4.2 Analysis of the deposition

We study the amorphous deposit during deposition with respect to the following data: (1) the temperature gradient along the z-axis, (2) coordination histograms, (3) radial distribution function and (4) bond-distance histograms. These are shown in Figure 6.3.

We note that the radial distribution function is an important feature for the comparison with the transmission electron microscopy experiment. This is discussed in detail in the methods section.

There appears to be a positive temperature gradient (See figure 6.3(a)) across the deposit from top to bottom with the top layers being hotter than the bottom-most layers. This behavior is observed at temperatures of 300K, 500K and 1000K as well. The reason is that the thermostat is applied only at the bottom of the substrate and the time between individual depositions is not long enough for the energy of the deposited cluster to completely dissipate out of the system. The gradient remains the same for deposits generated at a lower rate too. In contrast, in the work on deposition of Xenon, it was found that the layers have largely the same temperatures. This could be a result of the ionic nature of the Mg-F interactions that do not permit heat diffusion easily even at high temperatures by reducing the number of collision during deposition.

## 6. ATOMISTIC MODELING OF THE LT-ABD METHOD

---

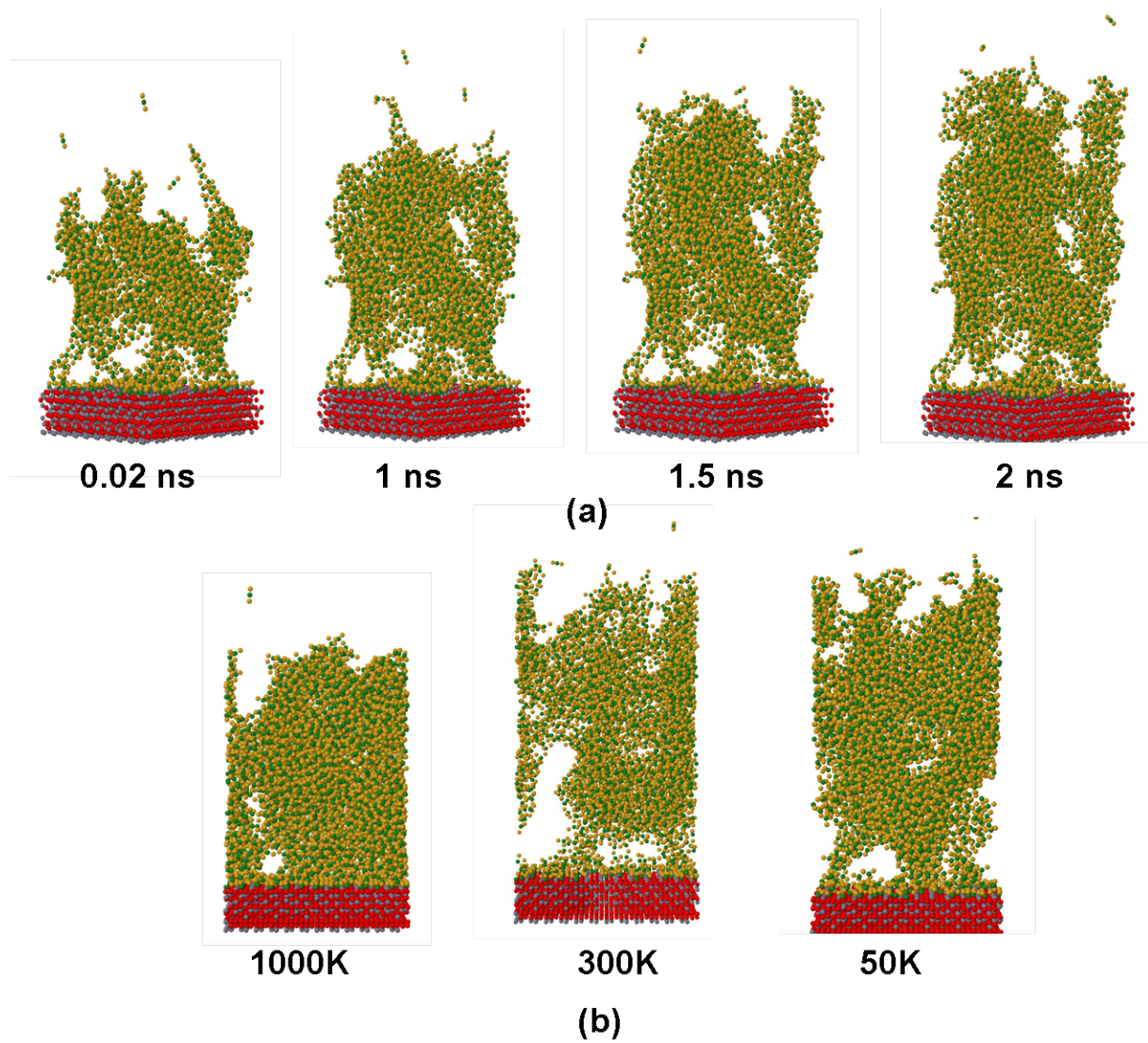


**Figure 6.2: Deposition at different temperatures** -(a) The figure shows different stages of growth of the amorphous  $\text{MgF}_2$  deposit at 50K. (b) Amorphous deposits at three different temperatures of 1000K, 300K and 50K. .

The tight packing in Xe with practically no voids inside the deposit implies that the temperature can be easily distributed across all atoms through collisions leading to a better averaged kinetic energy throughout the deposit and the heat dissipation is mostly controlled by the substrate-deposit interface.

The fluorine-fluorine coordination ranges from 5 to 15 with a peak at 12 growing with time. We note that the coordination of 12 is required for the hcp arrangement in the  $\text{CaCl}_2$ -type structure (rutile shows tetragonal fluorine atom packing with a 11 fold F-F coordination). The radial distribution function indicates that absolutely no long-range order is present in the final deposit after deposition at all temperatures and rates studied. Average Mg-F, Mg-Mg and F-F bond lengths of 1.96 Å, 2.5 Å and 4 Å are found in the deposit at 50K.

## 6.5 Tempering

After the deposition stage resulting in amorphous structures as described above for deposition at temperatures ranging from 50K to 1000K, we tempered these deposits first at the temperatures at which these were grown. However, even after tempering at 1000K for 18 ns, we did not find an ordered deposit. Thus, keeping the computational time expenses in mind, we performed tempering runs of five different amorphous structures grown at 50K at 1500K and 2000K (the experimentally reported melting point of  $\text{MgF}_2$  is 1536K (146)), but it must be noted that most empirical potentials fitted for bulk systems do not reproduce melting points in general and tend to under or over estimate this value significantly. Given the constraints of time and computational effort, we performed a long tempering on a few deposited amorphous layers, where the high temperatures essentially accelerate the diffusion and lead to ordering within the the first nanosecond of the simulation time.

We observed that for all amorphous samples studied (i.e the ones generated using big clusters, small clusters and different temperatures), tempering at 1500K led to a structure exhibiting some ordering within a simulation time of approximately 1 ns. The driving force for formation of an ordered structure is the formation of a fully ordered layer at the substrate-deposit interface. As soon as this is achieved, the ordering process begins in a bottom-up fashion. This process is clearly observed at 1500K with accelerated diffusion. Figure 6.4 shows snapshots that clearly indicate this bottom-up ordering process. The temperature of 2000K is found to be too high since the deposit becomes liquid like and remains that way for the duration of the simulation.

The change in total energy of the system during the annealing process can be seen in Figure 6.5 at 1000K and 1500K: the energy of the low-temperature deposit significantly increases during tempering as a result of an increase in kinetic energy. After a certain point in time, the process of ordering begins and the energy reduces drastically as more and more bonds are formed. After about 1 ns, the system equilibrates and the bottom-up ordering process is nearly complete. At 2000K, the crystallization step does not occur as the deposit remains liquid-like.

## 6. ATOMISTIC MODELING OF THE LT-ABD METHOD

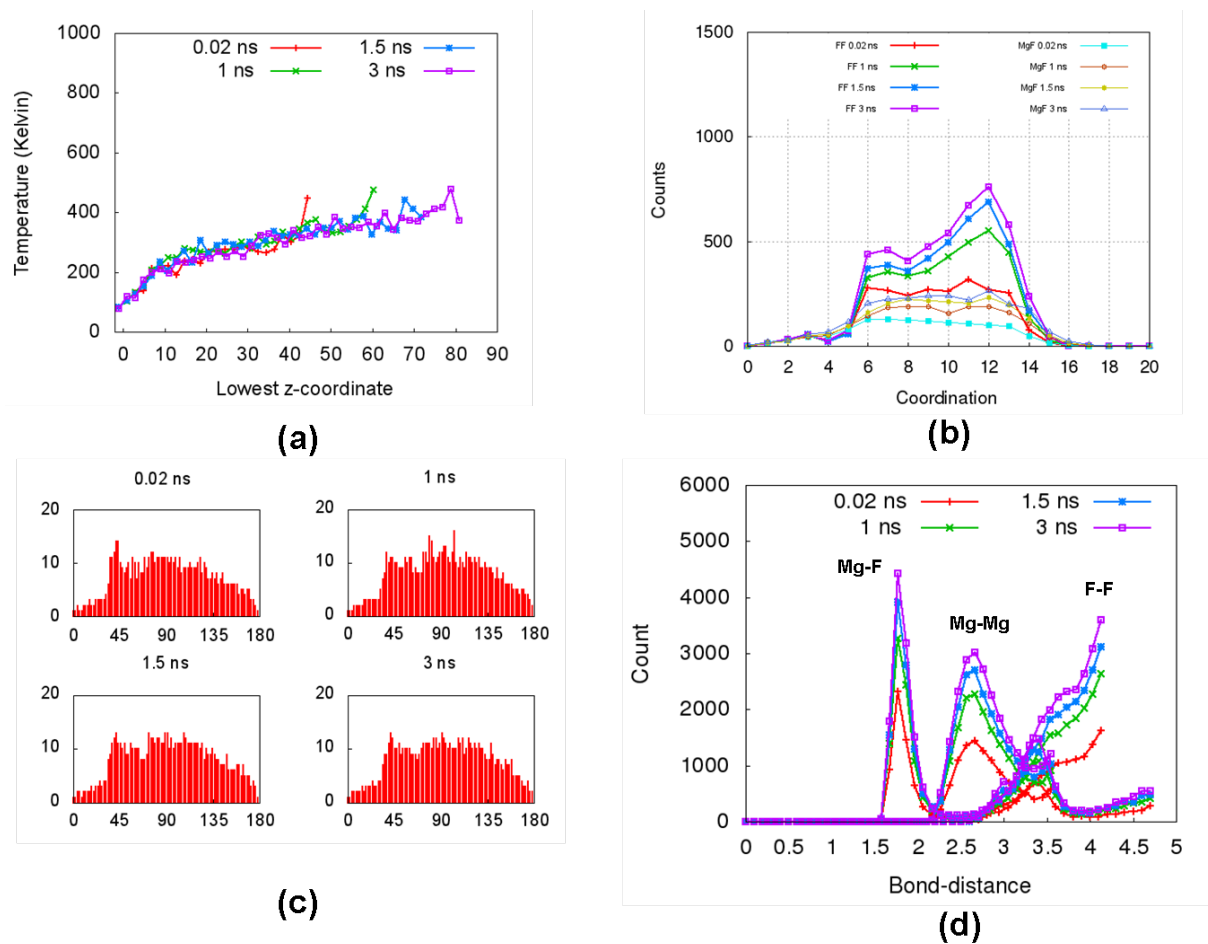
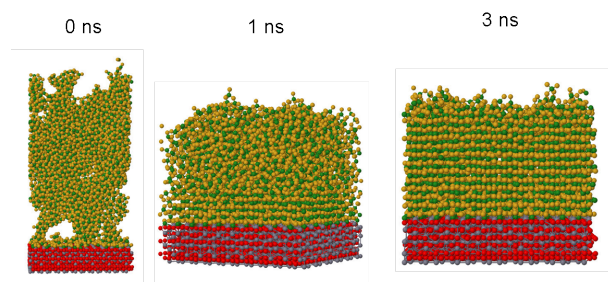


**Figure 6.3: Analysis of deposition at 50K-** The figure shows (a) The temperature gradient normal to the substrate at different time-steps (b) F-F and Mg-Mg coordination numbers at different time steps (c) F-F bond angle histograms and (d) Bond-distances of Mg-F, Mg-Mg and F-F bonds distributed across the deposit. .



**Figure 6.4: Snapshots of annealing at 1500K-** The figure shows different stages during the annealing process starting from an amorphous structure obtained at 50K to an ordered deposit.



We saw during deposition that for all the choices of deposition parameters, the temperature of the deposit increased gradually in the direction normal to the exposed plane of the substrate. During the tempering stage however, this trend is reversed almost instantly. The reason is that our thermostat is placed at the bottom of the substrate. Without new deposited clusters adding kinetic energy at the top, it is easy to see why this happens. The trend is illustrated in Figure 6.5 where we can see the temperature change as a function of the  $z$ -coordinate in bins of  $4 \text{ \AA}$ . A bin of  $4 \text{ \AA}$  was chosen to make sure that at least 100 atoms were involved in the computation of the average the kinetic energies per layers. The temperature of the layer is then calculated from the kinetic energies via the law of equipartition of energy.

### 6.5.1 Structural features of the deposit

All structures after annealing for 1 ns at 1500K show an hcp-like packing of fluorine atoms as indicated by an ABAB type stacking of the fluorine layers (See figure 6.6). Experimentally, the amorphous to rutile phase transition has been suggested to proceed via the  $\text{CaCl}_2$ -type structure through an order-disorder type phase transition. The arrangement of fluorine atoms should be that of a tetragonal close packing for the structure to be classified as rutile-type whereas in the  $\text{CaCl}_2$ -type structure, the fluorine-fluorine coordination should be equal to 12. However, a well-known shearing of the  $\text{CaCl}_2$ -type structure easily transforms it into the rutile-type structure (147). Thus, understanding the behavior of the fluorine atoms becomes key to understanding the precise crystalline structure of the ordered deposit.

A clearer picture emerges when we look at the polyhedral connections along the  $y$ - $z$  and  $x$ - $z$  planes in sections of  $3\text{-}4 \text{ \AA}$  thickness along the  $x$  or  $y$  directions. We see that while the ABAB type stacking of fluorine atoms is consistently maintained, the magnesium atoms are distributed across the deposit so as to enable the existence of several different crystal types, and in particular, two specific ones: while a major part of the annealed deposit contains  $\text{CaCl}_2$ -type edge-sharing octahedral connections, we also see the emergence of regions containing  $\text{CdI}_2$ -type nuclei. Both these configurations can

## 6. ATOMISTIC MODELING OF THE LT-ABD METHOD

### Annealing at 1500K

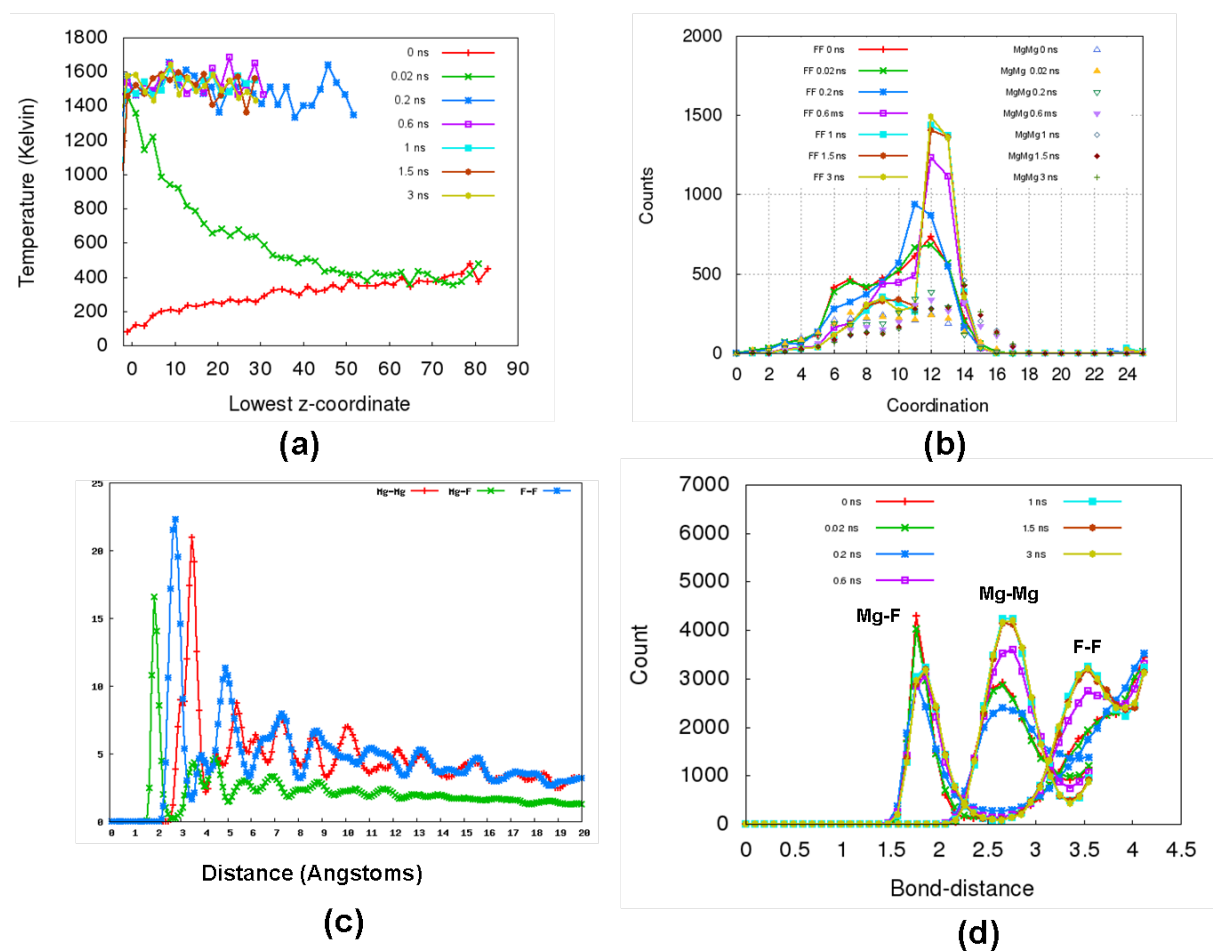


**Figure 6.5: Analysis of anneal at 1500K-** The figure shows different stages during the annealing process starting from an amorphous structure obtained at 50K to an ordered deposit.

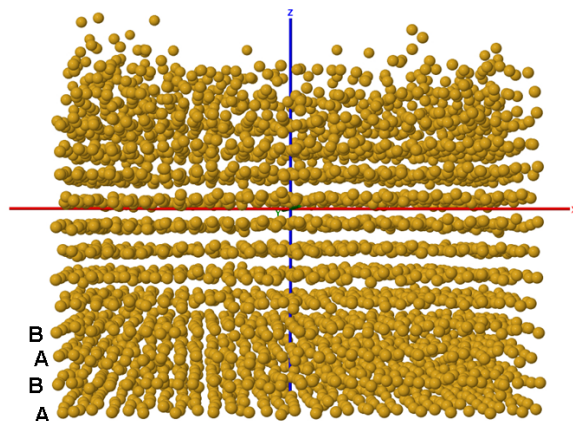


**Figure 6.6: ABAB stacking of fluorine atoms-** The figure shows ABAB type stacking of fluorine atoms in the annealed deposit at 1500K after 1 ns. The magnesium atoms are hidden from view. .

co-exist while maintaining an hcp-arrangement of the fluorine atoms. The  $\text{CdI}_2$ -type crystal structure had also been predicted to be a kinetically stable local minimum on the energy landscape by Wevers et al. (21, 41). The polyhedral patterns can be seen in Figure 6.7. On quenching this configuration, we can clearly recognize the existence of two nuclei distributed across the whole deposit.(See figure 6.8)

### 6.5.2 Mechanism

It can thus be argued that it is the presence of small regions containing the  $\text{CdI}_2$ -type nuclei that stabilizes the  $\text{CaCl}_2$ -type crystal in experiment. It has been argued from TEM studies performed in collaboration with X. Mu, Dr. Wilfried Sigle and Prof. P. Van Aken that, in fact the  $\text{CaCl}_2$ -type nucleus is stabilized by the grain-boundaries. However, the structure of the grain-boundary remained unclear. From our MD simulations, it would appear that the  $\text{CdI}_2$ -type arrangement of edge-sharing polyhedras should be a part of this grain boundary. The radial distribution functions of the model derived from experimental studies appear to match the model predicted by our MD simulations (148). Thus, it is possible that the grain boundaries are in fact of the  $\text{CdI}_2$ -type. This also opens up the possibility of varying simulation parameters in order to stabilize the  $\text{CdI}_2$ -type nucleus.

It has been previously argued that the diffusion of magnesium atoms within the hcp lattice of fluorine atoms leads to the observance of the  $\text{CaCl}_2$ -type structure due to averaging over distortions in the XRD/TEM experiments. However, we can see from the MD simulations that this is not the case. The  $\text{CaCl}_2$ -type structure is stable because of the competing  $\text{CdI}_2$ -type arrangement within the system. Over longer periods of time, the  $\text{CaCl}_2$ -type arrangement cannibalizes the  $\text{CdI}_2$ -type. Finally, when the crystal is

## 6. ATOMISTIC MODELING OF THE LT-ABD METHOD

---

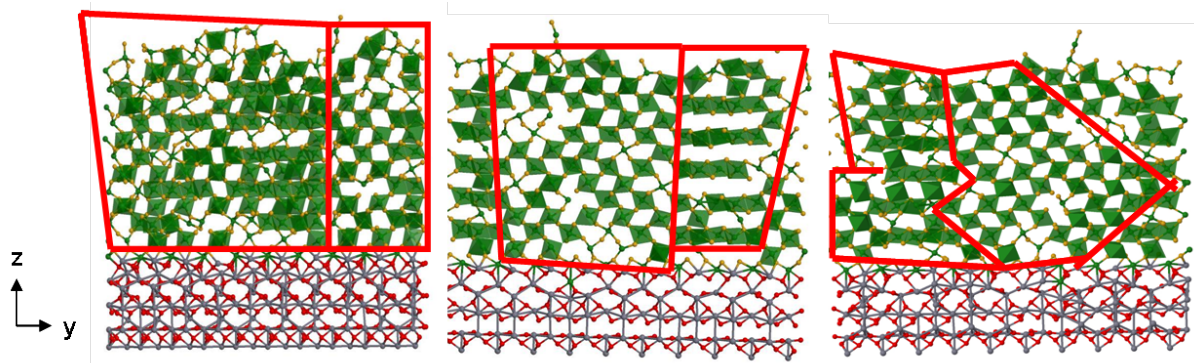


**Figure 6.7: Competing nuclei-** The figure shows the formation of two competing nuclei in the annealed deposit at 1500K after 1 ns. Two sections of 3 Å are cut across the y-z plane. .

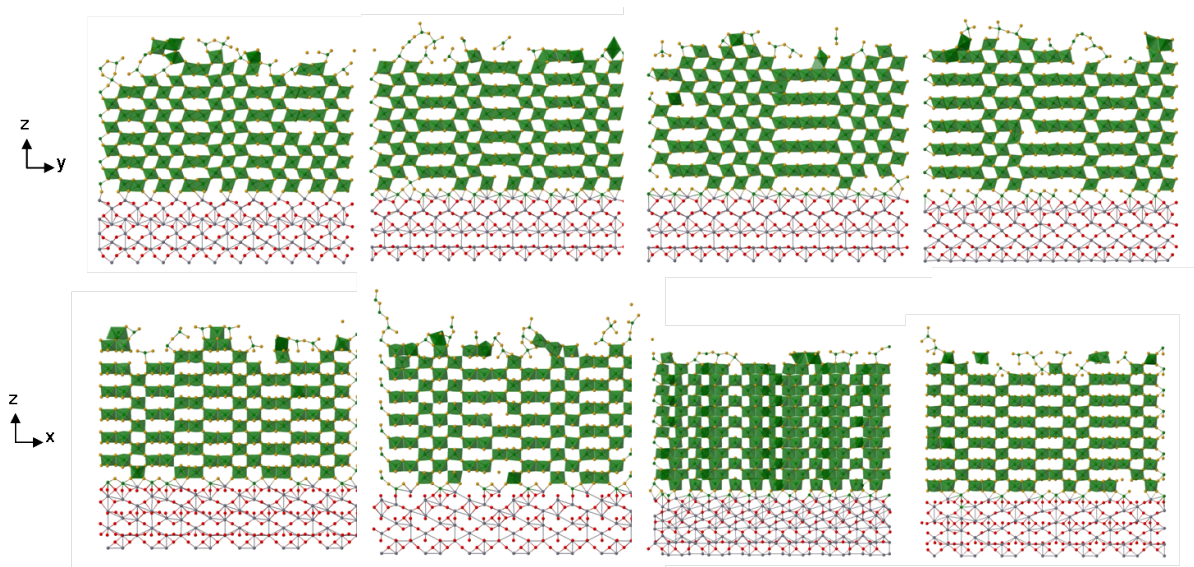


**Figure 6.8: Competing nuclei-** The figure shows the formation of two competing nuclei in the annealed deposit at 1500K after 1 ns followed by a quench. Sections of 3 Å are cut across the y-z and x-z planes. .

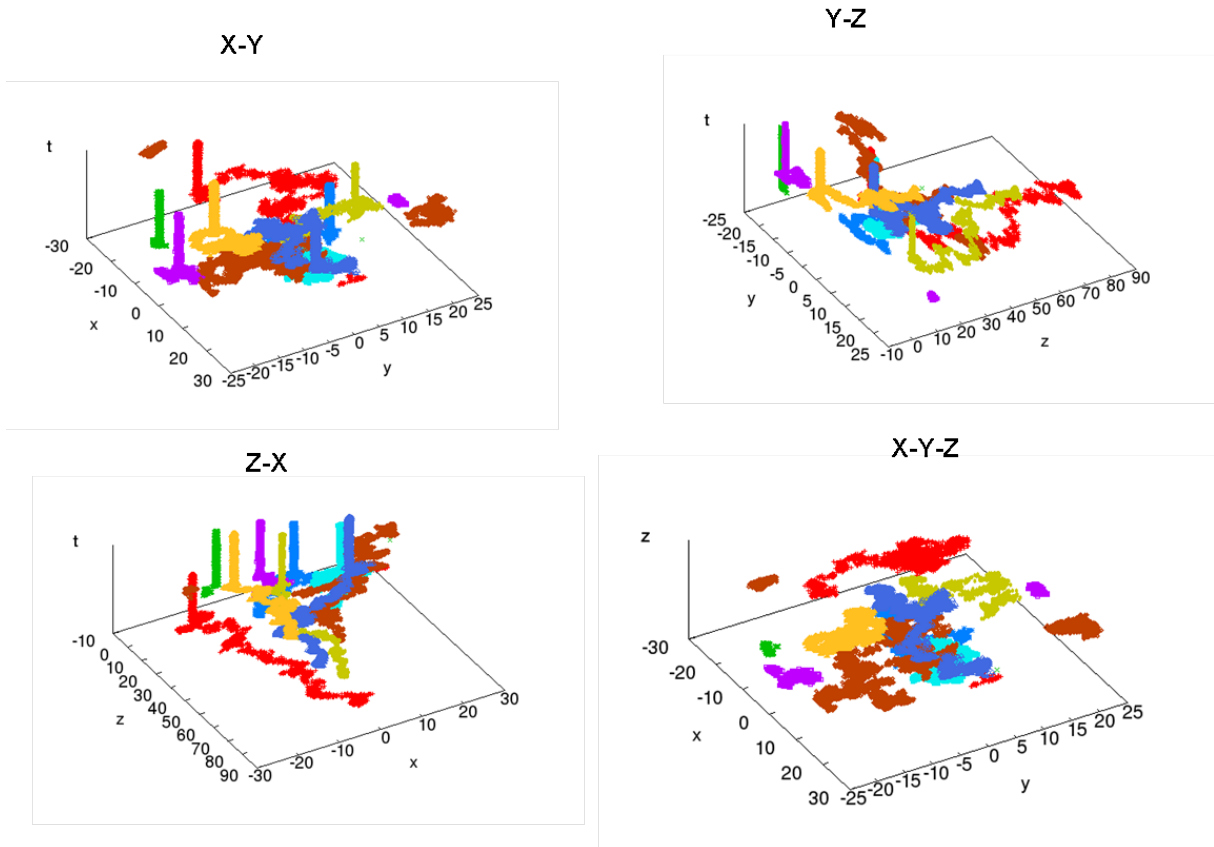


**Figure 6.9: Fluorine diffusion profiles-** The figure shows that during annealing, the fluorine atoms diffuse until crystallization occurs and then only vibrate along their lattice sites. .

big enough to make a  $C_2$  axis rotation (the shearing transformation mentioned earlier), the  $\text{CaCl}_2$  structure relaxes to the more stable rutile structure. The impediment of this mechanism would explain the stability of the metastable  $\text{CaCl}_2$  structure type in the experiment.

### 6.5.3 Diffusion profiles

In order to gain more insight into the kinetics of the deposition and annealing processes, the diffusion profiles of 9 fluorine atoms picked randomly at different points within the amorphous deposit are shown in Figure 6.9. It appears from the figure that after crystallization has occurred, hardly any movement of fluorine atoms takes place in the deposit and they essentially vibrate around fixed positions as expected. Similarly, from the diffusion profiles of the Mg atoms, we see that after crystallization, there is very

## 6. ATOMISTIC MODELING OF THE LT-ABD METHOD

---

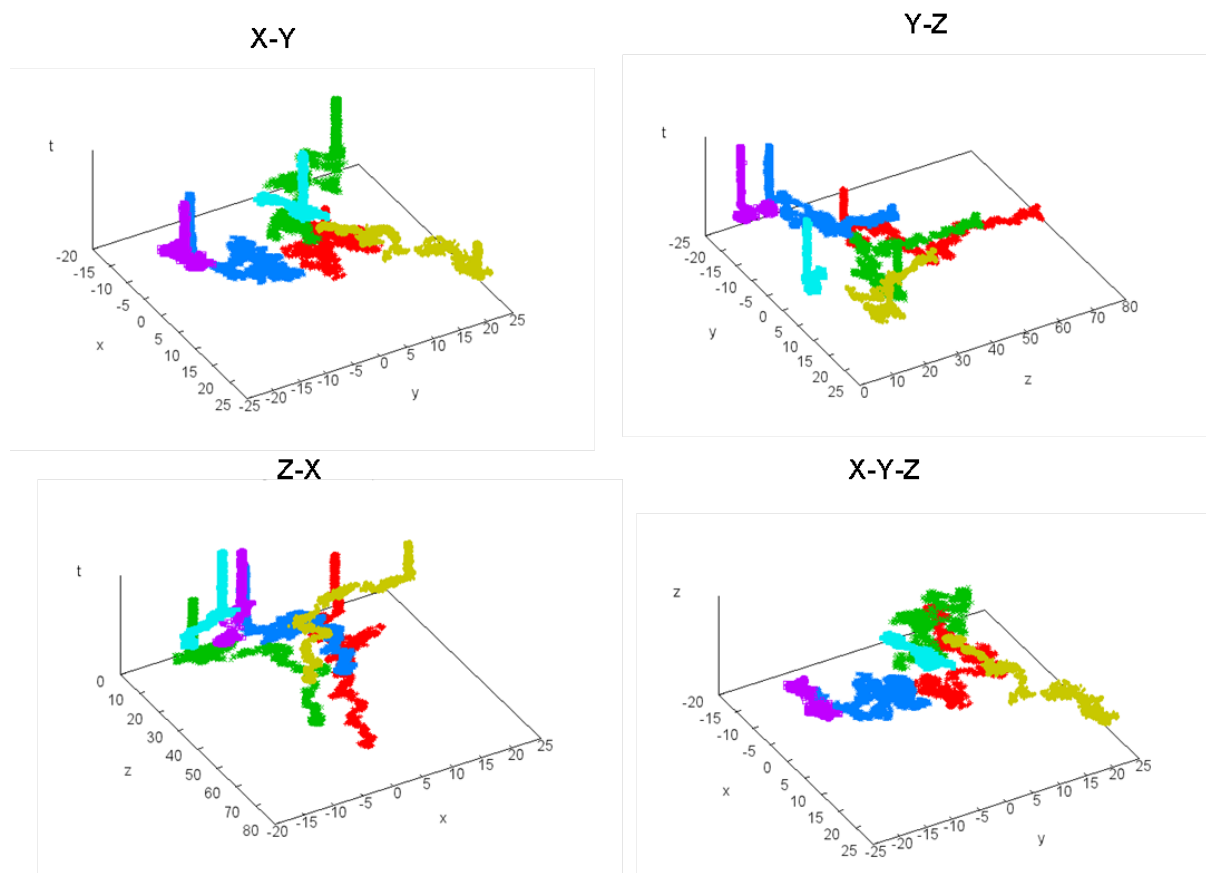


**Figure 6.10: Magnesium diffusion profiles-** The figure shows that during annealing, the magnesium atoms diffuse until crystallization occurs and then only vibrate along their lattice sites. .

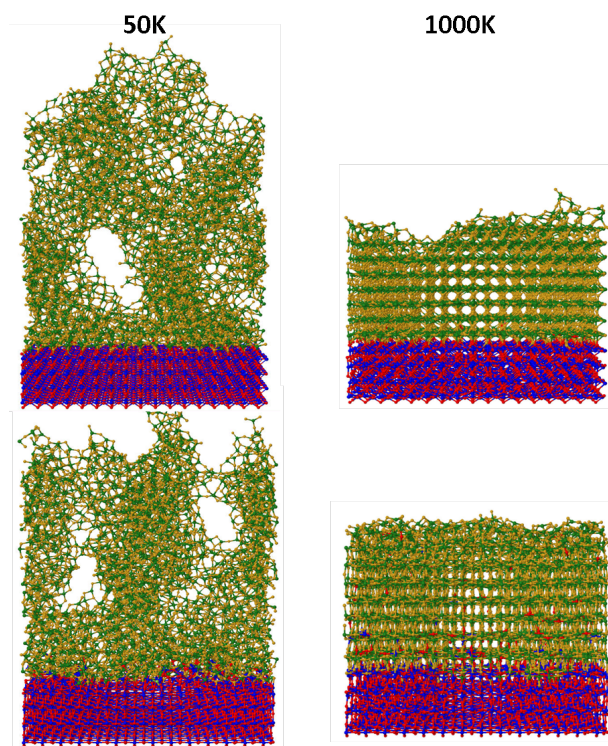


**Figure 6.11:** Deposition on  $\text{MgF}_2$  seeds- Amorphous and crystalline deposits obtained at 50K and 1000K for  $\text{MgF}_2$ -anatase and  $\text{MgF}_2$ -rutile seeds. .

little movement and the atoms tend to vibrate about their lattice positions. A sample of seven Mg atoms picked randomly is shown in Figure 6.10

## 6.6 Epitaxial growth and tempering on $\text{MgF}_2$ -anatase

From the energy landscape exploration on bulk  $\text{MgF}_2$ , ab initio local optimizations and the vibrational spectra of  $\text{MgF}_2$ -anatase, we can state with confidence that the anatase structure should be kinetically stable, at least at very low temperatures. However, the degree of kinetic stability of this structure still needs to be established. We note that we did not come across this structure during the amorphous-crystalline phase transition on  $\text{Al}_2\text{O}_3$  discussed above.

Assuming that we are able to stabilize a big enough nucleus, our MD simulations show that this structure should survive long enough as a meta-stable phase for experimental observation. During deposition on both rutile (110 and 001) and anatase (110 and 100) substrates, we find epitaxial growth in the structure as the substrate at 1000K. At 500K, the growth is a little more disordered. At low temperatures of 10K and 50K,

## 6. ATOMISTIC MODELING OF THE LT-ABD METHOD

---

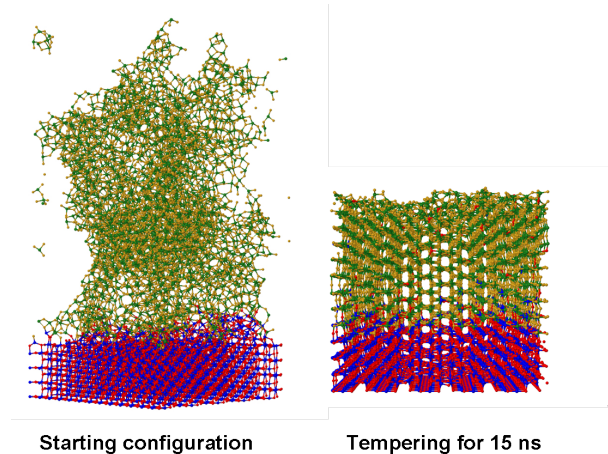


**Figure 6.12: Annealing on  $\text{MgF}_2$ -anatase-** Tempering the amorphous deposit for 15 ns at 1500K on the Anatase-110 substrate results in the formation of the Anatase-type structure. .

there is practically no diffusion during the deposition and thus we get amorphous deposits on all surfaces studied. This suggests that depositing at high temperatures on an anatase-compatible substrate might increase the likelihood of obtaining the anatase form, and this also shows the kinetic stability of this structure.

To test this proposition further, we anneal the amorphous structures obtained at low temperatures at a high temperature of 1500K for 18 ns. On both the anatase surfaces studied (100 and 011), the amorphous structure transforms to the anatase-type structure of the substrate within 2.1 ns (See figure 6.13). We can thus conclude that if a big enough seed of the anatase-type is formed, this structure can be stabilized for the  $\text{MgF}_2$  system. On the rutile substrate, the analogous process resulting directly in a rutile crystal occurs. In particular, we see no formation of a  $\text{CaCl}_2$ -type phase or stacking faults that result in the  $\text{CdI}_2$ -type structures on the  $\text{Al}_2\text{O}_3$  substrate.

### 6.7 Radial distribution functions

The structural evolution of  $\text{MgF}_2$  from an amorphous deposit through a metastable phase to the thermodynamically stable polymorph is also studied by comparing pair distribution functions extracted from energy-filtered electron diffraction and our molecular-dynamics simulations. To do so, we calculate radial distribution functions of all the structures studied at different points in time. These enable us to figure out exactly when long-range order is established in the system. We also compare models generated from our MD simulations with the pair distribution functions derived by X. Mu and Prof. Peter Van Aken at the Stuttgart Center for Electron Microscopy. We find excellent agreement for the amorphous structure found experimentally at a temperature of



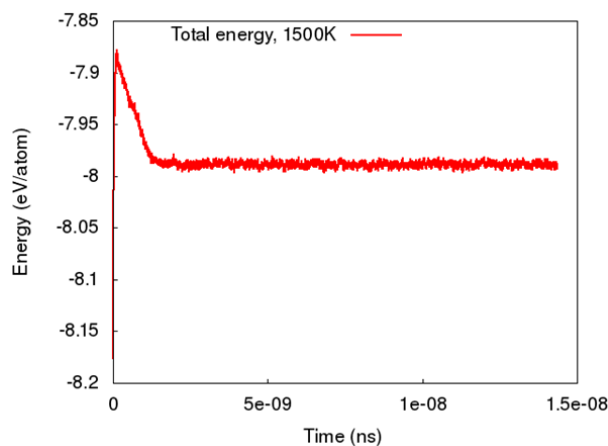


**Figure 6.13: Energies during annealing on  $\text{MgF}_2$ -anatase-** The energy increases as the substrate is heated from 50K to 1500K. This is followed by a crystallization almost immediately resulting in the anatase-type structure. The system is in equilibrium as energies fluctuate around this structure. .

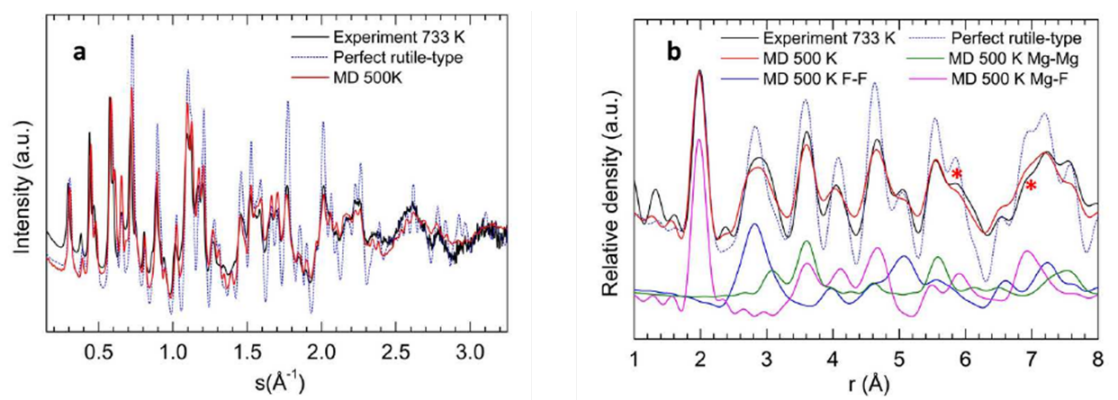
623 K.

Figure 6.14a shows the experimental structure factors of the specimen measured at 733 K (Fig. 6.14a, black solid line) and of the MD simulation at 500 K using all atoms of the MD cell (Fig. 6.14a, red solid line) and of the perfect model of rutile-type structure (Fig. 6.14a, blue dotted line). Peak positions of the experimental structure factor show good agreement with those of the perfect model of the rutile-type structure. This agreement confirms that the structure of the sample annealed at 733 K is close to rutile-type. However, the peaks of the experimental structure factor are strongly damped compared to the perfect rutile-type model. On the other hand, the experimental structure factor shows excellent agreement, both in peak heights and widths, with the structure factor calculated from the 500 K MD model. Because the 500 K MD simulation contains highly ordered as well as disordered regions, we conclude that the specimen annealed at 733 K also contains disordered regions. Most likely these regions correspond to grain-boundary regions (perhaps containing small  $\text{CdI}_2$ -type nuclei) because these represent a large volume fraction in the nanocrystalline structure of the specimen annealed at 733 K. The behavior of the structure factors is confirmed by the PDFs shown in Figure 6.14.

From the 500 K MD simulation result we calculate element-specific partial pair distribution functions (PDFs) (See Figure 6.15: F-F (blue), Mg-F (pink), and Mg-Mg (green)). These partial PDFs allow us to better understand the presence of peaks of the total PDFs. The first pronounced peak at 1.99 Å is due to the MgF first coordination shell. The second pronounced peak at 2.83 Å is mainly attributed to the first F-F coordination shell. The first and second peaks reveal the approximately average bonding angle of F-Mg-F of 90°, and confirms the existence of the Mg-centered  $\text{MgF}_6$  octahedra in the annealed specimen. The right shoulder of the second peak around

## 6. ATOMISTIC MODELING OF THE LT-ABD METHOD

---



**Figure 6.14: Comparison of RDFs-** (a) Structure factors obtained from experiment at 733 K (black, solid) and MD simulation at 500 K (red, solid), as well as the perfect rutile-type structure (blue, dot). (b) PDFs obtained from the experiment at 733 K (black, solid), MD simulation at 500 K (red, solid) and the perfect rutile-type structure (blue, dot). Also shown (bottom three curves) are the element-specific partial PDFs, FF (blue), MgF (pink), and MgMg (green), calculated from the atomic structure of the MD simulation at 500 K. Figure by X. Mu at Max Planck Institute for Intelligent Systems, Stuttgart.

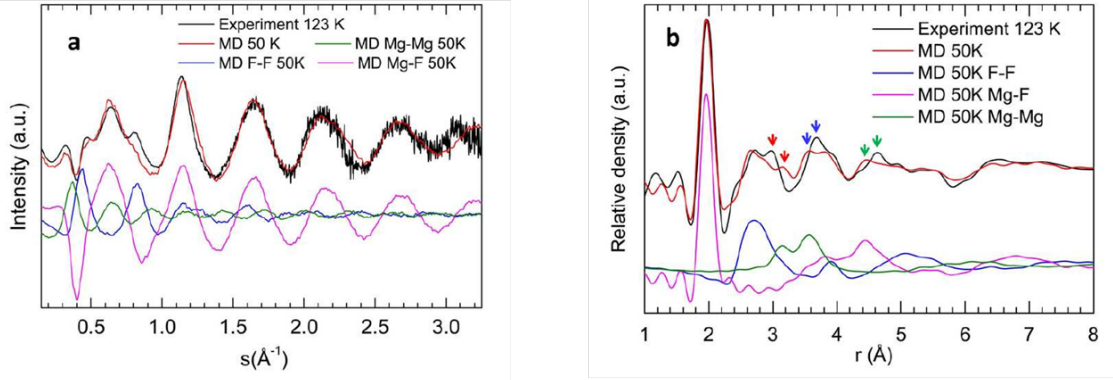


**Figure 6.15: Comparison of RDFs-** (a) Structure factors obtained from the experiment at 123 K (black) and MD simulation at 50 K (red), as well as the element-specific partial structure factors, FF (blue), MgF (pink), and MgMg (green), calculated from the MD model annealed at 50 K. (b) PDFs obtained from the experiment at 123 K (black), MD simulation at 500 K (red) and the element-specified partial PDFs (bottom three curves), FF (blue), MgF (pink), and MgMg (green), calculated from the atomic structure of the MD simulation at 50 K. Figure by X. Mu at Max Planck Institute for Intelligent Systems, Stuttgart.

3.10  $\text{\AA}$  and the third pronounced peak at 3.60  $\text{\AA}$  correlate with two Mg-Mg peaks which come from two different geometric configurations of the adjacent Mg-Mg atom pairs in the rutile-type structure. The first configuration is due to two adjacent  $\text{MgF}_6$  octahedra sharing one edge, i.e. two nearby Mg atoms share two F atoms, to form the first Mg-Mg coordination shell. The second configuration is due to two adjacent  $\text{MgF}_6$  octahedra sharing only one corner, namely one F atom, to form the second Mg-Mg coordination shell.

The experimental structure factor of the specimen deposited and measured at 123 K (Figure 6.15 black) shows a very good agreement to the structure factor of the 50 K MD simulation result (Figure 6.15 red line). The broad peaks in both structure factors confirm the amorphous structure. The element-specific partial structure factors, F-F, Mg-F, and Mg-Mg (Figure 6.15a) show that at large angles the total structure factor is dominated by the Mg-F partial structure factor. The F-F and Mg-Mg partial structure factors are strongly damped in the large-angle region. PDF and partial PDFs are shown in Figure 6.15b. Again, experimental and simulated total PDFs show excellent agreement. From the partial PDFs we see that the first pronounced peak at 1.99  $\text{\AA}$  corresponds to the Mg-F first coordination shell, the same as for the rutile-type. The peak around 2.72  $\text{\AA}$  in the experimental PDF correlates to the short-range structure of the FF octahedral structure. Compared to the crystalline state (Fig. 6.14), the peak at 2.72  $\text{\AA}$  is strongly damped in the experimentally obtained pair distribution functions of the amorphous material. This implies that the  $\text{MgF}_6$  octahedra are

## 6. ATOMISTIC MODELING OF THE LT-ABD METHOD

---

significantly distorted and some of the Mg atoms may even have only 4 or 5 F neighbors.

There are some small differences between the experimental and simulated PDFs marked by arrows in Fig. 6.15b. The red arrow on the 50 K MD PDF points out the first Mg-Mg peak which occurs when two adjacent Mg atoms share two F atoms (Figure 6.15, left, red dashed line), i.e. the first Mg-Mg coordination shell. The blue arrow on the 50 K MD PDF indicates the second Mg-Mg peak which corresponds to two adjacent Mg atoms sharing only one F atom, i.e. the second Mg-Mg coordination shell. As the contributions of the Mg-F peaks in the region between 2.9 Å and 3.8 Å are not expected to be very pronounced, the positions of the two arrow-marked peaks should mainly be dominated by the Mg-Mg contribution. Therefore, we assume that the mismatch of experimental and simulated PDF must be related to the two Mg-Mg geometries.

The experimental PDF shows also two different Mg-Mg geometries, as in the crystalline octahedral structure in the rutile-type phase. Since the red arrow at 2.97 Å in the experimental PDF should relate to the first Mg-Mg coordination shell, and the blue one at 3.68 Å should relate to the second Mg-Mg coordination shell, respectively, the mismatches marked by the red and blue arrows in Figure 6.15 can be attributed to different Mg-Mg distributions of the experimental and simulated structure. The first Mg-Mg coordination shell in the experiment has a larger radius than the one in the MD model, while the second Mg-Mg coordination shell in the experiment has a smaller radius than the MD simulation result. We note that this difference might be connected to the mismatch marked by the green arrow in Figure 6.15 which is contributed by the Mg-F pairs.

## 6.8 Conclusion

We modeled the growth of solid  $\text{MgF}_2$  from the gas phase on an  $\text{Al}_2\text{O}_3$  substrate, a  $\text{MgF}_2$ -anatase substrate and a  $\text{MgF}_2$ -rutile substrate as it occurs in a real low-temperature atom beam deposition experiment. The process was studied in all its stages, from the dynamics of  $\text{MgF}_2$  clusters in the gas phase, over their impact on the surface of the cold and hot substrates and their diffusion on the substrate, to the formation of crystallites. The growth process was studied as a function of synthesis parameters including the substrate temperature, deposition rate and type of clusters deposited.

Both high and low rates resulted in the formation of amorphous  $\text{MgF}_2$  deposits. On annealing, we discovered a possible mechanism for the stability of the  $\text{CaCl}_2$ -type structure. We find two competing structures in the first few nanoseconds of the deposition and argue that this competition stabilizes the  $\text{CaCl}_2$ -type structure long enough for experimental observations.

We also confirm the kinetic stability of the yet-unknown  $\text{MgF}_2$ -anatase polymorph by annealing an amorphous deposit on a hypothetical  $\text{MgF}_2$ -anatase substrate and find this structure to be stable. A nearly perfect layer-by-layer epitaxial growth was

achieved on both  $\text{MgF}_2$ -anatase and  $\text{MgF}_2$ -rutile at high temperatures.

## 6. ATOMISTIC MODELING OF THE LT-ABD METHOD

---

# References

- [1] ANTHONY K. CHEETHAM. *Science*, **264**(5160):794–795, 1994. 3
- [2] J. PANNETIER, J. BASSAS-ALSINA, J. RODRIGUEZ-CARVAJAL, AND V. CAIGNAERT. *Nature*, **346**:343–345, 1990. 3, 4
- [3] C. M. FREEMAN, J. M. NEWSAM, S. M. LEVINE, AND C. R. A. CATLOW. *J. Mater. Chem.*, **3**:531–535, 1993. 3, 4
- [4] J. C. SCHÖN AND M. JANSEN. *Angew. Chem. Int. Ed. Eng.*, **35**:1286–1304, 1996. 3, 12, 13
- [5] J. C. SCHÖN AND M. JANSEN. *Z. Krist.*, **216**:307–325;361–383, 2001. 3
- [6] M. JANSEN. *Angew. Chem. Int. Ed.*, **41**:3747–3766, 2002. 3
- [7] C. MELLOTT-DRAZNIKS. *J. Mater. Chem.*, **17**:4348–4358, 2007. 3
- [8] S. M. WOODLEY AND C. R. A. CATLOW. *Nature Mater.*, **7**:937, 2008. 3
- [9] J. C. SCHÖN AND M. JANSEN. *Int. J. Mat. Res.*, **100**:135–152, 2009. 3
- [10] J. C. SCHÖN, K. DOLL, AND M. JANSEN. *Phys Stat. Sol. (b)*, **247**:23–39, 2010. 3
- [11] M. JANSEN AND J. C. SCHÖN. *Z. Anorg. Allg. Chem.*, **624**:533–540, 1998. 3
- [12] J. C. SCHÖN, M. A. C. WEVERS, AND M. JANSEN. *J. Mater. Chem.*, **11**:69–77, 2001. 3
- [13] J. C. SCHÖN, Ž. ČANČAREVIĆ, AND M. JANSEN. *J. Chem. Phys.*, **121**:2289–2304, 2004. 3
- [14] Ž. ČANČAREVIĆ, J. C. SCHÖN, AND M. JANSEN. *Chem. Asian. J.*, **3**:561–572, 2008. 3
- [15] D. FISCHER AND M. JANSEN. *Angew. Chem. Int. Ed.*, **41**:1755–1756, 2002. 3, 5, 20
- [16] Y. LIEBOLD-RIBEIRO, D. FISCHER, AND M. JANSEN. *Angew. Chem. Int. Ed.*, **47**:4428–4431, 2008. 3, 4, 5, 20

## REFERENCES

---

- [17] G. V. VAJENINE, X. WANG, I. EFTHIMIOPOULOS, S. KARMAKAR, K. SYASSEN, AND M. HANFLAND. *Phys. Rev. B*, **in press**, 2009. 3
- [18] A. BACH, D. FISCHER, AND M. JANSEN. *Z. Anorg. Allg. Chem.*, **635**:2406–2409, 2009. 3, 5, 9, 20, 52, 63, 64
- [19] D. SANTAMARIA-PEREZ, A. VEGAS, C. MÜHLE, AND M. JANSEN. *Acta Cryst. B*, **67**:DOI: 10.1107/S010876811005370X, 2011. 3
- [20] J. C. SCHÖN, A. HANNEMANN, AND M. JANSEN. *J. Phys. Chem. B*, **108**:2210–2217, 2004. 3
- [21] J. C. SCHÖN, M.A.C. WEVERS, AND M. JANSEN. *J. Phys. A: Math. Gen.*, **34**:4041–4052, 2001. 4, 10, 14, 35, 44, 48, 62, 85
- [22] N. TOTO, J. C. SCHÖN, AND M. JANSEN. *Phys. Rev. B*, **82**:115401, 2010. 4, 78
- [23] JOEL BERNSTEIN, ROGER J. DAVEY, AND JAN-OLAV HENCK. *Angewandte Chemie International Edition*, **38**(23):3440–3461, 1999. 5, 11
- [24] DIETER FISCHER AND MARTIN JANSEN. *Journal of the American Chemical Society*, **124**(14):3488–3489, 2002. 5
- [25] DIETER FISCHER AND MARTIN JANSEN. *Angewandte Chemie International Edition*, **41**(10):1755–1756, 2002. 5
- [26] D. FISCHER, Z. CANCAREVIC, J. C. SCHN, AND M. JANSEN. *Zeitschrift für anorganische und allgemeine Chemie*, **630**(1):156–160, 2004. 5
- [27] M. P. ALLEN AND D. J. TILDESLEY. Oxford science publications. Oxford University Press, USA, June 1989. 6, 15, 27
- [28] M. KENNEDY, D. RISTAU, AND H.S. NIEDERWALD. *Thin Solid Films*, **333**(1-2):191–195, 1998. cited By (since 1996) 17. 9
- [29] *Thin Solid Films*, **342**(12):83 – 92, 1999. 9
- [30] L. DUMAS, E. QUESNEL, J.-Y. ROBIC, AND Y. PAULEAU. *Thin Solid Films*, **382**(12):61 – 68, 2001. 9
- [31] DETLEV RISTAU, STEFAN GÜNSTER, SALVADOR BOSCH, ANGELA DUPARRÉ, ENRICO MASETTI, JOSEP FERRÉ-BORRULL, GEORGE KIRIAKIDIS, FRANCESCA PEIRÓ, ETIENNE QUESNEL, AND ALEXANDER TIKHONRAVOV. *Appl. Opt.*, **41**(16):3196–3204, Jun 2002. 9
- [32] J. HAINES, J. M. LÉGER, F. GORELLI, D. D. KLUG, J. S. TSE, AND Z. Q. LI. *Phys. Rev. B*, **64**(13):134110, Sep 2001. 9
- [33] LC MING AND MH MANGHNANA. *Geophysical Research Letters*, **6**(1):13–16, 1979. 10



## REFERENCES

---

- [34] RS KRISHNAN AND RS KATIYAR. *Le Journal de Physique*, **26**, 1965. 10
- [35] R S KRISHNAN AND J P RUSSELL. *British Journal of Applied Physics*, **17**(4):501, 1966. 10
- [36] S. P. S. PORTO, P. A. FLEURY, AND T. C. DAMEN. *Phys. Rev.*, **154**(2):522–526, Feb 1967. 10, 29, 62, 64
- [37] MICHAEL L. LESIECKI AND JOSEPH W. NIBLER. *The Journal of Chemical Physics*, **64**(2):871–884, 1976. 10, 61, 62, 65, 68, 72
- [38] ALAN SNELSON. *The Journal of Physical Chemistry*, **70**(10):3208–3217, 1966. 10, 61, 62, 65, 72
- [39] J. BERKOWITZ. *J. Chem. Phys.*, **37**:1853, 1962. 10, 61
- [40] H.K. PULKER AND E. JUNG. *Thin Solid Films*, **4**(3):219 – 228, 1969. 10, 61
- [41] M. A. C. WEVERS, J. C. SCHÖN, AND M. JANSEN. *J. Solid State Chem.*, **136**:223–246, 1998. 10, 35, 55, 62, 85
- [42] M. A. C. WEVERS, J. C. SCHÖN, AND M. JANSEN. *J. Phys.: Cond. Matt.*, **11**:6487–6499, 1999. 10, 14, 35, 43
- [43] M A C WEVERS, J C SCHÖN, AND M JANSEN. *Journal of Physics A: Mathematical and General*, **34**(19):4041, 2001. 10
- [44] LIJUN ZHANG, YANCHAO WANG, TIAN CUI, YANMING MA, AND GUANGTIAN ZOU. *Solid State Communications*, **145**(5-6):283 – 287, 2008. 10
- [45] Y. A. NGA AND C. K. ONG. *The Journal of Chemical Physics*, **98**(4):3240–3245, 1993. 10
- [46] G GIGLI. *Journal of Chemical Physics*, **93**(7):5224–5233, OCT 1 1990. 10, 61
- [47] J AXTEN, M TRACHTAMN, AND CW BOCK. *Journal of Physical Chemistry*, **98**(32):7823–7831, AUG 11 1994. 10, 37, 61, 62
- [48] E FRANCISCO, AM PENDAS, AND A COSTALES. *Journal of Physical Chemistry A*, **106**(2):335–344, JAN 17 2002. 10, 36, 52, 61, 62, 65, 72
- [49] BK YSTENES. *Spectrochimica Acta Part A-Molecular and biomolecular spectroscopy*, **54**(6):855–868, JUN 1998. 10, 61, 62
- [50] E.D. SIMANDIRAS AND C.A. NICOLAIDES. *Chemical Physics Letters*, **223**(3):233 – 239, 1994. 10, 61
- [51] HARALD BRUNE. *Surface Science Reports*, **31**(46):125 – 229, 1998. 11
- [52] FEDERICO ROSEI AND RENZO ROSEI. *Surface Science*, **500**(13):395 – 413, 2002. 11
- [53] ELIAS VLIEG. *Surface Science*, **500**(13):458 – 474, 2002. 11

## REFERENCES

---

- [54] ANDREA C LEVI AND MIROSLAV KOTRLA. *Journal of Physics: Condensed Matter*, **9**(2):299, 1997. 11
- [55] H JONSSON. *ANNUAL REVIEW OF PHYSICAL CHEMISTRY*, **51**:623–653, 2000. 11
- [56] M. SCHNEIDER, A. RAHMAN, AND IVAN K. SCHULLER. *Phys. Rev. B*, **34**:1802–1805, Aug 1986. 11
- [57] E. T. GAWLINSKI AND J. D. GUNTON. *Phys. Rev. B*, **36**:4774–4781, Sep 1987. 11
- [58] S. M. PAIK AND S. DAS SARMA. *Phys. Rev. B*, **39**:1224–1228, Jan 1989. 11
- [59] W. D. LUEDTKE AND UZI LANDMAN. *Phys. Rev. B*, **40**:11733–11746, Dec 1989. 11
- [60] I. KWON, R. BISWAS, G. S. GREY, AND C. M. SOUKOULIS. *Phys. Rev. B*, **41**:3678–3687, Feb 1990. 11
- [61] P GUAN, D R MCKENZIE, AND B A PAILTHORPE. *Journal of Physics: Condensed Matter*, **8**(45):8753, 1996. 11
- [62] NORGE CRUZ HERNANDEZ AND JAVIER FERNANDEZ SANZ. *The Journal of Physical Chemistry B*, **105**(48):12111–12117, 2001. 11
- [63] MUHITTIN MUNGAN, YVES WEISSKOPF, AND MEHMET ERBUDAK. *Phys. Rev. B*, **76**:195443, Nov 2007. 11
- [64] JOHN R. ARTHUR. *Surface Science*, **500**(13):189 – 217, 2002. 11
- [65] N. METROPOLIS, A. W. ROSENBLUTH, M. N. ROSENBLUTH, A. H. TELLER, AND E. TELLER. *J. Chem. Phys.*, **21**:1087–1092, 1953. 12
- [66] S. KIRKPATRICK, C. D. GELATT JR., AND M. P. VECCHI. *Science*, **220**:671–680, 1983. 12, 25
- [67] V. ČERNÝ. *J. Optim. Theo. Appl.*, **45**:41–51, 1985. 12
- [68] E. L. LAWLER, J. K. LENSTRA, A. H. G. RINNOOY KAN, AND D. B. SHMOYS. Wiley Interscience, Chichester, UK, 1985. 12
- [69] D. L. APPEGATE, R. E. BIXBY, V. CHVÁTAL, AND W. J. COOK. Princeton University Press, Princeton, USA, 2006. 12
- [70] J. C. SCHÖN. *Ber. Bunsenges.*, **100**:1388–1391, 1996. 12, 13, 25
- [71] D. J. WALES, M. A. MILLER, AND T. R. WALSH. *Nature*, **394**:758–760, 1998. 12
- [72] P. SALAMON, P. SIBANI, AND R. FROST. SIAM Monographs on Mathematical Modeling and Computation. Society for Industrial and Applied Mathematics, Philadelphia, USA, 2002. 12

## REFERENCES

---

- [73] FLAVIA P. AGOSTINI, DIOGO DE O. SOARES-PINTO, MARCELO A. MORET, CARLA OSTHOFF, AND PEDRO G. PASCUTTI. *Journal of Computational Chemistry*, **27**(11):1142–1155, 2006. 12
- [74] L. DAVIS. Pitman, London, 1987. 12
- [75] D. E. GOLDBERG. Addison-Wesley Publishing Company, Reading. M.A., 1989. 12, 13
- [76] J. H. HOLLAND. Univ. Mich. Press, Ann Arbor, 1975. 12
- [77] R. L. JOHNSTON, editor. **110**. Springer Berlin Heidelberg, Berlin, Heidelberg, 2004. 13
- [78] R. L. JOHNSTON AND C. ROBERTS. pages 161–204. Springer-Verlag, Berlin, 2003. 13
- [79] D. J. WALES AND J. P. K. DOYE. *J. Phys. Chem.*, **101**:5111–5116, 1997. 13, 51
- [80] D. J. WALES AND T. V. BOGDAN. *J. Phys. Chem. B*, **110**:20765–20776, 2006. 13
- [81] D. J. WALES AND H. A. SCHERAGA. *Science*, **285**:1368–1372, 1999. 13
- [82] A. R. OGANOV, Y. MA, C. W. GLASS, AND M. VALLE. *Psi-k Newsletter*, **84**:142–171, 2007. 13
- [83] J. C. SCHÖ AND M. JANSEN. chapter 4, pages 67–106. Wiley VCh, Weinheim, 2011. 13
- [84] TIM N. HEINZ AND PHILIPPE H. HÜNENBERGER. *J. Comput. Chem.*, **25**(12):1474–1486, September 2004. 15, 27
- [85] D. WOLF, P. KEBLINSKI, S. R. PHILLPOT, AND J. EGGBRECHT. *The Journal of Chemical Physics*, **110**(17):8254–8282, 1999. 15, 26
- [86] J. A. POPLE AND R. K. NESBET. *The Journal of Chemical Physics*, **22**(3):571–572, 1954. 17
- [87] J. L. FRY, N. E. BRENER, AND R. K. BRUYERE. *Phys. Rev. B*, **16**:5225–5232, Dec 1977. 17
- [88] N. E. BRENER AND J. L. FRY. *Phys. Rev. B*, **17**:506–512, Jan 1978. 17
- [89] P.W. ATKINS. *Molecular quantum mechanics: an introduction to quantum chemistry*. Clarendon Press, 1970. 17
- [90] WIKIPEDIA, 2012. [Online; accessed 22-June-2012]. 17, 18
- [91] RICHARD M. MARTIN. Cambridge University Press, April 2004. 17, 19
- [92] P. HOHENBERG AND W. KOHN. *Phys. Rev. B*, **136**:864–871, 1964. 17

## REFERENCES

---

- [93] G. PETZOW, E. T. HENIG, U. KATTNER, AND H. L. LUKAS. *Z. Metallkd.*, **75**:3–10, 1984. 19
- [94] M. D. TOWLER, 1996. 19
- [95] R. DOVESI. **67** of *Lecture Notes in Chemistry*. Springer-Verlag, Berlin Heidelberg New York, 1996. 19
- [96] C. PISANI, editor. **67** of *Lecture Notes in Chemistry*. Springer-Verlag, Berlin Heidelberg New York, 1996. 19
- [97] R. DOVESI, B. CIVALLERI, R. ORLANDO, C. ROETI, AND V. R. SOUNDERS. **21** of *Reviews in Computational Chemistry*. Wiley-VCH, John Wiley & Sons, Inc., Weinheim, New York, 2005. 19
- [98] R. DOVESI, R. ORLANDO, B. CIVALLERI, C. ROETI, V. R. SOUNDERS, AND C. M. ZICOVICH-WILSON. *Z. Kristalogr.*, **220**:571–573, 2005. 19
- [99] M.D. TOWLER. European Summer School "Ab initio modeling in solid state chemistry", Torino, Italy, 2000. 19
- [100] R. DOVESI, V.R. SAUNDERS, C ROETTI, R. ORLANDO, C. M. ZICOVICH-WILSON, F. PASCALE, B. CIVALLERI, K. DOLL, N.M. HARRISON, I.J. BUSH, P. DARCO, AND M. LLUNELL. Univ. Torino, Torino, 2009. 19, 20, 27, 29, 62
- [101] <http://www.crystal.unito.it/>. 20
- [102] D. FISCHER AND M. JANSEN. *Z. Anorg. Allg. Chem.*, **629**:1934, 2003. 20
- [103] V. CZERNY. *J. Optim. Theo. Appl.*, **45**:41–51, 1985. 25
- [104] J. C. SCHÖN, H. PUTZ, AND M. JANSEN. *J. Phys.: Cond. Matt.*, **8**:143–156, 1996. 25, 50
- [105] R. HUNDT. KPLOTT: A Program for Plotting and Investigation of Crystal Structures, University of Bonn, Germany, Version 9, 2007, 1979. 26, 35
- [106] R. HUNDT, J. C. SCHÖN, S. NEELAMRAJU, J. ZAGORAC, AND M. JANSEN. *J. Appl. Cryst.*, 2012. Accepted. 26
- [107] R. HUNDT, J. C. SCHÖN, AND M. JANSEN. *J. Appl. Cryst.*, **39**:6–16, 2006. 26, 35
- [108] D. WALES. Cambridge University Press, Cambridge, UK, 1 edition, 2003. 26
- [109] TULLIO PILATI AND ALESSANDRA FORNI. *Journal of Applied Crystallography*, **33**(2):417, Apr 2000. 26
- [110] A. HANNEMANN, R. HUNDT, J. C. SCHÖN, AND M. JANSEN. *J. Appl. Cryst.*, **31**:922–928, 1998. 26
- [111] J. D. GALE. *J. Chem. Soc. Farad. Trans.*, **93**:629–637, 1997. 26

## REFERENCES

---

- [112] M CATTI, A PAVESE, R DOVESI, C ROETTI, AND M CAUSA. *Physical Review B*, **44**(8):3509–3517, AUG 15 1991. 26, 55
- [113] D. BACORISEN, ROGER SMITH, J.A. BALL, R.W. GRIMES, B.P. UBERUAGA, K.E. SICKAFUS, AND W.T. RANKIN. *Nuclear Instruments and Methods in Physics Research Section B: Beam Interactions with Materials and Atoms*, **250**(12):36 – 45, 2006. 26
- [114] W. A. HARRISON. W. H. Freeman and Co., San Francisco, 1980. 27
- [115] R. DOVESI, R. ORLANDO, B. CIVALLERI, C. ROETTI, V. R. SAUNDERS, AND C. M. ZICOVICH-WILSON. *Zeitschrift fur Kristallographie*, **220**(5-6):571–573, 2005. 27, 29, 62
- [116] L. VALENZANO, Y. NOEL, R. ORLANDO, AND C. M. ZICOVICH-WILSON. *Theoretical Chemistry Accounts*, **117**(5-6):991–1000, MAY 2007. 27, 29, 62
- [117] R NADA, CRA CATLOW, C PISANI, AND R ORLANDO. *Modelling and Simulation in Materials Science and Engineering*, **1**(2):165–187, JAN 1993. 27, 29, 62
- [118] M. KAUPP, P. V. R. SCHLEYER, H. STOLL, AND H. PREUSS. *The Journal of Chemical Physics*, **94**(2):1360–1366, 1991. 27
- [119] A. KULKARNI, K. DOLL, J. C. SCHON, AND M. JANSEN. *J. Phys. Chem. B*, **114**:15573–15581, 2010. 27
- [120] A. D. BECKE. *J. Chem. Phys.*, **98**:5648, 1993. 29, 62
- [121] XIAOSONG LI AND MICHAEL J. FRISCH. *Journal of Chemical Theory and Computation*, **2**(3):835–839, 2006. 29
- [122] VINCENT LIEGEOIS, KENNETH RUUD, AND BENOIT CHAMPAGNE. *The Journal of Chemical Physics*, **127**(20):204105, 2007. 29
- [123] F. PASCALE, C. M. ZICOVICH-WILSON, F. LPEZ GEJO, B. CIVALLERI, R. ORLANDO, AND R. DOVESI. *Journal of Computational Chemistry*, **25**(6):888–897, 2004. 30
- [124] ANDREAS BACH, DIETER FISCHER, XIAOKE MU, WILFRIED SIGLE, PETER A. VAN AKEN, AND MARTIN JANSEN. *Inorganic Chemistry*, **50**(4):1563–1569, 2011. 37
- [125] R. G. GORDON AND Y. S. KIM. *J. Chem. Phys.*, **56**:3122, 1976. 37
- [126] F. RAMONDO, L. BENCIVENNI, AND V. ROSSI. *Journal of Molecular Structure*, **193**:203 – 210, 1989. 37
- [127] M. SPOLITI, L. BENCIVENNI, F. RAMONDO, AND V. ROSSI. *Journal of Molecular Structure: THEOCHEM*, **315**:19 – 27, 1994. 37
- [128] D. J. WALES. Cambridge Univ. Press, 2004. 41

## REFERENCES

---

- [129] A. MÖBIUS, A. NEKLIODOV, A. DIAZ-SANCHEZ, K. H. HOFFMANN, A. FACHAT, AND M. SCHREIBER. *Phys. Rev. Lett.*, **79**:4297–4301, 1997. 51
- [130] A. MÖBIUS, K. H. HOFFMANN, AND J. C. SCHÖN. pages 215–219. International School of Solid State Physics, World Scientific Singapore, 2004. 51
- [131] D. M. DEAVEN AND K. M. HO. *Phys. Rev. Lett.*, **75**:288–291, 1995. 51
- [132] J.H. FERZIGER AND H.G. KAPER. North-Holland Pub. Co., 1972. 52
- [133] E. FRANCISCO, A. MARTIN PENDAS, AND M. A. BLANCO. *The Journal of Chemical Physics*, **123**(23):234305, 2005. 54
- [134] M. J. FRISCH, G. W. TRUCKS, H. B. SCHLEGEL, G. E. SCUSERIA, M. A. ROBB, J. R. CHEESEMAN, J. A. MONTGOMERY, JR., T. VREVEN, K. N. KUDIN, J. C. BURANT, J. M. MILLAM, S. S. IYENGAR, J. TOMASI, V. BARONE, B. MENNUCCI, M. COSSI, G. SCALMANI, N. REGA, G. A. PETERSSON, H. NAKATSUJI, M. HADA, M. EHARA, K. TOYOTA, R. FUKUDA, J. HASEGAWA, M. ISHIDA, T. NAKAJIMA, Y. HONDA, O. KITAO, H. NAKAI, M. KLENE, X. LI, J. E. KNOX, H. P. HRATCHIAN, J. B. CROSS, V. BAKKEN, C. ADAMO, J. JARAMILLO, R. GOMPERTS, R. E. STRATMANN, O. YAZYEV, A. J. AUSTIN, R. CAMMI, C. POMELLI, J. W. OCHTERSKI, P. Y. AYALA, K. MOROKUMA, G. A. VOTH, P. SALVADOR, J. J. DANNENBERG, V. G. ZAKRZEWSKI, S. DAPPRICH, A. D. DANIELS, M. C. STRAIN, O. FARKAS, D. K. MALICK, A. D. RABUCK, K. RAGHAVACHARI, J. B. FORESMAN, J. V. ORTIZ, Q. CUI, A. G. BABOUL, S. CLIFFORD, J. CIOSLOWSKI, B. B. STEFANOV, G. LIU, A. LIASHENKO, P. PISKORZ, I. KOMAROMI, R. L. MARTIN, D. J. FOX, T. KEITH, M. A. AL-LAHAM, C. Y. PENG, A. NANAYAKKARA, M. CHALLACOMBE, P. M. W. GILL, B. JOHNSON, W. CHEN, M. W. WONG, C. GONZALEZ, AND J. A. POPLE. Gaussian, Inc., Wallingford, CT, 2004. 62
- [135] D. E. MANN, G. V. CALDER, K. S. SESHADRI, DAVID WHITE, AND M. J. LINEVSKY. *The Journal of Chemical Physics*, **46**(3):1138–1143, 1967. 62, 65, 72
- [136] S. NEELAMRAJU, A. BACH, J. C. SCHON, D. FISCHER, AND M. JANSEN. *The Journal of Chemical Physics*, **137**(19):194319, 2012. 63
- [137] S. NEELAMRAJU, J. C. SCHON, K. DOLL, AND M. JANSEN. *Phys. Chem. Chem. Phys.*, **14**:1223–1234, 2012. 65
- [138] V. KASPAROV, YU. EZHOV, AND N. RAMBIDI. *Journal of Structural Chemistry*, **21**:154–157, 1980. 10.1007/BF00746871. 65
- [139] V.I. BAIKOV. *Optics and Spectroscopy*, pages 502–5, 1969. 65
- [140] RH HAUGE, JL MARGRAVE, AND AS KANAAN. *Journal of the Chemical Society Faraday Transactions II*, **71**:1082–1090, 1975. 65, 72
- [141] S. BLONSKI AND S.H. GAROFALINI. *Surface Science*, **295**(12):263 – 274, 1993. 75

## REFERENCES

---

- [142] C. VERDOZZI, D. R. JENNISON, P. A. SCHULTZ, AND M. P. SEARS. *Phys. Rev. Lett.*, **82**:799–802, Jan 1999. 75
- [143] J.A. KELBER, CHENGYU NIU, K. SHEPHERD, D.R. JENNISON, AND A. BOGICEVIC. *Surface Science*, **446**(12):76 – 88, 2000. 75
- [144] X.-Z. DING, X.-H. LIU, AND Y.-Z. HE. *Journal of Materials Science Letters*, **15**:1789–1791, 1996. 76
- [145] A.F. VASSILYEVA, R.I. EGLITIS, E.A. KOTOMIN, AND A.K. DAULETBKOVA. *Physica B: Condensed Matter*, **405**(8):2125 – 2127, 2010. 78
- [146] DAVID P. LIDE, editor. *CRC Handbook of Chemistry and Physics*. CRC PRESS, 81 edition, 2000. 81
- [147] U. MÜLLER. *Inorganic Structural Chemistry*. Inorganic Chemistry. John Wiley & Sons, 1993. 83
- [148] X. MU, S. NEELAMRAJU, SCHON. J. C., W. SIGLE, P. A. VAN AKEN, AND M. JANSEN. submitted, 2013. 85

## REFERENCES

---



**Part VII**

**Appendix**



# Appendix A

## Vibrational frequencies of neutral clusters

Structure	Frequency( $\text{cm}^{-1}$ )	Mode	IR intensity	Raman Intensity(scaled)
M1	148.0	PIU	136.2	0.0
	148.0	PIU	136.2	0.0
	549.0	SGG	0	0.0
	862.5	SGU	152.4	5.7
D1	53.2	B3U	32.0	0.0000
	102.4	B2U	58.7	0.0000
	131.0	B2G	0.0	0.1395
	151.2	B3G	0.0	0.3822
	254.0	AG	0.0	0.8445
	264.1	B3U	194.4	0.0000
	436.0	B3G	0.0	0.1865
	453.6	B1U	40.8	0.0000
	479.8	AG	0.0	4.4909
	491.8	B2U	225.6	0.0000
	761.4	B1U	347.8	0.0000
	784.3	AG	0.0	2.5668
D2	126.0	A'	5.3809	0.0475
	126.4	A''	4.9356	0.0467
	247.0	A''	23.3475	0.0649
	247.8	A'	23.8909	0.0640
	280.7	A'	83.3832	0.2660
	281.1	A''	84.3854	0.2664
	324.8	A'	12.2685	1.3123

## A. VIBRATIONAL FREQUENCIES OF NEUTRAL CLUSTERS

---

	390.3	A'	94.4795	0.6034
	564.8	A''	150.4727	0.7560
	566.5	A'	150.5218	0.7518
	605.0	A'	121.7408	8.0581
	743.1	A'	117.9504	0.4341
T1	41.5	A''	8.7898	0.0468
	74.5	A'	13.4606	0.2703
	88.6	A''	0.5391	0.0246
	116.4	A'	28.6598	0.0339
	121.5	A'	8.1677	0.0195
	127.6	A''	34.5196	0.0537
	186.2	A''	11.1164	0.0747
	221.8	A'	34.3575	0.3270
	277.7	A''	85.8194	0.1685
	292.4	A'	17.0860	0.5658
	300.1	A'	13.3136	0.0864
	312.3	A'	128.3836	1.3710
	334.2	A''	53.4468	0.0256
	372.7	A'	36.8189	0.4358
	449.1	A'	105.1304	1.7405
	470.4	A'	42.9653	2.2137
	501.3	A'	61.6946	0.2286
	546.1	A''	166.5212	0.2603
	649.8	A'	271.2572	0.7904
	746.8	A'	109.3279	0.7453
	772.4	A'	156.1625	1.7253
T2	43.5	B1	39.0506	0.0002
	47.8	A2	0.0000	0.0321
	50.0	B1	0.1347	0.0321
	90.4	A1	24.9874	0.2180
	91.2	B2	23.8209	0.2068
	136.4	B2	11.2876	0.1219
	138.2	B2	9.1610	0.1050
	140.0	A1	18.8608	0.2129
	176.0	B1	0.0406	0.1055
	176.8	A2	0.0000	0.1039
	241.4	A1	0.0000	0.3474
	259.0	B1	291.1725	0.0000
	320.0	A1	0.0031	2.9982
	407.2	A1	97.0486	0.0061

---

	407.3	B2	96.1379	0.0077
	571.4	A1	105.5569	0.0594
	572.1	B2	105.2027	0.0617
	580.5	B2	0.4946	0.0004
	762.0	B2	298.3694	0.7702
	762.0	A1	249.2707	1.4109
	764.0	A1	48.8832	4.0220
<hr/>				
T3	36.5	E	12.2875	0.0097
	36.5	E	12.2875	0.0097
	78.6	B1	0.0000	0.0256
	102.0	E	0.0189	0.1126
	102.0	E	0.0189	0.1126
	141.0	E	49.8869	0.0787
	141.0	E	49.8869	0.0787
	169.3	A1	0.0000	0.5406
	246.2	E	75.4518	0.1369
	246.2	E	75.4518	0.1369
	317.2	B2	4.6353	0.0756
	439.5	E	0.0385	0.1455
	439.5	E	0.0385	0.1455
	440.5	A1	0.0000	0.2323
	470.4	B2	35.8086	0.2656
	474.0	A1	0.0000	6.1841
	497.0	E	234.7357	0.0041
	497.0	E	234.7357	0.0041
	620.1	B2	315.1249	0.0835
	770.0	B2	285.5255	0.0427
	774.6	A1	0.0000	2.4080
<hr/>				
T4	60.8	A'	8.3647	0.1213
	86.9	A''	3.0095	0.0680
	93.2	A'	6.2821	0.1235
	126.9	A'	68.3523	0.2745
	127.5	A''	11.8183	0.0104
	171.3	A''	15.3715	0.0926
	189.7	A''	28.4894	0.1052
	190.7	A'	6.0682	0.0688
	237.7	A'	53.1411	0.2960
	297.6	A''	20.5940	0.3125
	299.3	A'	51.5793	0.2493
	314.0	A'	47.3980	0.8942

## A. VIBRATIONAL FREQUENCIES OF NEUTRAL CLUSTERS

---

	365.2	A''	0.0840	0.0270
	398.7	A'	126.0244	1.6972
	456.6	A'	149.5222	0.4994
	476.1	A''	39.6279	0.1266
	506.8	A'	156.9000	0.4303
	538.4	A'	75.5735	3.5392
	682.0	A''	199.1603	0.2940
	731.4	A''	203.1952	0.8707
	745.7	A'	87.3807	1.9166
<hr/>				
T5	54.0	A'	7.7371	0.0430
	124.4	A''	17.4140	0.1656
	130.0	A'	10.9628	0.0365
	183.4	A''	1.2842	0.0211
	210.7	A'	9.6254	0.1280
	231.7	A''	9.4204	0.1889
	251.1	A'	21.1302	0.3122
	267.6	A''	8.8632	0.0564
	289.0	A'	22.8508	0.5266
	328.2	A'	34.0474	0.1303
	337.2	A'	25.9769	0.7002
	339.8	A''	93.8939	0.0020
	368.7	A''	1.7879	0.2548
	424.5	A'	50.0123	1.2059
	438.5	A'	61.7045	0.2162
	464.4	A'	161.9525	2.0283
	466.9	A''	270.2487	0.0221
	536.2	A'	123.3064	4.8036
	550.9	A''	67.7196	0.0359
	597.2	A'	241.0170	0.3073
	713.5	A'	139.5334	1.4484
<hr/>				
T6	70.6	B1	2.9457	0.0204
	122.9	A1	0.8654	0.0303
	132.9	B2	10.8874	0.1416
	163.3	B1	1.3794	0.0079
	201.8	A2	0.0000	0.0463
	202.5	B2	119.6797	0.0028
	245.6	B1	49.1215	0.1138
	251.3	A1	14.0570	0.6545
	279.8	B2	5.1319	0.0737
	297.6	B2	31.5348	0.1975

---

	301.1	B1	42.3173	0.0728
	348.7	A1	18.2333	1.3034
	363.0	A2	0.0000	0.2513
	377.0	A1	26.6579	0.3523
	440.1	A1	71.7765	0.0458
	451.6	B1	260.2597	0.2996
	464.3	B2	250.8441	0.0268
	506.5	A1	28.6621	6.7414
	616.5	B2	78.7279	0.0826
	653.4	A1	227.1155	1.4360
	713.2	A1	128.0996	1.4198
T7	68.5	A''	7.6704	0.0619
	106.4	A'	0.5411	0.0424
	107.6	A''	1.9695	0.0341
	120.9	A'	39.2952	0.1707
	184.8	A''	8.1091	0.0289
	202.4	A'	55.9345	0.2128
	231.6	A''	22.4024	0.0201
	235.0	A''	16.4679	0.1990
	270.0	A'	1.3786	0.8320
	311.1	A'	46.0444	0.0600
	321.2	A'	17.9661	0.2486
	373.2	A''	31.6876	0.0231
	388.1	A'	7.3084	0.4483
	404.0	A'	184.7231	1.7208
	428.1	A'	84.6590	0.2994
	480.2	A''	41.5636	0.3104
	540.7	A'	128.7992	2.7961
	547.0	A''	271.0096	0.1716
	565.2	A'	58.1100	3.5233
	626.5	A'	194.5326	0.6894
	721.7	A'	151.1661	0.9241
T8	6.7	A''	0.7373	0.0153
	41.8	A'	0.5302	0.0066
	84.8	A''	1.4423	0.0030
	122.1	A'	30.0149	0.0538
	142.7	A''	41.8700	0.1617
	183.5	A''	3.0652	0.0447
	185.6	A'	2.5098	0.5236
	218.4	A'	12.2745	0.0273

## A. VIBRATIONAL FREQUENCIES OF NEUTRAL CLUSTERS

---

	255.2	A'	7.3137	0.1683
	267.6	A''	15.0231	0.1753
	299.9	A'	155.5214	0.1180
	369.4	A'	13.5348	0.1049
	381.6	A'	126.6344	0.6490
	413.4	A''	50.8211	0.1379
	486.7	A'	6.4779	3.3473
	503.0	A''	96.0985	0.0328
	542.9	A'	281.4334	0.8002
	567.0	A'	143.7221	0.6635
	579.9	A''	204.7646	0.5750
	620.3	A'	23.4273	7.0113
	768.0	A'	161.8410	0.6015
T9	-3.7	A''	0.4249	0.0040
	44.3	A''	0.7037	0.0059
	80.4	A'	1.0247	0.0041
	125.1	A''	29.6125	0.0440
	135.6	A'	43.7493	0.1682
	166.6	A'	5.5360	0.1196
	188.3	A'	0.1928	0.4757
	221.0	A''	11.9621	0.0131
	256.3	A''	4.9389	0.1598
	267.8	A'	14.6046	0.1672
	300.3	A''	159.5594	0.1156
	367.6	A'	8.3764	0.1209
	376.5	A'	134.3805	0.5687
	409.7	A'	52.7907	0.2039
	485.1	A'	12.7501	3.1954
	500.3	A'	96.4353	0.1865
	540.1	A'	273.0599	0.7736
	566.6	A''	152.9906	0.6274
	581.0	A'	186.1845	0.7722
	621.5	A'	30.6112	6.9002
	767.8	A'	161.0548	0.5871

---



# Appendix B

## Vibrational frequencies of global minima upto 10 units

Number of units	Frequency( $\text{cm}^{-1}$ )	Mode	IR intensity	Raman Intensity(scaled)
4	58.6	A1	6.7326	0.1837
	80.0	B2	20.8441	0.0731
	86.5	A2	0.0000	0.0364
	115.5	B1	34.5686	0.2769
	145.2	B1	13.1537	0.0203
	146.1	B2	0.0237	0.1120
	147.5	A1	1.9802	0.0001
	165.2	A2	0.0000	0.1332
	166.8	A1	12.5773	0.1362
	215.5	A2	0.0000	0.0988
	216.4	B2	145.0914	0.0025
	218.7	A1	6.0993	0.1693
	222.6	B1	62.9640	0.0869
	233.8	B2	0.0041	0.0561
	317.3	A1	4.0220	1.3079
	330.2	B2	30.3425	0.1141
	335.7	B1	33.2935	0.1800
	349.3	A1	58.1075	2.3089
	417.5	A1	132.3348	1.1394
	427.5	B2	14.2666	0.0421
	439.0	A2	0.0000	0.0075
	439.7	B1	93.2202	0.0352
	461.2	A1	1.5330	2.4764
	470.5	B1	33.5846	0.0002
	523.8	B1	329.7026	0.0583
	534.5	A1	144.7885	0.3543
	627.5	A2	0.0000	0.0224
	647.4	B2	407.1950	0.1736
	726.4	B2	71.5541	0.6949

## B. VIBRATIONAL FREQUENCIES OF GLOBAL MINIMA UPTO 10 UNITS

---

	734.9	A1	196.3153	2.4906
5	42.5	A'	16.2501	0.0169
	75.3	A'	3.0805	0.1565
	76.5	A''	12.2114	0.0063
	88.0	A''	8.3603	0.0259
	94.8	A'	7.3953	0.0173
	105.9	A'	8.5464	0.0940
	112.5	A''	1.1732	0.0912
	129.8	A''	8.8877	0.1293
	135.9	A'	18.5476	0.1466
	161.9	A''	0.6419	0.1026
	170.2	A'	7.9129	0.0987
	187.4	A'	42.1853	0.0538
	187.5	A''	32.9779	0.0191
	197.4	A'	1.0468	0.1846
	216.5	A'	61.7957	0.0906
	220.2	A''	15.3913	0.2248
	247.9	A'	54.2461	0.0263
	260.4	A''	50.5935	0.0595
	284.3	A''	31.4531	0.0841
	307.8	A'	30.8066	0.0727
	323.7	A'	8.0105	0.3201
	332.6	A'	27.9853	4.5423
	345.0	A''	81.1791	0.0092
	364.5	A'	10.0140	0.6831
	396.4	A'	29.0563	0.2085
	410.2	A''	29.1124	0.0198
	422.1	A'	3.6968	0.8813
	447.6	A'	118.1758	0.6275
	467.1	A'	94.4912	0.1251
	480.6	A''	20.7465	0.0773
	509.2	A''	252.8038	0.0013
	516.8	A''	3.4352	0.0100
	550.1	A'	203.5833	0.0710
	569.9	A''	206.2644	0.0618
	585.9	A'	104.4917	0.3169
	605.0	A''	24.2561	0.0005
	630.1	A'	400.1761	0.2634
	707.7	A'	331.2969	0.0167
	713.1	A'	5.0237	3.5877
6	22.8	A''	6.6111	0.0388
	58.8	A'	13.2458	0.0092
	79.6	A'	5.1512	0.0083
	82.3	A''	2.8915	0.0201
	88.7	A''	0.0336	0.0399
	99.1	A'	3.4155	0.0428
	104.5	A''	0.3359	0.0013

---

106.0	A'	8.7921	0.1830
117.3	A'	1.4871	0.2121
128.9	A'	13.8882	0.1493
129.1	A''	15.6826	0.0410
153.8	A''	4.8281	0.0871
160.1	A'	29.8695	0.0878
166.5	A''	0.4783	0.0201
188.2	A'	0.8744	0.0862
190.1	A''	0.1704	0.0471
195.9	A'	38.5085	0.0733
212.2	A''	53.9713	0.2148
213.0	A'	6.7457	0.0304
222.0	A'	15.8285	0.1417
225.5	A''	74.1638	0.1101
272.5	A''	8.3068	0.0481
278.8	A'	6.7363	1.6054
287.5	A''	27.4609	0.0224
291.2	A'	0.2408	0.0320
306.6	A'	30.1298	2.4951
328.5	A'	19.6677	0.4617
341.9	A'	2.4085	0.0332
353.5	A''	90.0244	0.0083
366.5	A'	222.8767	1.4521
385.1	A''	73.7103	0.0018
397.6	A'	15.7381	0.0557
415.2	A'	5.9872	0.0292
418.2	A''	126.4654	0.0408
442.3	A'	34.0089	0.9430
455.7	A'	9.2135	0.0898
495.5	A'	66.2716	0.1207
513.3	A''	197.6633	0.0074
529.2	A''	32.8299	0.0357
534.0	A'	3.7027	0.1637
554.9	A'	248.8994	0.8477
564.6	A''	122.2987	0.0520
604.4	A'	80.6193	0.2939
611.4	A'	195.9529	0.0440
611.4	A''	36.2122	0.0204
635.0	A'	531.7646	0.2197
702.2	A'	198.6839	1.4801
750.9	A'	173.6522	1.9915
7			
13.0	E	1.6422	0.0012
13.0	E	1.6422	0.0012
25.3	E	0.0738	0.0423
25.3	E	0.0738	0.0423
31.7	B	0.0000	0.0025
40.0	E	6.3874	0.0108

## B. VIBRATIONAL FREQUENCIES OF GLOBAL MINIMA UPTO 10 UNITS

---

40.0	E	6.3874	0.0108
55.2	A	0.0000	0.0000
72.9	A	0.0000	0.2377
73.9	E	0.0836	0.0271
73.9	E	0.0836	0.0271
77.0	B	0.0000	0.0075
94.4	A	0.0000	0.0000
100.7	E	14.6496	0.0051
100.7	E	14.6496	0.0051
105.5	B	0.0000	0.0921
125.3	E	0.2206	0.0254
125.3	E	0.2206	0.0254
138.5	E	32.5682	0.1966
138.5	E	32.5682	0.1966
144.0	B	0.1104	0.0001
211.1	A	0.0000	0.2312
216.6	E	62.4382	0.0202
216.6	E	62.4382	0.0202
235.4	E	9.6898	0.0052
235.4	E	9.6898	0.0052
250.5	E	48.4617	0.0797
250.5	E	48.4617	0.0797
272.2	B	1.2535	0.0056
324.7	A	0.0000	0.2009
363.9	B	2.2216	0.4695
423.2	A	0.0000	0.0851
436.2	E	0.5347	0.3960
436.2	E	0.5347	0.3960
437.5	E	0.9343	0.0437
437.5	E	0.9343	0.0437
439.6	B	8.0338	0.0963
440.0	E	0.0839	0.0034
440.0	E	0.0839	0.0034
451.8	A	0.0000	0.1017
458.4	B	6.5540	0.0287
461.6	A	0.0000	5.4063
473.7	B	34.2935	0.2104
473.8	A	0.0000	7.7781
486.4	E	20.9914	0.0016
486.4	E	20.9914	0.0016
496.8	E	2.2921	0.0008
496.8	E	2.2921	0.0008
508.6	E	635.6606	0.0004
508.6	E	635.6606	0.0004
581.9	B	1323.7050	0.0062
609.8	A	0.0000	0.0009
627.7	B	49.5150	0.0404

---

	636.1	A	0.0000	0.0000
	639.1	B	2.8465	0.4195
	771.1	B	274.9044	0.0420
	771.4	A	0.0000	2.3211
8	50.0	A”	0.3969	0.0067
	60.4	A’	2.4826	0.0235
	68.2	A”	6.2329	0.0543
	76.7	A’	8.5233	0.0327
	83.8	A”	6.5839	0.0144
	97.4	A’	1.4379	0.0840
	107.0	A”	0.0281	0.0056
	114.0	A’	0.7317	0.0544
	119.7	A”	3.0533	0.0258
	126.3	A”	0.0171	0.0524
	128.5	A’	7.5386	0.1412
	138.5	A’	3.3461	0.0592
	146.4	A’	0.9195	0.0551
	151.2	A”	4.0448	0.0033
	152.5	A”	13.2419	0.0597
	152.6	A’	35.0947	0.2060
	159.6	A’	16.0083	0.1476
	179.5	A’	26.8372	0.0667
	180.9	A”	4.5971	0.0199
	186.2	A’	28.9752	0.0098
	195.0	A”	22.7203	0.1290
	199.4	A”	10.2353	0.2049
	204.5	A’	1.1776	0.1286
	223.2	A’	42.7241	0.1662
	230.3	A”	10.7963	0.0038
	241.5	A”	17.7016	0.0303
	245.2	A’	53.4046	0.0804
	254.5	A”	5.3647	0.0185
	263.3	A’	11.6420	0.0145
	270.5	A”	18.7553	0.0058
	270.8	A’	37.9365	0.0190
	285.0	A’	16.0584	3.3535
	294.6	A”	0.4333	0.0191
	306.2	A’	6.0721	0.5679
	323.1	A’	0.7360	0.4020
	335.4	A’	9.0177	1.2675
	348.4	A’	67.1888	0.7186
	360.5	A’	53.0865	0.0208
	362.1	A”	62.2728	0.0467
	389.5	A’	114.1426	0.0487
	389.8	A”	85.0982	0.0616
	398.1	A’	114.4946	0.0093
	402.7	A”	126.7417	0.0006

## B. VIBRATIONAL FREQUENCIES OF GLOBAL MINIMA UPTO 10 UNITS

---

	404.0	A'	63.1571	0.7153
	435.2	A'	9.2814	0.0617
	436.5	A''	4.6381	0.0259
	453.7	A'	83.9177	1.4879
	458.8	A'	30.5904	0.2052
	463.8	A''	1.6080	0.0216
	469.0	A''	73.8072	0.0302
	472.3	A'	90.9997	0.5727
	498.1	A'	9.1417	0.0271
	501.8	A''	72.4480	0.0049
	507.1	A'	45.4412	0.0261
	526.1	A''	59.1465	0.0153
	543.0	A'	33.1433	0.0685
	553.0	A'	85.4608	0.1603
	560.1	A''	6.3038	0.0380
	562.6	A'	314.1408	0.0347
	586.0	A'	463.3548	0.1636
	589.0	A''	156.7928	0.0318
	601.7	A''	224.7759	0.0940
	646.9	A''	178.5020	0.0506
	653.1	A'	124.6271	0.0313
	676.2	A'	383.9245	0.1149
	715.8	A'	248.0084	1.5732
9	31.6	A	2.1665	0.0330
	43.6	A	3.6851	0.0168
	53.5	A	1.8765	0.0127
	66.5	A	9.0712	0.0578
	70.2	A	4.4174	0.0246
	78.4	A	3.9557	0.0688
	87.4	A	0.4800	0.0327
	94.5	A	1.4446	0.0626
	99.0	A	3.0160	0.1585
	105.4	A	2.8840	0.1288
	114.1	A	5.6767	0.0672
	120.2	A	7.6769	0.0438
	130.5	A	4.4267	0.1213
	138.6	A	3.0259	0.1578
	139.5	A	7.9405	0.2045
	146.2	A	7.2878	0.0218
	149.3	A	10.8678	0.1254
	157.4	A	23.3236	0.0511
	158.2	A	11.0660	0.2046
	164.9	A	12.1132	0.0378
	167.1	A	38.6998	0.1372
	187.9	A	14.3337	0.1028
	195.7	A	15.1703	0.0145
	200.3	A	3.3631	0.1070

---

206.3	A	13.2481	0.2055
209.5	A	41.3094	0.3295
229.3	A	11.4889	0.7214
229.9	A	24.3394	0.2577
241.3	A	19.5985	0.2835
253.4	A	79.3442	0.3822
260.1	A	12.3575	0.5912
265.5	A	114.3311	0.8078
273.7	A	69.9533	0.5728
279.5	A	23.8249	0.0713
285.2	A	35.4327	0.3174
298.0	A	14.2573	0.4424
312.1	A	13.3333	1.1343
323.8	A	15.6850	0.9982
324.4	A	12.3478	0.8149
341.8	A	3.0957	1.3903
347.6	A	61.3149	0.3217
362.6	A	47.6414	0.3607
371.6	A	57.3908	0.0292
377.7	A	149.6673	0.6454
382.3	A	52.5440	0.1011
403.7	A	126.9940	0.0859
406.2	A	153.3274	0.1925
408.9	A	288.4836	0.1569
424.0	A	22.3274	0.2346
435.0	A	47.4411	0.3684
445.8	A	17.1127	0.3432
453.5	A	19.1752	0.6970
466.4	A	33.7412	1.1303
468.5	A	11.5022	0.0980
482.2	A	0.4043	0.3111
492.3	A	79.0891	0.8056
501.5	A	18.8070	2.7075
508.7	A	12.2672	0.2576
525.9	A	95.2352	0.6121
530.2	A	20.5372	0.0524
531.9	A	88.7572	0.1731
557.7	A	90.2204	0.1036
570.4	A	38.5739	0.3955
572.6	A	106.4015	0.4427
610.0	A	61.5525	0.2056
630.2	A	38.6600	0.0505
633.7	A	101.2509	0.2263
643.6	A	177.7731	0.0521
648.9	A	97.6276	0.1820
659.2	A	64.6150	0.3252
664.3	A	244.9240	0.7080

## B. VIBRATIONAL FREQUENCIES OF GLOBAL MINIMA UPTO 10 UNITS

---

	669.6	A	522.1809	0.0489
	697.8	A	184.5098	0.0371
	713.6	A	241.1336	0.1190
	780.3	A	189.5966	0.6176
10	-48.5	A''	0.0000	0.0043
	22.5	A'	3.7658	0.0155
	33.0	A'	0.3349	0.0701
	61.7	A''	0.0004	0.0356
	79.1	A''	10.3786	0.0115
	81.6	A''	0.0001	0.0075
	97.2	A'	55.2013	0.0009
	113.0	A'	1.3493	0.0037
	120.8	A''	0.1574	0.0138
	129.1	A'	1.1633	0.0282
	135.8	A''	0.4063	0.0404
	138.5	A''	0.0000	0.0284
	143.3	A'	4.4763	0.0187
	145.9	A''	0.6501	0.0286
	149.3	A'	0.0551	0.0111
	158.8	A'	2.2289	0.1640
	165.3	A'	1.6075	0.0176
	175.9	A''	19.9424	0.0293
	177.1	A''	0.0011	0.0003
	180.6	A'	11.9819	0.0384
	194.0	A''	75.5174	0.0270
	194.1	A'	7.9757	0.1218
	194.6	A'	1.3862	0.0353
	197.9	A'	33.1184	0.0007
	204.7	A''	1.8705	0.0002
	217.1	A'	14.4901	0.0471
	218.1	A''	0.0000	0.0020
	220.1	A''	0.0011	0.0098
	229.1	A'	33.0239	0.1140
	236.8	A''	20.8729	0.0056
	253.7	A'	0.0009	0.0005
	254.4	A''	0.0004	0.0017
	260.2	A'	60.5301	0.5794
	267.7	A''	35.2671	0.0048
	284.6	A'	0.3185	0.7454
	287.4	A'	136.4049	0.0001
	304.2	A'	31.2394	0.0004
	306.8	A''	167.8007	0.0026
	323.4	A'	4.2092	0.0489
	331.1	A''	0.0000	0.0262
	331.2	A'	74.3278	0.0110
	339.0	A''	2.4741	0.0021
	347.7	A'	84.8624	0.0118



---

356.2	A”	6.3529	0.0170
365.8	A’	13.7869	0.0676
367.0	A”	8.2219	0.0469
370.3	A’	152.5974	0.0549
374.0	A”	0.0005	0.0691
383.4	A’	236.1554	0.0111
408.4	A’	16.8096	0.0122
409.9	A’	91.6895	0.8100
431.2	A”	372.0890	0.0040
434.1	A”	0.0680	0.0329
443.5	A’	45.5549	0.0254
444.8	A’	196.5176	0.0789
453.4	A”	13.0024	0.0514
463.4	A’	28.5946	0.0065
464.6	A’	52.8870	0.1171
472.9	A”	0.0011	0.0312
475.9	A’	38.7383	1.9089
490.9	A’	20.3717	0.0019
500.4	A”	96.4716	0.0257
520.9	A”	0.0000	0.0008
530.7	A”	1.0359	0.1444
539.3	A’	42.9993	0.0527
544.6	A’	368.9668	0.0132
556.9	A”	0.0003	0.0113
567.9	A’	1.2616	0.1774
570.7	A’	64.2559	0.0055
580.5	A’	13.2129	0.1024
588.9	A”	173.2279	0.0010
589.6	A”	0.3764	0.0000
596.0	A”	20.3506	0.0344
603.5	A’	0.4926	0.0015
614.7	A’	67.8846	0.0378
623.3	A’	4.2561	0.0607
627.0	A”	0.0141	0.0002
633.2	A”	0.0021	0.0184
639.4	A’	230.0861	0.0715
640.4	A”	104.1140	0.0424
640.7	A’	424.0081	0.0873
666.6	A’	504.0917	0.2095 43
667.3	A”	806.9889	0.0083
686.6	A’	479.0277	0.0028

---

## B. VIBRATIONAL FREQUENCIES OF GLOBAL MINIMA UPTO 10 UNITS

---

# Appendix C

## Vibrational frequencies of ionic clusters

c Structure	Frequency( $\text{cm}^{-1}$ )	Mode	IR intensity	Raman Intensity(scaled)
MC1	679.8018	SG	78.8403	7.4925
MA1	-110.5	E'	0.4104	23.2675
	-110.5	E'	0.4102	23.2869
	73.5	A2''	111.4239	0.0000
	516.2	A1'	0.0000	106.6192
	667.8	E'	45.3380	45.4110
DC1	265.0	B1	23.6325	0.2687
	266.0	A1	23.9081	0.2758
	276.7	B2	443.7219	0.0365
	327.2	B2	0.2685	15.9612
	329.2	A2	0.0000	15.7746
	400.0	A1	0.0001	109.2487
	474.4	A1	98.2860	0.6070
	475.2	B1	98.3594	0.6141
	549.8	A1	0.0010	2.8787
DC2	84.9	B1	14.0533	1.4872
	133.9	B2	27.8667	0.0727
	219.2	B1	69.2485	11.3888
	281.2	A1	0.0001	0.6758
	396.1	B2	34.0819	2.3021
	467.3	A1	93.6508	75.5593
	475.8	A1	27.2367	2.5574
	483.1	B2	98.1352	0.2187
	766.3	A1	182.1028	1.4581
DC3	-138.5	PIU	1.0810	0.0000
	-138.5	PIU	1.0810	0.0000
	-57.5	PIG	0.0000	1009.9197
	-57.5	PIG	0.0000	1009.9200
	25.9	PIU	18.0044	0.0000

### C. VIBRATIONAL FREQUENCIES OF IONIC CLUSTERS

---

	25.9	PIU	18.0044	0.0000
	248.3	SGG	0.0000	129.2307
	460.1	SGU	397.1577	0.0000
	743.1	SGG	0.0000	73.8618
	755.5	SGU	84.0479	0.0000
DA1	66.2	B1	30.7103	0.0290
	93.4	A1	47.7257	3.1752
	125.3	A2	0.0000	1.5100
	138.2	B2	0.5991	0.2692
	176.0	A2	0.0000	3.3518
	204.4	B1	80.9822	0.5421
	239.7	A1	0.2578	156.6837
	259.3	B1	18.5432	3.7675
	276.1	B2	22.1043	31.4769
	308.9	A1	74.9180	2820.3390
	454.6	B2	16.1697	4.1155
	481.3	A1	44.7666	2049.5416
	484.4	A1	83.7108	592.4673
	749.9	B2	259.3744	281.7580
	773.0	A1	5.7531	3020.0861
DA2	43.6	B2	30.7103	1.6095
	45.2	A2	47.7257	3.9971
	93.6	B1	0.0000	0.0061
	119.8	B2	0.5991	0.9180
	146.2	B1	0.0000	0.2391
	214.5	A1	80.9822	1.3424
	249.0	B2	0.2578	1.1012
	338.9	A1	18.5432	21.3338
	416.4	B2	22.1043	5.0196
	439.4	B1	74.9180	0.1546
	446.6	A1	16.1697	11.7881
	476.4	A1	44.7666	6.8373
	494.3	B1	83.7108	0.0054
	666.3	A1	259.3744	6.1669
	773.8	A1	5.7531	1.4591
DA3	-36.6	A	0.0000	50.6544
	-8.6	A	6.9357	24.5911
	9.7	A	8.9434	28.1201
	88.1	A	2.7941	19.1799
	91.9	A	0.0001	58.7104
	110.7	A	33.0797	2.0066
	119.0	A	32.4177	0.0871
	218.0	A	59.3988	1.9739
	219.8	A	84.9449	3.4491
	310.2	A	0.0000	139.3342
	501.7	A	44.7279	63.6140
	597.5	A	0.0056	161.5212

---

	602.9	A	60.0225	135.8909
	603.5	A	72.1319	113.5497
	699.4	A	55.2994	4.5919
TC1	136.8	B2	418.3581	1340.4660
	148.6	A1	416.9516	1300.8257
	186.2	B1	0.0712	315.1066
	186.4	A2	0.0000	313.2535
	232.1	B1	17.1611	0.4381
	250.0	B2	3.8741	112.7729
	251.6	A1	3.4423	111.2257
	323.8	A2	0.0000	17.3689
	326.8	B1	0.0009	15.0988
	343.9	A1	0.0350	0.6957
	352.1	B2	42.2601	5.3177
	353.9	A1	45.5417	7.6014
	402.0	B1	117.6992	0.0269
	405.8	B2	0.0702	0.1302
	438.6	A1	0.0608	424.6644
	474.1	A1	0.0016	9.0957
	517.2	A1	27.0627	23.7837
	518.2	B2	27.3886	23.7634
TC2	35.3	B1	2.5610	0.0354
	89.5	B2	85.8832	49.7256
	120.2	B2	6.4857	20.9734
	133.1	B1	17.0968	0.0595
	134.2	A1	15.2675	11.5524
	144.4	A2	0.0000	193.9584
	225.5	B1	65.3621	8.8713
	251.0	A1	2.0804	39.6663
	337.3	A1	9.8357	130.3101
	348.4	B2	411.2856	0.9958
	378.0	A1	15.6952	79.9564
	402.7	A2	0.0000	5.2578
	455.8	B2	10.5427	103.9680
	469.2	B1	100.8959	1.0866
	507.9	A1	3.8291	51.5220
	535.9	B2	17.3467	4.6889
	546.1	A1	115.4438	223.9297
	744.4	A1	199.6938	38.9575
TC3	-65.6	A''	22.4451	2006.6145
	-63.7	A'	22.4625	1988.5870
	21.2	A'	3.9328	140.9161
	22.1	A''	4.0115	131.9974
	117.6	A'	1.8760	531.2836
	118.5	A''	1.9823	521.0164
	186.2	A'	27.3257	299.2814
	271.5	A'	25.2831	9.7127

### C. VIBRATIONAL FREQUENCIES OF IONIC CLUSTERS

---

	273.1	A''	25.3136	10.7137
	313.3	A''	8.5750	26.1795
	315.2	A'	9.6294	25.5272
	374.8	A'	627.7478	264.3189
	415.6	A'	6.0065	91.7594
	485.7	A'	101.1238	12.5041
	486.3	A''	101.2806	12.8220
	510.9	A'	172.0292	86.5508
	627.1	A'	162.7790	34.0599
	787.3	A'	99.1198	102.2815
TC4	43.3	A2	0.0000	1.0345
	48.3	B1	19.6957	0.0511
	84.2	B1	2.1914	6.5110
	92.4	A1	23.0557	0.3756
	117.4	B2	0.0159	0.0292
	134.8	B2	20.9378	1.9946
	142.6	A1	25.1177	6.4170
	175.5	A2	0.0000	0.8324
	233.6	B1	153.8661	10.2567
	245.6	A1	0.6078	10.5717
	324.9	A1	13.5231	2.0198
	372.6	B2	50.4493	1.0809
	420.7	A1	41.9334	18.9884
	537.4	B2	38.7141	1.9434
	572.5	A1	208.0347	175.5988
	575.9	B2	21.9942	2.2376
	753.1	B2	295.5469	0.0671
	754.1	A1	127.6767	1.5852
TC5	43.1	B1	6.1630	0.0005
	56.3	B2	3.6148	0.5222
	79.1	A2	0.0000	0.2548
	119.2	B1	13.0668	0.1978
	128.3	B2	30.4411	0.2997
	184.3	A1	0.0098	0.7767
	199.2	B2	2.0201	9.3436
	244.0	B1	87.8513	0.1342
	330.5	A1	5.0068	2.3423
	395.7	B1	36.0350	2.3027
	434.7	B2	6.9203	0.0352
	444.8	A1	8.5735	10.0123
	470.1	A1	139.3128	46.9441
	475.2	A1	2.7020	4.1350
	486.3	B1	105.4313	0.3681
	495.8	B2	184.4568	1.4756
	620.2	A1	269.1153	11.0571
	770.7	A1	153.3829	3.6310

---

---

TC6	-147.1	B1	1.5970	33.5646
	-127.2	B2	0.0688	443.7031
	-43.3	B1	2.6646	929.8834
	19.3	B1	9.8371	8.0977
	20.5	B2	8.3125	20.3830
	48.1	B2	0.8270	251.5355
	79.3	B1	12.3282	220.8117
	132.8	B2	26.1824	11.9392
	169.6	A1	0.0005	16.4449
	210.0	B1	51.3572	816.7051
	317.9	A1	5.5779	35.8832
	421.8	A1	482.7756	102.4106
	427.8	B2	0.0382	3.6374
	462.6	A1	23.5302	758.2066
	479.7	B2	118.1511	96.6718
	624.8	A1	0.1169	1944.2514
	734.1	A1	74.0768	13.6941
	765.9	A1	277.6935	7.1181
<hr/>				
TA1	65.8	A'	2.7291	54.3360
	66.5	A''	1.4227	57.1131
	70.8	A'	15.9000	29.3380
	104.3	A'	13.3146	14.9332
	107.2	A''	11.7427	15.8007
	124.9	A''	0.0793	0.0112
	151.2	A'	0.0410	22.2048
	152.3	A''	0.0000	23.9270
	209.1	A'	32.9098	0.2053
	236.9	A	0.2441	6.4803
	237.0	A	0.2684	6.6628
	274.2	A'	0.2956	111.9139
	331.2	A''	3.5376	0.8244
	331.7	A'	3.3610	0.5288
	405.2	A'	167.0294	1.5353
	433.1	A'	4.7581	24.1506
	433.7	A''	4.5155	24.3821
	452.4	A'	80.3742	22.3108
	504.4	A''	0.0606	0.0145
	521.1	A''	5.8534	0.5073
523.2	A'	6.0774	0.6037	
562.3	A'	271.1470	27.6516	
563.4	A''	267.7650	25.0229	
655.6	A'	42.1063	129.6275	
<hr/>				
TA2	32.6891	B1	5.2962	8.8640
	62.9291	A1	2.2538	68.4745
	72.4416	A2	0.0000	24.0930
	80.7613	A	10.5665	24.9851
	81.2377	A	9.3551	63.0562

### C. VIBRATIONAL FREQUENCIES OF IONIC CLUSTERS

---

	125.7098	B2	5.9407	0.0067
	134.2234	B1	12.6166	4.0781
	137.3993	A1	2.5274	23.9647
	139.5365	B2	0.9630	24.4449
	183.3292	A2	0.0000	2.8121
	236.1175	B1	94.5877	0.4807
	257.0320	A1	2.2848	153.2806
	275.1156	A1	9.1626	10.4140
	388.6284	B2	4.9504	35.4235
	393.2017	A1	9.2182	15.6255
	413.0533	A2	0.0000	2.2115
	458.7100	A1	4.5387	45.7923
	475.7693	B1	184.1895	82.3009
	483.7675	B2	26.8532	5.2151
	501.2036	B2	236.5422	25.4715
	547.2299	A1	0.5302	20.3724
	563.1630	B2	0.5912	0.8336
	584.4562	A1	140.5754	280.8352
	699.8364	A1	56.6756	588.3195
TA3	32.6	B1	5.2962	8.8640
	62.9	A1	2.2538	68.4745
	72.4	A2	0.0000	24.0930
	80.7	A	10.5665	24.9851
	81.2	A	9.3551	63.0562
	125.7	B2	5.9407	0.0067
	134.2	B1	12.6166	4.0781
	137.3	A1	2.5274	23.9647
	139.5	B2	0.9630	24.4449
	183.3	A2	0.0000	2.8121
	236.1	B1	94.5877	0.4807
	257.0	A1	2.2848	153.2806
	275.1	A1	9.1626	10.4140
	388.6	B2	4.9504	35.4235
	393.2	A1	9.2182	15.6255
	413.0	A2	0.0000	2.2115
	458.7	A1	4.5387	45.7923
	475.7	B1	184.1895	82.3009
	483.7	B2	26.8532	5.2151
	501.2	B2	236.5422	25.4715
	547.2	A1	0.5302	20.3724
	563.1	B2	0.5912	0.8336
	584.4	A1	140.5754	280.8352
	699.8	A1	56.6756	588.3195
TA4	12.5	A''	1.7977	5.5767
	40.3	A''	2.8885	0.9890
	68.8	A'	11.6210	0.1872
	86.8	A''	1.6003	1.0151



---

	110.9	A'	21.3890	0.0090
	120.5	A''	21.1982	0.8472
	122.1	A'	5.1785	0.0240
	177.8	A''	1.3047	0.7086
	199.0	A'	13.0500	0.7111
	272.3	A''	53.2860	0.1235
	281.5	A'	91.6820	1.8757
	297.3	A'	7.4699	0.3194
	304.8	A'	66.1771	1.6772
	337.2	A''	44.7641	0.0452
	349.6	A'	30.1508	19.8825
	376.3	A'	32.6328	2.4455
	418.8	A''	0.7280	5.3665
	446.2	A'	77.8804	10.8052
	469.7	A'	52.6552	2.1178
	493.9	A'	63.2596	1.2578
	542.8	A''	156.4184	0.2418
	647.9	A'	335.6601	0.4185
	665.7	A'	98.6323	7.5735
	748.6	A'	109.5739	0.8327
TA5	-41.6	A	0.0063	5.0569
	5.2	A	5.9848	0.3500
	10.9	A	6.1814	0.3509
	69.8	A	5.9941	1.7392
	78.6	A	15.8592	0.0601
	124.8	A	30.3762	0.8079
	127.0	A	48.7007	0.0592
	156.3	A	2.0944	0.6806
	173.5	A	9.5987	0.3072
	177.6	A	26.9464	0.0157
	273.6	A	0.1309	0.1491
	275.0	A	0.1137	0.1606
	287.6	A	107.9823	0.0776
	288.4	A	102.7952	0.0838
	308.6	A	8.7147	21.1351
	342.8	A	46.9987	4.2953
	420.2	A	44.9250	8.4157
	446.1	A	0.0220	5.6037
	524.2	A	7.5888	7.3737
	525.0	A	166.0017	0.3495
	526.0	A	160.0976	0.3430
	627.0	A	173.2496	7.6490
	733.2	A	191.5725	0.8000
	768.1	A	173.3371	3.0487
TA6	-35.9	A	20.6585	0.0022
	11.9	A	10.8582	0.0577
	17.9	A	4.1098	0.6184

### C. VIBRATIONAL FREQUENCIES OF IONIC CLUSTERS

---

	37.3	A	0.0000	3.8214
	90.6	A	8.9953	0.3131
	99.2	A	0.0000	0.3554
	101.7	A	31.7922	0.0866
	109.9	A	32.2447	2.3678
	161.9	A	0.1541	0.8686
	244.3	A	49.1700	0.3963
	249.8	A	78.2769	0.2398
	286.2	A	0.0154	4.9424
	357.0	A	11.6742	12.0868
	437.9	A	0.1207	4.3856
	451.4	A	0.3652	4.1157
	469.2	A	1.9053	0.0733
	469.8	A	4.1172	0.0843
	471.4	A	16.1329	6.6153
	478.8	A	9.7693	7.8714
	500.4	A	211.7009	0.0357
	500.7	A	189.4414	0.0020
	665.6	A	310.8828	0.0744
	710.7	A	50.9102	2.6078
	801.6	A	82.6512	1.7868
TA7	24.8163	A	3.6058	4.7312
	44.7923	A	1.7470	1.2527
	63.8069	A	7.7771	0.2979
	85.5801	A	4.2907	0.8387
	106.3863	A	26.8274	0.0481
	110.9924	A	19.0923	1.0727
	137.6858	A	21.7089	0.1571
	179.5617	A	5.5833	0.6016
	204.9413	A	15.9547	0.9810
	286.2145	A	70.7604	1.9999
	291.9682	A	73.5866	0.1123
	305.4118	A	64.5502	1.1214
	316.3778	A	10.5353	2.6929
	359.4924	A	47.9684	0.0059
	365.9997	A	27.2618	15.6892
	391.9323	A	59.5050	0.3730
	441.4299	A	0.1770	4.5188
	459.8353	A	54.2472	9.8446
	494.5301	A	52.6490	1.5836
	533.2184	A	61.0202	1.1216
	557.3734	A	126.0952	0.5200
	678.1435	A	174.3689	1.8802
	708.6247	A	137.2994	3.0937
	780.0202	A	73.8730	0.8888

---

# Appendix D

## Vibrational modes for all the periodic structures studied

Structure	Frequency( $\text{cm}^{-1}$ )	Mode	IR active(I/A)	Raman active (I/A)	IR intensity(Km/mol)
Rutile (6a)	-3.1407	EU	A	I	0.04
	0.0000	A2U	A	I	0.00
	119.2986	B1G	I	A	0.00
	268.1421	B1U	I	I	0.00
	280.4701	EU	A	I	416.98
	291.5282	EG	I	A	0.00
	336.7311	A2G	I	I	0.00
	395.5091	EU	A	I	26.46
	397.2123	A2U	A	I	554.31
	400.8502	B1U	I	I	0.00
	411.7179	A1G	I	A	0.00
	440.2274	EU	A	I	605.64
	515.9486	B2G	I	A	0.00
Anatase (6b)	-3.2360	A2U	A	I	0.05
	-0.0683	EU	A	I	0.00
	159.5062	EG	I	A	0.00
	279.8888	EG	I	A	0.00
	283.7683	EU	A	I	257.93
	304.3807	B2U	I	I	0.00
	321.9659	A1G	I	A	0.00
	338.3952	A2U	A	I	536.38
	377.0052	B1G	I	A	0.00
	451.3006	B1G	I	A	0.00
	473.5365	EU	A	I	774.56
532.1146	EG	I	A	0.00	
CaCl <sub>2</sub> (6c)	152.8	B2U	I	A	0.00
	159.9	B3U	I	I	0.00
	259.2	B1U	A	I	204.44
	268.2	AG	I	A	0.00

## D. VIBRATIONAL MODES FOR ALL THE PERIODIC STRUCTURES STUDIED

---

	277.0	AU	I	A	0.00
	284.8	B3U	A	I	120.54
	347.1	B3G	I	A	0.00
	353.1	B2G	A	I	254.83
	374.8	B2U	A	I	542.77
	382.1	B1G	A	I	316.06
	384.3	B3U	I	A	0.00
	411.2	B1U	I	I	0.00
	459.6	B2U	A	I	79.27
	471.5	AG	A	I	90.57
	488.0	AU	I	A	0.00
CdI <sub>2</sub>	334.3	EG	I	A	0.00
(6d)	389.7	EU	A	I	562.00
	403.8	A2U	A	I	187.22
	413.0	A1G	I	A	0.00
5-fold	-6.0	BU	A	I	0.00
(5a)	-3.1	BU	A	I	0.00
	-0.0	AU	A	I	0.00
	14.7	AG	I	A	0.00
	55.6	AG	I	A	0.00
	68.2	BU	A	I	3.03
	108.6	AU	A	I	0.00
	138.3	AG	I	A	0.00
	158.8	BG	I	A	0.00
	162.7	AG	I	A	0.00
	170.8	BG	I	A	0.00
	192.8	BU	A	I	65.40
	201.7	BU	A	I	0.84
	207.5	AG	I	A	0.00
	216.4	BU	A	I	0.05
	217.9	AU	A	I	301.25
	264.5	BG	I	A	0.00
	286.3	BG	I	A	0.00
	328.4	BU	A	I	270.08
	338.8	AG	I	A	0.00
	376.7	AG	I	A	0.00
	380.5	BU	A	I	617.23
	403.7	AG	I	A	0.00
	432.4	AG	I	A	0.00
	447.3	AU	A	I	0.01
	449.5	AU	A	I	747.16
	456.9	AG	I	A	0.00
	490.0	BU	A	I	0.01
	519.8	BU	A	I	0.01
	532.6	BG	I	A	0.00
	533.7	BG	I	A	0.00
	614.3	BU	A	I	294.79

---

	655.8	AG	I	A	0.00
	659.0	BU	A	I	643.41
	674.6	AG	I	A	0.00
6e	-2.4	A1	A	A	0.02
	-0.9	B1	A	A	0.00
	-0.1	B2	A	A	0.00
	119.8	A2	I	A	0.00
	161.5	A1	A	A	2.24
	238.6	A2	I	A	0.00
	248.0	B1	A	A	27.81
	265.2	B2	A	A	12.45
	272.2	A1	A	A	70.86
	290.4	A1	A	A	338.34
	299.2	B1	A	A	283.08
	353.2	B2	A	A	537.45
	355.7	A2	I	A	0.00
	417.6	B1	A	A	121.56
	421.9	A1	A	A	104.61
	464.5	A1	A	A	21.46
	475.8	B1	A	A	100.38
	522.4	B1	A	A	13.02
NaCl	-0.2	EU	A	I	0.00
(6c)	-0.1	AU	A	I	0.00
	119.1	EU	A	I	424.29
	275.7	EU	A	I	117.98
	349.9	AU	A	I	65.00
	705.2	AU	A	I	202.70

---

## D. VIBRATIONAL MODES FOR ALL THE PERIODIC STRUCTURES STUDIED

---

# Appendix E

## Raman intensities for global minima of $(\text{MgF}_2)_n$ clusters

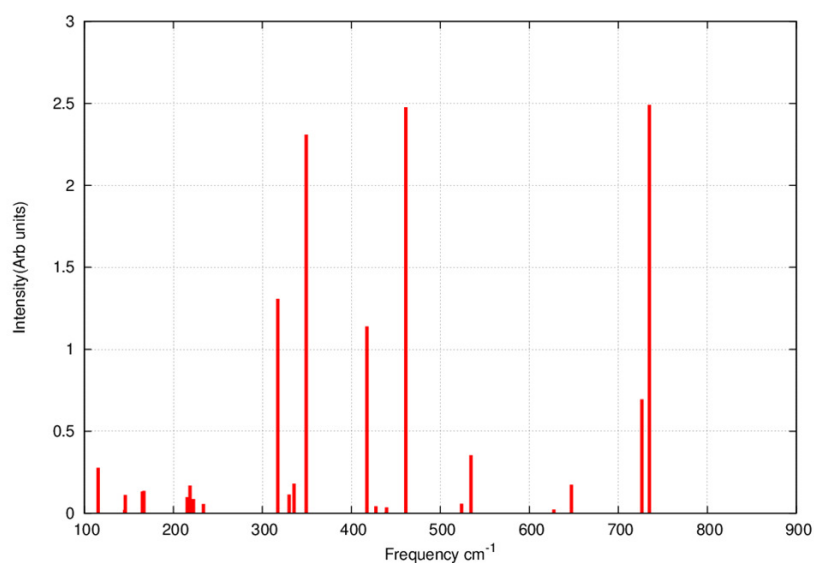


**Figure E.1:** Raman frequencies and intensities for global minimum of  $(\text{MgF}_2)_4$  at the B3LYP/6311++G\*\* level

## E. RAMAN INTENSITIES FOR GLOBAL MINIMA OF $(\text{MgF}_2)_N$ CLUSTERS

---

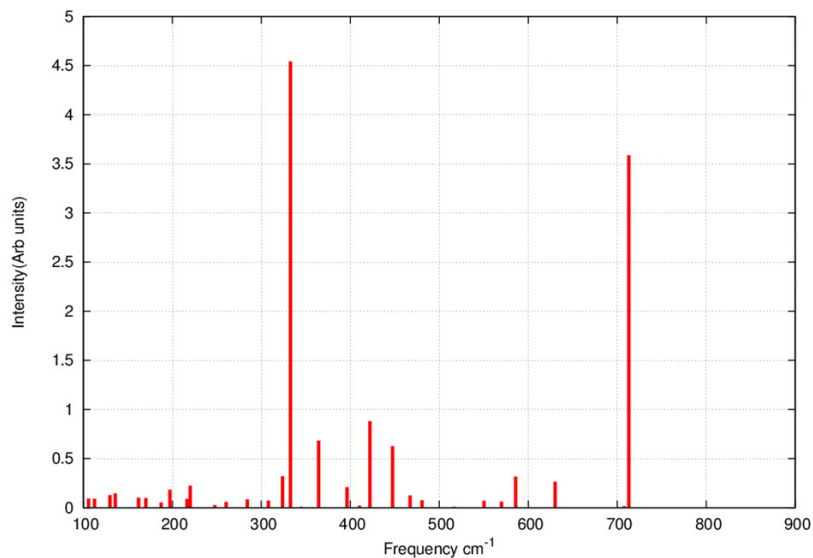


**Figure E.2:** Raman frequencies and intensities for global minimum of  $(\text{MgF}_2)_5$  at the B3LYP/6311++G\*\* level

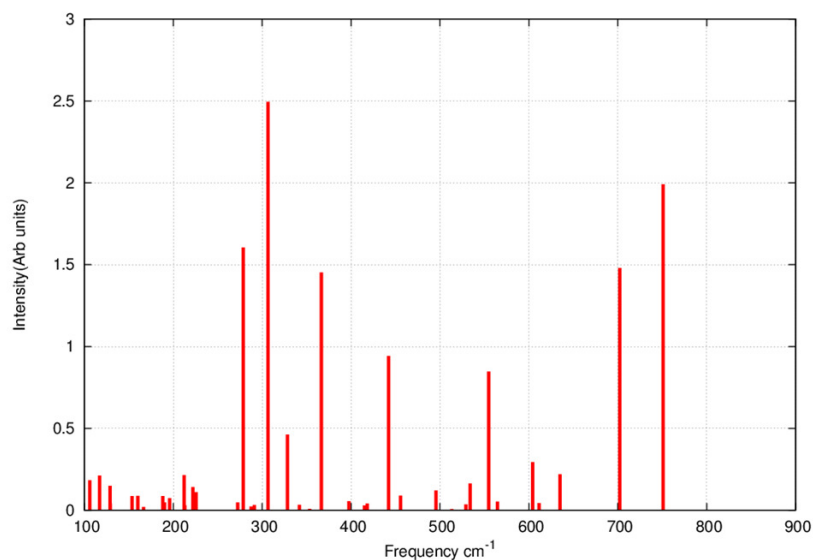


**Figure E.3:** Raman frequencies and intensities for global minimum of  $(\text{MgF}_2)_6$  at the B3LYP/6311++G\*\* level



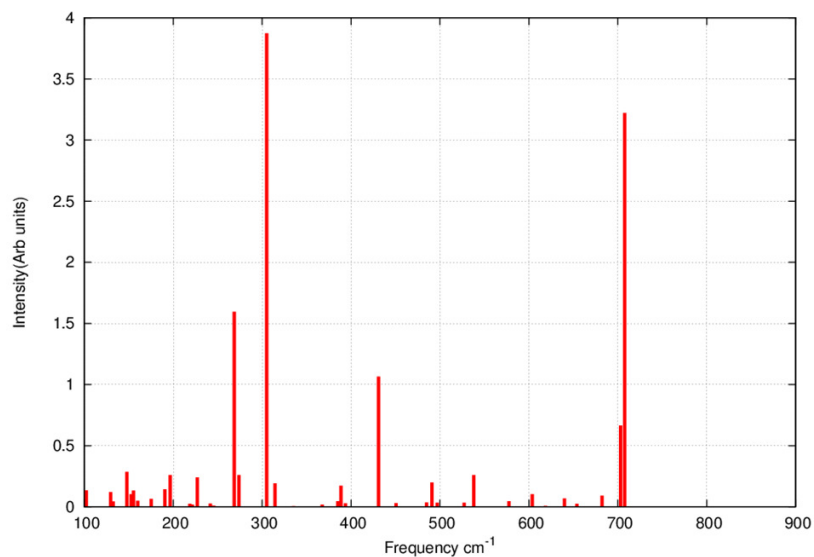


**Figure E.4:** Raman frequencies and intensities for global minimum of  $(\text{MgF}_2)_7$  at the B3LYP/6311++G\*\* level

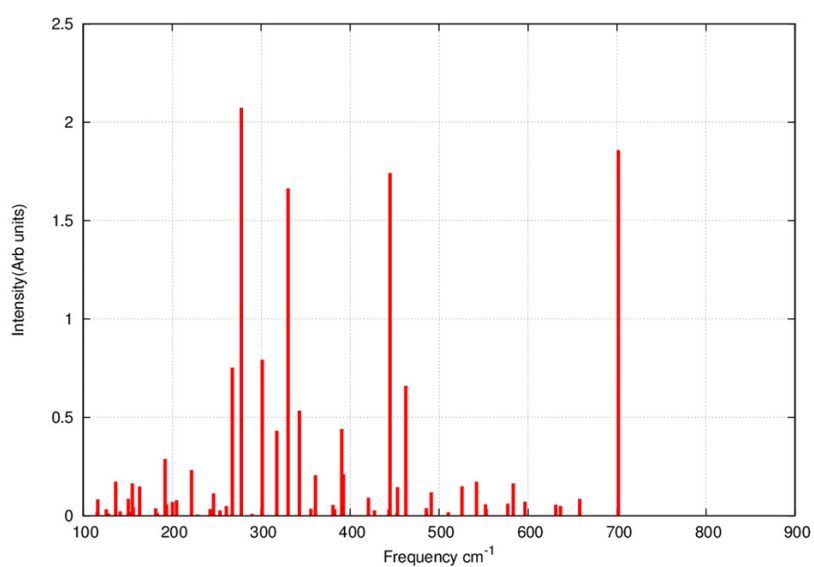


**Figure E.5:** Raman frequencies and intensities for global minimum of  $(\text{MgF}_2)_8$  at the B3LYP/6311++G\*\* level

## E. RAMAN INTENSITIES FOR GLOBAL MINIMA OF $(\text{MgF}_2)_N$ CLUSTERS

---

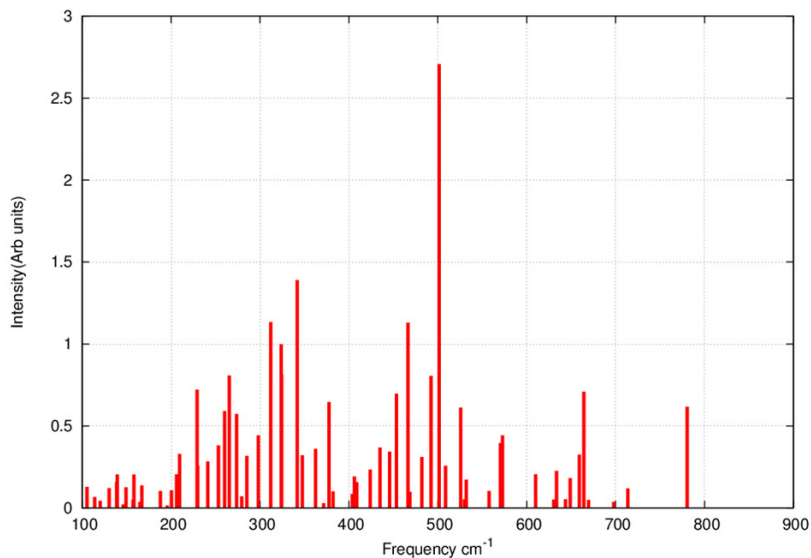


**Figure E.6:** Raman frequencies and intensities for global minimum of  $(\text{MgF}_2)_9$  at the B3LYP/6311++G\*\* level

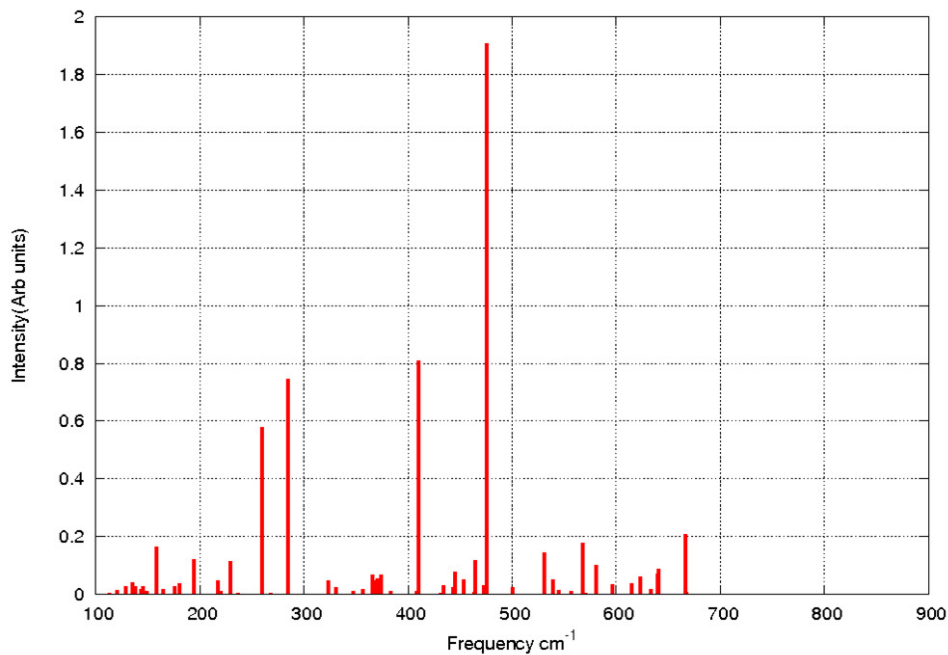


**Figure E.7:** Raman frequencies and intensities for global minimum of  $(\text{MgF}_2)_{10}$  at the B3LYP/6311++G\*\* level

## Appendix F

# Raman active modes observed in rutile structures

The four Raman active modes found in the Rutile structure are shown in Figure F.1

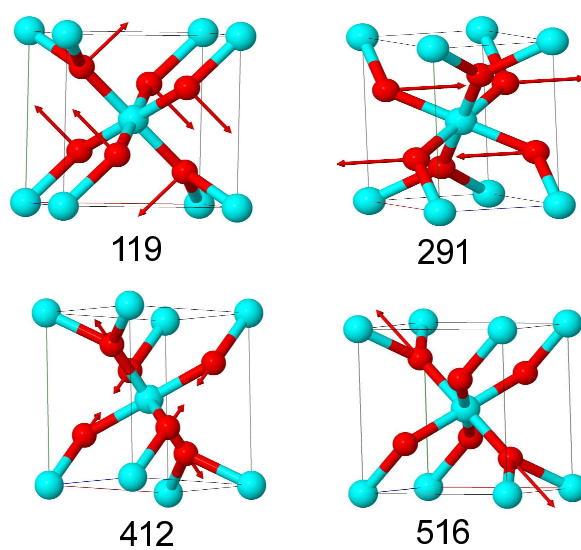


**Figure F.1:** Modes of the rutile structure that are Raman active along with their frequencies in  $\text{cm}^{-1}$ .

## F. RAMAN ACTIVE MODES OBSERVED IN RUTILE STRUCTURES

# Appendix G

## CaF<sub>2</sub>-Energy-Volume curves

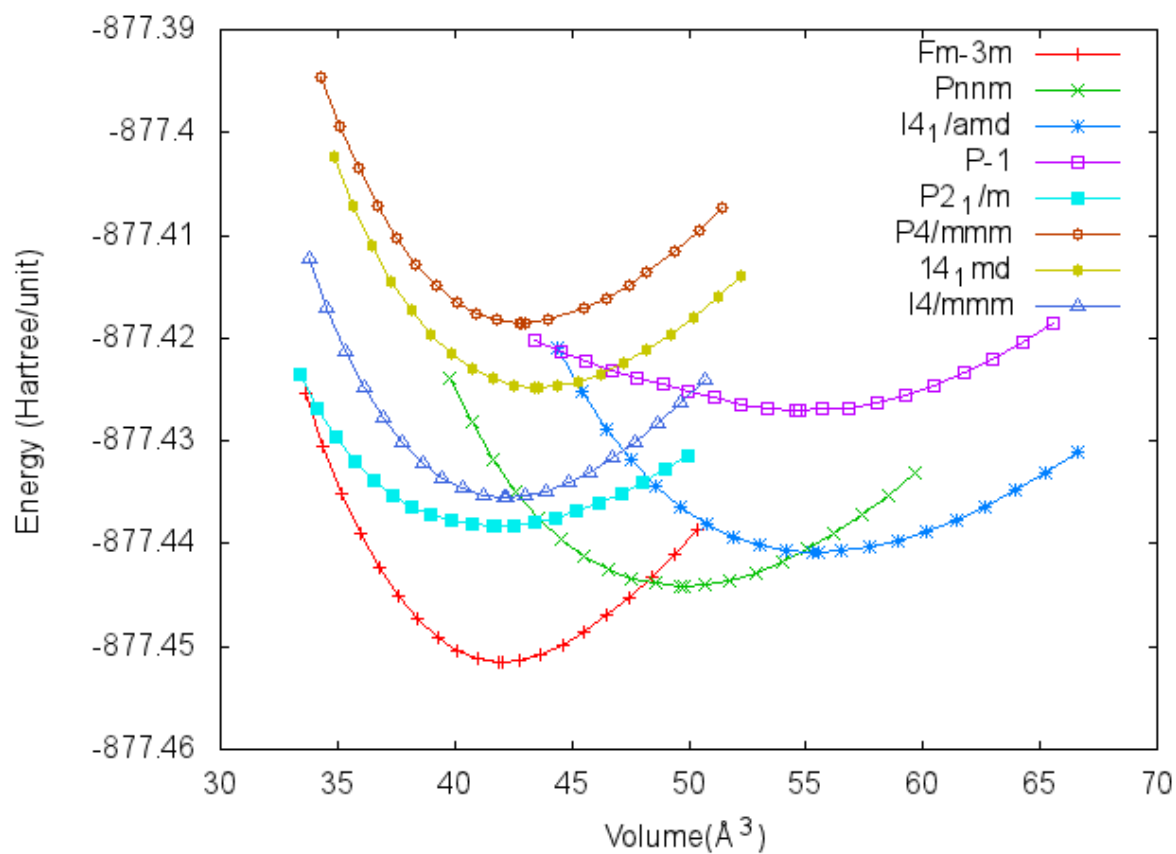


**Figure G.1:** Energy-Volume curves derived for important structures of bulk CaF<sub>2</sub> found from Monte-Carlo simulated annealing.

## G. $\text{CAF}_2$ -ENERGY-VOLUME CURVES

---

# Appendix H

## List of publications

1. “Ab initio and empirical energy landscapes of  $(\text{MgF}_2)_n$  clusters ( $n = 3,4$ )”, S. Neelamraju, K. Doll, J. C. Schön and M. Jansen, *Phys Chem Chem Phys*, **14**(3), 1223-34 (2012).
2. “Experimental and theoretical study on Raman spectra of magnesium fluoride clusters and solids”, S. Neelamraju, A. Bach, J. C. Schön, D. Fischer and M. Jansen, *J. Chem. Phys.* **197**, 194319 (2012).
3. “CCL - an algorithm for the efficient comparison of clusters”, R. Hundt, J. C. Schön, S. Neelamraju, J. Zagorac and M. Jansen, *J. Appl. Cryst.* (**accepted**).
4. “Evolution of order in amorphous-to-crystalline phase transformation of  $\text{MgF}_2$ ”, X. Mu, S. Neelamraju, W. Sigle, C. T. Koch, N. Toto, J. C. Schön, A. Bach, D. Fischer, M. Jansen and P. A. van Aken, **Submitted**.
5. “Atomistic simulation of  $\text{MgF}_2$  crystal growth via low-temperature atom beam deposition”, S. Neelamraju, J. C. Schön and M. Jansen, **In preparation**.

## H. LIST OF PUBLICATIONS

---



# **Part VIII**

## **Formalia**



## Eidesstattliche Versicherung

Ich versichere hiermit an Eides Statt, dass ich die vorliegende Arbeit selbständig verfasst und die verwendeten Hilfsmittel angegeben habe.

# Curriculum Vitae

## Personal Data

<b>Name</b>	Sridhar Neelamraju
<b>Date of Birth</b>	27.06.1986
<b>Place of birth</b>	New Delhi
<b>Marital Status</b>	Single

## Schooling

- 2004 Bharatiya Vidya Bhavan's Vidyashram, Hyderabad, India

## University studies

<b>2004 – 2007</b>	<b>B.Sc (Hons.) Chemistry</b> St.Stephen's College, Delhi, India
<b>2007 – 2008</b>	<b>M.Sc in Theoretical Chemistry</b> University of Oxford, Oxford, United Kingdom
<b>2009 – 2013</b>	<b>Ph.D. in Chemistry</b> Max Planck Institute for Solid State Research, Stuttgart, Germany